

Directional Proton Conductance in Bacteriorhodopsin Is Driven by 2 Concentration Gradient, Not Affinity Gradient

Zhong Ren (✉ zren@uic.edu)

University of Illinois at Chicago <https://orcid.org/0000-0001-7098-3127>

Biological Sciences - Article

Keywords: proton pump, retinal, serial crystallography, singular value decomposition, X-ray free electron laser

Posted Date: November 2nd, 2021

DOI: <https://doi.org/10.21203/rs.3.rs-944138/v3>

License: © ⓘ This work is licensed under a Creative Commons Attribution 4.0 International License.

[Read Full License](#)

1 **Directional Proton Conductance in Bacteriorhodopsin Is Driven by**
2 **Concentration Gradient, Not Affinity Gradient**

3
4 Zhong Ren

5
6 Department of Chemistry, University of Illinois at Chicago, Chicago, IL 60607, USA
7 Renz Research, Inc., Westmont, IL 60559, USA

8
9 zren@uic.edu

10 ORCID 0000-0001-7098-3127

11
12 **Keywords**

13 proton pump, retinal, serial crystallography, singular value decomposition, X-ray free
14 electron laser

15
16 **Abstract**

17 It is widely spread that microorganisms can harvest energy from sun light to establish
18 electrochemical potential across cell membrane by pumping protons outward. Light
19 driven proton pumping against a transmembrane gradient entails exquisite electronic
20 and conformational reconfiguration at fs to ms time scales. However, transient
21 molecular events along the photocycle of bacteriorhodopsin are difficult to comprehend
22 from noisy electron density maps obtained from multiple experiments when the
23 intermediate populations coexist and evolve as a function of 13 decades of time. Here I
24 report an in-depth meta-analysis of the recent time-resolved datasets collected by
25 several consortiums. This analysis deconvolutes the observed mixtures, thus
26 substantially improves the quality of the electron density maps, and provides a clear
27 visualization of the isolated intermediates from I to M. The primary photoproducts
28 revealed here suggest a proton transfer uphill against 15 pH units is accomplished by
29 the same physics that governs the tablecloth trick. While the Schiff base is displaced at
30 the beginning of the photoisomerization within ~30 fs, the proton stays due to its
31 inertia. This affinity-independent early deprotonation builds up a steep proton
32 concentration gradient that drives the directional proton conductance toward the
33 extracellular medium. This mechanism fundamentally deviates from the widely
34 adopted assumption based on equilibrium processes driven by light-induced changes of

35 proton affinities. The method of a numerical resolution of concurrent events from
36 mixed observations is also generally applicable.

37

38 **Introduction**

39 Bacteriorhodopsin (bR) captures photon energy to pump protons outward from the
40 cytoplasm (CP) against the concentration gradient, thus converts light into
41 electrochemical energy. This integral membrane protein of 28 kDa singlehandedly
42 achieves the exact same goal of photosynthesis and cellular respiration combined. This
43 simplicity is widely exploited in optogenetics and bioelectronics (Fenno et al., 2011; Li et
44 al., 2018). A trimeric form of bR on the native purple membrane shares the retinal
45 chromophore and the same protein fold of seven transmembrane helices A-G (Fig. S1)
46 with large families of microbial and animal rhodopsins (Ernst et al., 2014; Kandori,
47 2015). An all-*trans* retinal is covalently connected to Lys216 of helix G through a
48 protonated Schiff base (SB) pointing toward the extracellular side (EC) in the resting
49 state, of which the double bond $C_{15}=N_{\zeta}$ is also in *trans* (traditionally also noted as *anti*
50 (McCarty, 1970)) Upon absorption of a visible photon, the retinal isomerizes efficiently
51 and selectively to adopt the 13-*cis* configuration (Govindjee et al., 1990). Extensive
52 structural events during the ultrafast isomerization sampling and stereochemical
53 selection were recently revealed by the companion study of this work (Ren, 2021).

54

55 *Photocycle*

56 It has been shown that the species I or a collection of species prior to the
57 photoisomerization arises before 30 fs and remains in 13-*trans* instead of a near 90°
58 configuration about $C_{13}=C_{14}$ (Zhong et al., 1996). A red-shifted intermediate species J in
59 13-*cis* forms around 450-500 fs and decays at 3 ps to a less red-shifted species K
60 (Applebury et al., 1978; van den Berg et al., 1990), which lasts longer than five decades
61 of time therefore becomes the most “stable” intermediate throughout the entire
62 photocycle on a log-time scale. The blue-shifted L state emerges from K at 1-2 μ s and
63 converts to strongly blue-shifted M states at \sim 50 μ s (Lozier et al., 1975). The L \rightarrow M
64 transition has been considered as the step for the proton acceptor, the carboxylate group
65 of Asp85, to become neutralized by receiving a proton (Fahmy et al., 1992). This
66 established view has been largely based on peak assignments in resonance Raman and
67 Fourier transform infrared spectroscopy (FTIR) on wildtype bR and various mutants
68 (Braiman et al., 1988, 1991; Gerwert et al., 1990; Lewis et al., 1974). However, the event

69 of SB deprotonation has been mistakenly inferred from the observed protonation of the
70 carboxylate of Asp85. It has been widely quoted in the literature that the proton
71 transfer from the SB to the proton acceptor occurs as the M formation. This study finds
72 that this proton transfer spans ten decades in time instead of a single event. The
73 electron density maps of I to M are unscrambled from one another in this analysis.
74 They clearly show extensive conformational changes leading to and developing from
75 the isomerization of the chromophore (Fig. 1).

76

77 *Structure*

78 Although the first low resolution map of bR was revealed in 1975 (Henderson and
79 Unwin, 1975), the majority of structural information awaited technology advances until
80 the 1990s in cryo electron microscopy (Henderson et al., 1990), electron diffraction
81 (Grigorieff et al., 1996), and X-ray crystallography (Pebay-Peyroula et al., 1997). Finally,
82 the atomic resolution of a bR model was achieved (Luecke et al., 1999a). The main
83 technique to study intermediates along the photocycle used to be cryo trapping,
84 including both light illumination of crystals at room temperature followed by rapid
85 freezing and illumination at elevated cryo temperatures. The 13-*cis* retinal and its
86 associated H-bond network have been observed in M state with extensive
87 conformational changes in the anchor helix G (Luecke et al., 1999b), FG loop, EC half of
88 helix C (Takeda et al., 2004), and an enlarged CP pocket (Sass et al., 2000). Numerous
89 attempts have been made to capture intermediates other than M with inconsistent
90 results (Wickstrand et al., 2015).

91

92 A new phase began with time-resolved serial crystallography conducted at X-ray
93 free electron lasers (XFELs). The ultrashort X-ray laser pulses open the opportunity to
94 capture transient structural species in the photocycle as short-lived as fs. It is equally
95 important that serial crystallography enables photo triggering and data collection at
96 room temperature. Authentic signals of conformational changes of greater amplitudes
97 are expected at room temperature compared to cryo trapping. Several international
98 consortiums carried out large operations and accumulated abundant time points along
99 the photocycle that spans more than 13 decades of time. Judged only from the
100 extensiveness of the reported signals, time-resolved XFEL data at room temperature
101 unfortunately do not surpass those captured by cryo trapping, which hints at much
102 needed improvements in experimental protocols and data analysis methods. Nogly et

103 al. captured retinal isomerization to 13-*cis* at 10 ps (Nogly et al., 2018). More
104 importantly, they observed that the SB water moves before the isomerization and the SB
105 itself has already displaced at the earliest time point of 49-406 fs, which is the key
106 contribution to this analysis. Kovacs et al. contributed datasets at many short time
107 delays (Kovacs et al., 2019). Nango et al. found an ordered water in a newly established
108 H-bond network involving the SB in the 13-*cis* retinal pointing to the CP on ns- μ s time
109 scale, which led to their conclusion of the proton path (Nango et al., 2016). These are
110 three major sources of data analyzed in this study (Table S1). Several synchrotron
111 datasets at ms delays also contribute to this analysis (Weinert et al., 2019).

112
113 Structural heterogeneity is the common difficulty to both cryo trapping and time-
114 resolved serial crystallography at room temperature. To what extent a specific species
115 can be enriched in crystals depends on the reaction kinetics under a condition of
116 illumination, such as wavelength and temperature. A more stable species K or M can
117 reach a higher fractional concentration at a specific time point due to a greater ratio
118 between the rates going into and exiting from that species. Others will be populated
119 poorly because of their transient nature. This structural heterogeneity causes the
120 practical difficulties in the interpretation of electron density maps and the refinement of
121 these intermediate structures (Ren et al., 2013). An assumption in nearly all previous
122 studies has been that each dataset, at a cryo temperature or at a time delay, is derived
123 from a mixture of a single photoinduced species and the ground state. Therefore, the
124 difference map reveals a pure intermediate structure. This assumption leads to the
125 more time points the more overinterpretation rather than the more overdetermination.
126 Previous studies using cryo trapping and time-resolved crystallography could not
127 evaluate clear electron density maps of pure intermediate species without a proper
128 deconvolution of heterogeneous species. Because none of the experimental conditions
129 at a cryo temperature or a time point can guarantee an experimental map that does not
130 involve heterogeneous mixture (Ren et al., 2013; Yang et al., 2011). This work is yet
131 another case study to test our general strategy of dynamic crystallography, that is, from
132 the outset every observation at a time point or a temperature setting is treated as a
133 mixture of unknown number of structural species with unknown populations
134 (Methods). The structures of all intermediate species are also unknown except the
135 ground state. The analytical protocol is responsible for a reliable structural
136 interpretation by overdetermination of these unknowns from consistent observations

137 (Ren, 2019; Ren et al., 2013; Yang et al., 2011). Inconsistent observations are identified
138 and isolated.

139

140 *Mechanism*

141 Understanding the mechanism of proton pumping uphill against gradient has been
142 centered on two entangled aspects: Where are the proton uptake and release pathways?
143 How does the retinal photoisomerization adjust the chemical groups' ability to hold
144 proton along these pathways? The ability of a chemical group to hold a proton is
145 measured by its value of pK_a , where p stands for $-\log_{10}$ function and K_a is the acid
146 dissociation constant, one form of the equilibrium constant of a chemical reaction. It is
147 clear that a proton previously retained by the SB is accepted by the carboxylate group of
148 Asp85 in helix C and eventually released to the EC medium. Each of Arg82, Asp85, 212,
149 Glu194, 204, and some waters could play a role (Balashov et al., 1997; Govindjee et al.,
150 1996; Richter et al., 1996). However, the sequence of events during this proton
151 conductance is unclear thus often mistakenly inferred.

152

153 At the resting state of bR, the SB holds a proton tightly with a pK_a of 13.3 pointing
154 toward the EC channel (Druckmann et al., 1982; Sheves et al., 1986). The nearby proton
155 acceptor Asp85 bridged to the SB by a water stays quite acidic with its pK_a spanning 2-3
156 range (Balashov et al., 1996). That water, often numbered as 402, has been identified as
157 the centerpiece of the mechanism (Wickstrand et al., 2015). Therefore, the SB proton is
158 associated with both N and O simultaneously in $N\zeta:H^+:OH_2$ with both interactions much
159 weaker than an ordinary single bond (Fig. 2c). One of the competing hypotheses is
160 willing to consider that the proton is first brought to the CP side by the SB
161 isomerization to 13-*cis*, and then conducted through Thr89 and a newly found water
162 other than Wat402 on the CP side, and finally reaches Asp85 (Nango et al., 2016). The
163 difficulty encountered by this hypothesis is the rollercoasting pK_a values that the proton
164 has to go through. The other competing hypothesis relies on a H-bond network long
165 after photoisomerization but largely similar to that in the resting state to translocate the
166 proton on the SB. The H-bond from the SB to Wat402 has to be reconciled with two
167 double bonds $C_{13}=C_{14}$ and $C_{15}=N\zeta$, both highly twisted away from *trans* and *cis*
168 configurations to near 90° , until a successful proton translocation to Asp85 (Lanyi and
169 Schobert, 2007). This interpretation of these highly twisted double bonds is a direct

170 consequence of the inability to unscramble a mixed observation of multiple
171 conformations.

172
173 Despite intense studies, fundamental questions on the operating mechanism of this
174 proton pump remain puzzling and some unanswered. Q1) How does the protonated
175 SB with a pK_a of 13.3 transfer its proton to the acidic acceptors and when? Q2) Which
176 molecular event, the isomerization, or another event, switches the accessibility of the SB
177 from EC to CP and how does the SB avoid reprotonation on the wrong side? Q3) How
178 are protons conducted $> 15 \text{ \AA}$ through the rollercoasting pK_a values and released into
179 the EC medium from the SB of a high pK_a through aspartic acids of low pK_a , arginine
180 (strictly speaking, its guanidinium ion) and tyrosines of high pK_a , and glutamic acids of
181 low pK_a again? Q4) How is a gradient-driven proton backflow prevented in the resting
182 state and during the pumping motions? No convincing evidence can directly
183 demonstrate a photoinduced reversal of the drastically different proton holding abilities
184 along the EC half channel to facilitate a spontaneous proton conductance that would
185 require an ascending order of pK_a 's. The fundamental flaw in the previous line of
186 thinking is multiple equilibrium steps driven by proton affinities as the values of pK_a
187 describe. A proton is spontaneously transferred from one chemical group with a less
188 proton affinity, that is, smaller pK_a , to another with a greater affinity, that is, larger pK_a
189 (Jardetzky, 1966; Stoeckenius et al., 1979). Such proton conductance was presumed to
190 be accomplished by the means of abundant thermal events of protonation and
191 deprotonation, that is, equilibrium. If a slope of affinity does not satisfy the directional
192 flow of protons, it has been commonly assumed that a photoinduced reversal of proton
193 affinity must have occurred during the photocycle (Stoeckenius, 1999). This study
194 shows that equilibrium is not how the light-driven proton pump bR works, and the
195 directional proton conductance is not driven by increasing affinities but by a
196 concentration gradient of protons.

197
198 Here the ultrafast molecular events revealed from the serial crystallographic
199 datasets demonstrate that the photochemical reaction of bR transfers a proton held by
200 the SB to form a strong acid that barely has any ability to hold a proton. However, this
201 proton transfer is not achieved by equilibrium therefore not governed by pK_a 's. Instead,
202 before the isomerization occurs, this proton transfer takes place due to the SB
203 displacement within ~ 30 fs in a single molecular event. The proton's inertia prevents it

204 from accelerating as fast as the SB under the same physics of the tablecloth trick (Q1).
205 Rapid photoisomerization flips the already deprotonated SB at 500 fs, thus protects the
206 SB from being reprotonated on the wrong side (Q2). Proton conductance follows a
207 descending order of the proton concentration gradient established in the EC half
208 channel (Q3). A built-in seal constructed by an irregular helix reacts to the
209 isomerization and ensures no proton leakage back to the CP channel during the motions
210 of proton pumping (Q4). The inner EC channel is strictly surrounded by chemical
211 groups of high pK_a 's so that protons can only flow out but cannot flow back in even
212 during dark (Q4). See Supplementary Information (SI) for coherent answers to these
213 questions.

214

215 **Results and Discussion**

216 A total of 42 datasets and 36 time points analyzed in this study are divided into two
217 groups: 18 short delays up to 10 ps and 18 long delays ranging from ns to ms, which
218 unfortunately leaves a gap longer than three decades not surveyed (Fig. 1 and Table S1).
219 Difference Fourier maps among these time points and with respect to their
220 corresponding dark datasets are calculated according to protocols previously described
221 (Methods). Singular value decomposition (SVD) of difference maps and the subsequent
222 Ren rotation in a multi-dimensional Euclidean space established by SVD (Ren, 2016,
223 2019, 2021) are performed separately to 126 difference maps of the short delays and 101
224 maps of the long delays (Methods). This method of "decomposition and
225 deconvolution" results in a clean separation of electron density changes due to
226 coexisting photoexcited species mixed in the observed datasets. The main findings are
227 summarized in a Gantt chart (Fig. 1). Eight intermediate structures along the
228 photocycle, now isolated from one another, are refined against reconstituted structure
229 factor amplitudes (Methods; Table S2) (Ren, 2021). The assignments of the previously
230 identified intermediates I to M to these refined structures are largely based on the time
231 stamps of the observed signals. No absorption signatures are directly associated with
232 the X-ray data.

233

234 *Intermediates I', I, and Schiff base deprotonation*

235 Three decomposed map components \mathbf{U}_{10} , \mathbf{U}_{14} , and \mathbf{U}_{17} of the short delays contain
236 extraordinary structural signals in terms of their extensiveness and quality (Ren, 2021).
237 These signals originate exclusively from a few time points of Nogly et al., too few to fit

238 the time dependency with exponentials. Instead, a spline fitting through these time
 239 points estimates the coefficients c_{10} , c_{14} , and c_{17} in the linear combination of $c_{10}\mathbf{U}_{10} + c_{14}\mathbf{U}_{14}$
 240 $+ c_{17}\mathbf{U}_{17}$ for the early states I, J, and their respective precursors I', J' (Ren, 2021). The
 241 precursor prior to I state is located on the spline trajectory from the origin, that is, the
 242 ground state bR at the time point of 0- before the photon absorption, to the first time
 243 point of 49-406 fs (PDB entry 6g7i). It would be appropriate to name this location on the
 244 trajectory I' as a precursor leading to I state judged only by the time point at ~30 fs.
 245

246 The all-*trans* retinal in bR is largely flat except C₁₅ (Fig. 2b 2nd panel). However, two
 247 single bonds of Lys216 are highly twisted to near 90° (Fig. 2b 4th panel), which forms a
 248 corner at C_ε that deviates from the flat plane of the all-*trans* retinal, protrudes inboard,
 249 and makes a van der Waals contact at 3.4 Å with Thr89 in helix C (Fig. 2b 2nd panel).
 250 This contact is identified in this study as a seal between the extracellular (EC) and
 251 cytoplasmic (CP) half channels. The retinal in I' remains in near perfect all-*trans*
 252 configuration, including the Schiff base (SB) double bond C₁₅=N_ζ (Fig. S2), while it is
 253 creased into an S-shape in an expanded retinal binding pocket together with other
 254 features revealing the isomerization sampling (Ren, 2021). The slit between Thr89 and
 255 the SB increases to 4.3 Å that may break the seal between two half channels, which is
 256 inconsequential as argued below. The C₂₀ methyl group swings 1.1 Å to the outboard
 257 direction, a motion previously known but at much later time. These motions are
 258 rotations around the long axis of the polyene chain instead of translations (Fig. 2b
 259 bottom panel). It is important that the displaced Wat402, now a hydronium ion H₃O⁺
 260 (see below), remains H-bonded to both Asp residues in I'. However, its association
 261 with the SB increases to 3.3 Å that barely qualifies as a H-bond.
 262

263 Due to the availability of the time stamp, a conformational change captured in a
 264 time-resolved experiment can be converted to the velocity of an atomic displacement
 265 that would further hint the acceleration and force required to achieve the observed
 266 conformation changes at the time of the measurement. It can be shown that a force >
 267 500 pN is required to keep the proton accelerating as fast as N_ζ that has been displaced
 268 by 0.7 Å within 30 fs. A force of this magnitude could unfold α-helices or even an entire
 269 protein (Su and Purohit, 2009; Takahashi et al., 2018). Accelerating the proton with the
 270 SB is not achievable given the charge on the proton and its H-bond association with
 271 Wat402. Compared to the regular single bond N-H in an amine group at a pK_a of 40, the

272 coordination bond $N_{\zeta}:H^+$ in the protonated SB at its pK_a of 13.3 is much weaker. In
273 addition, a proton acceleration with the SB would have to break its interaction with
274 Wat402, nearly as costly as to break the coordination bond $N_{\zeta}:H^+$ (Fig. 2c). Therefore,
275 which of the two weak interactions $N_{\zeta}:H^+:O402$ survives the abrupt tare before the
276 photoisomerization is determined by the inertia of the proton. It captures the starting
277 moment of a reliable deprotonation from the SB that does not depend on thermal
278 equilibrium. Here the 0.6 Å increase from the SB to Wat402 is attributed to the
279 separation of the proton from the SB rather than from Wat402. Instead of accelerating
280 with the SB, the proton stays with Wat402 to form a hydronium H_3O^+ due to its inertia
281 (Q1; Figs. 1 inset and 2c). Since several water molecules have been observed in the
282 inner EC channel, possibilities of other proton complexes also exist, such as $H_5O_2^+$ (Marx
283 et al., 1999; Mathias and Marx, 2007). The hydronium 402 has been shown possible by
284 magic angle spinning NMR (Friedrich et al., 2020).

285
286 This conjecture here, however, is not based on an observation of the scattered X-rays
287 by the proton as the proton does not scatter X-ray. Direct evidence supporting this
288 water cluster with excess protons reside in FTIR observations. Complex kinetic
289 behaviors of several broad band continua at the frequencies $> 1700\text{ cm}^{-1}$ were recorded
290 in FTIR experiments and interpreted as protonated water clusters (Garczarek et al.,
291 2004, 2005; Lorenz-Fonfria et al., 2017; Wang and El-Sayed, 2001). However, detailed
292 assignments of these continua remain debatable. For example, the removal of one
293 terminal carboxylate near the exit of the EC channel (Fig. S1) in the mutant E204Q
294 certainly could affect proton release. But the observed change in some FTIR continua
295 cannot be easily pinpointed to a water cluster in the outer EC channel (Garczarek et al.,
296 2004), since shutting down one proton release pathway could affect the kinetics of the
297 upstream water cluster in the inner EC channel. Furthermore, the FTIR continua most
298 likely originate from a super-acidic water cluster in the inner EC channel because a
299 well-known proton barrier surrounds the inner EC channel but no proton barrier for the
300 outer EC channel (see below).

301
302 The hydronium 402 is likely short-lived. Either Asp85 or 212 “quickly” accepts
303 another proton from the hydronium and returns it back to Wat402 (Fig. 1 inset). The
304 lifetime of hydronium 402 is unclear from X-ray diffraction. Nevertheless, this lifetime
305 does not have to contradict the commonly adopted view that these aspartic acids are

306 protonated later in tens of μs to ms during M formation (Briman et al., 1988, 1991;
307 Gerwert et al., 1990), given that the pK_a difference between the aspartic acid and
308 hydronium is < 4 pH units. As argued below, a super-acidic water cluster harboring
309 excess protons in the inner EC channel must be established before proton release.
310 Reliable deprotonations from the SB in consecutive photocycles continuously
311 overcharge the inner EC channel. The deprotonation event cannot be directly inferred
312 from the vibrational signatures due to the protonation of the carboxylic proton
313 acceptors in the Asp residues. In other words, the “proton transfer” from the SB to the
314 proton acceptor, as commonly stated in the literature, is not a single event. Instead, it
315 spans ten decades in time.

316
317 The retinal in I state remains in near perfect all-*trans*, including the SB. However,
318 the major difference from the precursor is that the single bond $\text{N}_\zeta\text{-C}_\epsilon$ is now in a perfect
319 *syn* conformation, and the anchor Lys216 has largely returned to its resting
320 conformation (Figs. 2b 4th panel and S3). The SB makes a sharp U-turn toward inboard
321 before 500 fs (Fig. S2) and closes the slit with Thr89 to 3.8 Å and ends the breakage in
322 the seal that is too brief to result in a proton leakage (Q3). After the U-turn, the
323 deprotonated SB is pointing toward inboard while Wat402, currently a hydronium, is
324 displaced outboard but remains H-bonded to both Asp85 and 212. The SB and Wat402
325 are not only beyond a H-bond distance, but also in a bad geometry for proton exchange
326 (Fig. S3d). The accessibility of the SB in I state is already very limited while the SB is
327 reoriented toward inboard despite that the isomerization is yet to occur (Q2). This
328 ultrafast U-turn is how the SB gets rid of the proton by a mechanism of the same
329 physics that governs the tablecloth trick (Q1; Fig. S2). Holding Wat402 in place by
330 Asp85 and 212 symmetrically from inboard and outboard, respectively, is as important
331 as the ultrafast shaking of the SB to its successful deprotonation. See SI for mutant
332 functions when the symmetric holding of Wat402 is disrupted. Here the tablecloth trick
333 is not an analogy to the SB deprotonation. Both are governed by the exact same
334 Newton mechanics: A certain mass, such as a planetary body, a dining set, or a
335 proton, does not accelerate fast enough unless a sufficient force is exerted on it. The U-
336 turn of the SB marks the peak power, or the maximum rate of enthalpy change dH/dt ,
337 of the entire photochemical reaction (see Discussion). The spectrogram derived from
338 the transient absorption or transmittance clearly supports that the photocycle reaches its
339 peak power within the first tens of fs (Kahan et al., 2007; Kobayashi et al., 2001). If a

340 deprotonation is unsuccessful at the peak power of the photocycle, there will be no
 341 further opportunity to translocate a proton from a fair base to a decent acid uphill
 342 against 11 pH units under equilibrium. The same is true that a proton transfer is
 343 energetically impossible from the protonated SB at a pK_a of 13.3 to form a hydronium, a
 344 strong acid of a pK_a of -1.7, under equilibrium. The deprotonated SB is extremely
 345 vulnerable at this moment in I state despite its limited accessibility, as it will be quickly
 346 reprotonated if it lingers on in the EC channel to allow an equilibrium. As shown
 347 below, the isomerization to a 13-*cis* retinal prevents such an equilibrium in a futile
 348 photocycle. However, some of the photocycles are indeed unsuccessful as its quantum
 349 yield indicates if a reprotonation event does occur before the isomerization.

350

351 Incidentally, all previous hypotheses on the mechanism of SB deprotonation imply a
 352 formation of hydronium at one point or another (Lanyi and Schobert, 2007; Nango et al.,
 353 2016). It would require a donor group with a pK_a more negative than -1.7 to reliably
 354 form a hydronium by the means of equilibrium. None of the previous hypotheses have
 355 successfully explained how this is possible.

356

357 *Intermediates J', J and traveling water or hydronium 402*

358 Near perfect 13-*cis* is successfully refined in both structures of J' at ~700 fs and J at ~20
 359 ps with a contracted retinal binding pocket (Fig. 2b 4th panel) (Ren, 2021). However, the
 360 SB double bond $C_{15}=N_{\zeta}$ is momentarily distorted from the *trans* configuration in J' with
 361 a torsion angle of 133°. The *trans* double bond $C_{15}=N_{\zeta}$ is promptly restored in J (Fig. 2b
 362 4th panel). The SB N_{ζ} is rotating clockwise looking from the proximal to distal direction
 363 in the entire process of the isomerization $I' \rightarrow I \rightarrow J' \rightarrow J$ (Fig. 2a). If the deprotonated
 364 SB isomerizes to 13-*cis* at ~500 fs, this photocycle is productive. Otherwise, a photocycle
 365 could be wasted if reprotonation occurs prior to the isomerization as it could happen
 366 sometimes even in wildtype. The isomerization completes the accessibility switch for
 367 the SB from the EC half channel to the CP (Q2).

368

369 Due to the 13-*cis* configuration, C_{20} methyl group protrudes to a CP direction that is
 370 further tilted toward outboard from its original direction. No additional consequence is
 371 immediately obvious until the retinal flattens and returns to its original plane at later
 372 intermediates. At this moment, Trp182 and the retinal anchor Lys216 stay in their
 373 resting positions. Wat402, perhaps currently still a hydronium ion, is well defined in

374 both J_s (Ren, 2021). Contrary to the previous conclusion (Wickstrand et al., 2015), this
375 traveling water is never disordered throughout the surveyed portion of the photocycle
376 up to M_2 (see below) despite its large trajectory spanning greater than 3 Å (Fig. 2a).
377 Wat402 is observed with both strong difference electron density and its refined electron
378 density. Its association with Asp85 and 212 remains unwavering throughout the
379 photocycle except one increase to 4.1 Å from Asp212 during J' , the first moment after
380 isomerization. This observation demonstrates that Wat402, a hydronium through a
381 large part of the photocycle, is an integral part of the moving cluster that accepts the
382 proton from the SB. Most likely, this water will remain ordered throughout the rest of
383 the photocycle not yet surveyed.

384
385 The main cause to this contradiction is that a light induced change at any given time
386 point consists of a mixture of multiple conformations. As the most straightforward
387 example, the dramatic motion of Wat402 appears to be a disorder in an experimental
388 map prior to deconvolution. An experimental map is a spatial average over the
389 diffracting crystals and a temporal average over the X-ray exposures. In case of serial
390 crystallography, the range of this average is an extensive pool of crystals potentially
391 with diverse individualities (Ren et al., 2018). The only common feature among
392 multiple species of bR intermediates is the negative density on the original location of
393 Wat402 due to its departure. Multiple positive features at various locations are of low
394 occupancies without a proper deconvolution. In this analysis, a linear combination of
395 several SVD components unscrambles the mixture so that each state along the
396 photocycle presents a pure conformational species, a time-independent structure. Is
397 there an experimental solution to this problem of structural heterogeneity? Would a
398 better time resolution improve an experimental difference map so that a traveling water
399 molecule would always be temporally resolved? The answer is both surprisingly and
400 conclusively no, even if, for the sake of argument, an ultimate time resolution of truly
401 zero is achievable by two zero-width impulses of pump and probe (Strictly speaking,
402 each crystal must also be a spatial impulse, that is, zero size.). Because at no time
403 throughout the entire photocycle, the traveling water is synchronized throughout the
404 entire crystal, even if every retinal in the crystal absorbs a visible photon at the exact
405 same time zero. There is no difference between crystal and solution in this aspect,
406 which has been long recognized as Moffat laid the foundation of time-resolved

407 crystallography (Moffat, 1989, 2001). In conclusion, a numerical resolution of structural
408 heterogeneity, as exemplified here, is the last and the only resort (Ren et al., 2013).

409

410 *Five-decade long-lived K and global change in L*

411 This work continues with another joint analysis of the time-resolved datasets at long
412 delays > 10 ns collected mainly by Nango et al. with contributions from Nogly et al.,
413 Kovacs et al., and Weinert et al. (Table S1). These datasets at the long delays are
414 relatively noisier and contain systematic errors from one experiment to another. The
415 analytical procedure of SVD and the subsequent Ren rotation (Ren, 2016, 2019, 2021) is
416 capable of isolating time-resolved signals from these error and noise components. SVD
417 of 101 difference Fourier maps identifies 19 major components (Fig. S4a). Four of them
418 contain outstanding signals of structural changes (Fig. S5). Two others also carry
419 structural signals but without a clear time dependency (Fig. S6). The number of
420 datasets at long delays warrants an exponential fitting to the SVD coefficients (Fig. S7)
421 (Schmidt et al., 2010), which models the reaction scheme of the photocycle better
422 compared to the spline fitting applied to the limited number of short delays above. The
423 time constants obtained from the exponential fitting agree well with the transition times
424 between intermediates K, L, M₁, and M₂ known from spectroscopy. Coefficients for
425 relatively pure states are estimated and the refinement protocol based on reconstituted
426 difference maps again produce atomic coordinates of these states (Methods) (Ren, 2021).

427

428 The refined structures of K and L are discussed in SI (Figs. S8 and S9). A flattened
429 13-*cis* retinal is finally achieved in L with many global changes. The L state represents
430 the end goal of the global conformational changes due to the retinal isomerization.
431 Additional changes after L are no longer global (see below). C_δ-C_ε of the anchor moves
432 outboard and could break the seal with Thr89 once again. Last time, a potential
433 breakage occurs in I' at tens of fs that is too brief for any proton leak (Fig. 2b 2nd panel).
434 This time, the ns-μs time scale allows the protein to react. It is clearly observed that
435 Thr89 and helix C always follow C_δ-C_ε outboard in J, K, and L and maintain a distance
436 no more than 3.6 Å because of its tendency to be straightened (Figs. 3f and S10a). This
437 motion was also captured previously in cryo-trapped intermediates (Royant et al.,
438 2000). Therefore, the seal between two half channels is kept intact (Q4). Here the
439 mechanism of these motions of helices is attributed to several irregularities in these
440 helices (Fig. S10), the kinked helix C (Grigorieff et al., 1996), the stretched helix F, and

441 the π helical segment in G (Pebay-Peyroula et al., 1997). Contrary to the previous belief
442 (Luecke et al., 1999a), it is our general conclusion also from studies of other protein
443 mechanisms that irregularities in secondary structures not merely fulfill some structural
444 requirements but offer a wide variety of mechanical properties to achieve the functions
445 of protein nanodevices (Ren et al., 2016; Shin et al., 2019). These motions of the helical
446 segments collectively result in a tighter EC channel and an open CP channel in L (Fig.
447 S11).

448

449 *Intermediates M_1 , M_2 and proton release*

450 The refined structures of M_1 and M_2 are described in SI (Figs. S12 and S13). Thr89 is
451 kept 3.1 Å away from the SB in L, M_1 , and M_2 constantly so that the seal is well
452 maintained between two half channels (Q4). Compared to the slightly longer distance
453 between Thr89 and the SB at 3.6 Å in J and K, it is obvious that Thr89 and helix C react
454 to the retreating SB during J and K, but the SB is actively pushing Thr89 and helix C
455 from L to M (Fig. 4c). As discussed below, during pumping activity, drastic proton
456 concentration gradient is present across this seal that divides two half channels. A well-
457 maintained seal is crucial to the efficiency of the pump. Various mutants with
458 substitutions of Thr89 that could result in a proton leak retain $\sim 2/3$ of the pumping
459 activity compared to the wildtype (Marti et al., 1991).

460

461 The motions over the EC half of the molecule from tens of μ s to ms are directly
462 related to the pathway of the proton release (Q3). Residues in the EC half channel are
463 not arranged in a monotonic order of their pK_a 's. Quite the contrary, acidic residues
464 Asp85 and 212 with the smallest pK_a 's are at the end of the half channel next to the SB
465 with the greatest pK_a . Another layer of acidic residues Glu9, 194, and 204 are at the EC
466 surface. It is puzzling that Arg82, Tyr57, and 83 are located between these two acidic
467 layers (Figs. 5 and S1). It had been depicted multiple times by similar illustrations in
468 the past that a high pK_a layer is sandwiched between two acidic layers with low pK_a 's in
469 the EC half channel. Yet, the question remains: How are protons conducted through
470 the proton barrier of the guanidinium group of Arg82 that is already protonated and
471 the phenol hydroxyl groups of the Tyr residues that cannot be protonated anymore
472 (Brown et al., 1993)? No evidence shows that such rollercoasting pK_a values would
473 change in any meaningful way by the light-induced conformations. Therefore, the
474 previous proposal on an affinity-driven proton conductance is fundamentally flawed.

475

476 Proton conductance after SB deprotonation through the EC half channel not
477 necessarily operates on the basis of one event of proton release per photocycle. It was
478 previously suggested that a proton pumped in one photocycle could be released in the
479 next or subsequent photocycles (Braiman et al., 1991). However, a flawed common
480 assumption persists that the pumping and releasing of each proton are somehow
481 scheduled in different periods of a photocycle. Here a concentration-driven, instead of
482 affinity-driven, proton conductance is hypothesized. Proton release becomes
483 synchronized to the photocycle only when a super-acidic inner EC channel is
484 established. The first a few photocycles build up a proton concentration at the end of
485 the EC half channel. Multiple groups in the inner EC channel, including various waters,
486 could be all protonated after consecutive photocycles, that is, a puddle of protons
487 establishes a super-acidic inner EC channel as long as the seal of Thr89 is well
488 maintained (Fig. 5c). This is possible because the proton pumping step is a physical
489 process instead of a chemical equilibrium (see above). Although the first a few
490 photocycles are productive, they are not capable of releasing any proton before an
491 established proton concentration gradient. An established super-acidic inner EC
492 channel triggers a concentration-driven proton conductance (Fig. 5d). Proton release
493 from the wildtype bR was observed before proton uptake as if it is coupled with, if not
494 faster than, the protonation of the proton acceptor Asp85 (Braiman et al., 1988, 1991;
495 Gerwert et al., 1990; Zimanyi et al., 1992), which strongly suggests that the newly
496 pumped proton is not the one released to the EC medium in the same photocycle. Here
497 the concentration-driven proton conductance argues that the newly pumped proton
498 causes a proton overflow from the already super-acidic inner EC channel. Therefore,
499 the observed “early release” is actually a very late release during a subsequent
500 photocycle, several cycles after the very proton has been pumped into the inner EC
501 channel (Fig. 5e).

502

503 The inner EC channel has been called a proton cage at the active site of bR (Friedrich
504 et al., 2020), which reflects the same fact of the proton barrier (Fig. 5). Here I argue that
505 the super-acidic inner EC channel causes a second protonation of the guanidinium
506 group because of three electron-rich nitrogens (Fig. 5d). The observation to corroborate
507 this speculation is the motions of Arg82, Glu194, and 204 during $K \rightarrow L \rightarrow M_1 \rightarrow M_2$.
508 The monovalent guanidinium cation during the early photocycle has no salt bridge to

509 Glu194 and 204 until M state. It appears that Asp85 and 212 are continuously
510 protonated by proton pumping thus neutralized in the inner EC channel. Several
511 hydronium ions make the inner EC channel positively charged. The observed kinetics
512 of FTIR continua could explain excess protons harbored by the water cluster in the
513 inner EC channel (Garczarek et al., 2004, 2005; Lorenz-Fonfria et al., 2017; Wang and El-
514 Sayed, 2001). An extra positive charge on the short-lived divalent guanidinium drives
515 itself away from the inner EC channel and toward the negative charged Glu residues in
516 the outer EC channel (Fig. 5a). The EC segments of helices C and G move closer to each
517 other in the refined M structures, where Arg82 is sandwiched in between (SI; Fig. 4).
518 Molecular dynamics simulations found that the orientation of Arg82 is correlated with
519 the charge difference between the inner and outer acids (Ge and Gunner, 2016). The
520 contact between Glu194, 204, and the guanidinium discharges the second extra proton
521 to the outer EC channel and the EC medium (Fig. 5e). A monovalent guanidinium
522 cation is unable to discharge its proton to the carboxylates of the Glu residues due to
523 their low proton affinity. Therefore, Arg82 is a unidirectional proton valve that
524 conducts protons outward, but only under sufficient proton concentration in the inner
525 EC channel. During dark, Arg82 prevents a concentration-driven proton leak back into
526 the cell, because the EC medium cannot become super acidic as long as sufficient water
527 is available. See SI for mutant functions when the proton barrier is breached by
528 substitutes for Arg82.

529

530 **Discussion**

531 Under the guidance of Jardetzky's allosteric model of transmembrane pump (Jardetzky,
532 1966) and the common line of thinking led by Stoeckenius (Stoeckenius et al., 1979),
533 evidences were sought in the past half century to explain how the absorbed photon
534 energy is used to alter the proton affinity landscape along its pathway so that protons
535 can flow in one direction along an ascending order of pK_a values. Neither a hydraulic
536 powered noria or an animal powered sakia in the old time, nor an electric powered
537 fluid pump in the modern days, works under such an operating principle that requires
538 energy for a reconstruction of the landscape. Quite the contrary, the landscape is a
539 given constant and energy is absorbed by the to-be-pumped substance to gain its
540 potential energy, such as water is lifted by a noria or pressurized by an electric pump.
541 The energized substance will then flow freely along the largely constant landscape
542 governed by thermodynamics. In the meanwhile, it is critical to prevent a backflow

543 along a far steeper gradient than the forward-driving gradient. The molecular pump
544 bacteriorhodopsin (bR) for protons works under the exact same principle that
545 fundamentally differs from what Jardetzky and Stoeckenius once imagined. Other
546 transmembrane molecular pumps and transporters likely work the same way at this
547 philosophical level disregarding any molecular detail. Alteration of affinities to the
548 pumped substance cannot be an effective strategy because it is against the chemical
549 nature along the translocation pathway and therefore energetically difficult to achieve.
550 For example, the pK_a values differ more than 11 pH units at the resting state between
551 the protonated SB and the Asp acids, the proton acceptors. That is to say, a
552 photoinduced reduction of one million times to the proton affinity of the SB must occur
553 simultaneously with an increase of one million times to the proton affinity of the
554 carboxylates. Even if these changes in proton affinity are achievable, there will be 10%
555 failed attempts of proton transfers at a prolonged equilibrium. The proton levee,
556 consisting of a few tyrosine residues, main chain carbonyls, and most importantly,
557 Arg82, is strategically constructed around the inner EC channel to prevent proton
558 backflow (Fig. 5). Their high pK_a values are not meant to be changed even though small
559 changes could be detected. In this study, the assumption of an affinity-driven proton
560 conductance is replaced by a mechanism of concentration-driven proton conductance
561 that is not necessarily synchronous to the early photocycles.

562
563 All chemical reactions involve energy transfer or conversion, known as enthalpy
564 change ΔH . This flow of energy in a unit time is the temporal rate of enthalpy change
565 dH/dt or power as a function of time. This function is usually far from a constant. The
566 peak power of a chemical reaction could be orders of magnitude greater than its
567 average power. This is particularly true for each individual molecular event compared
568 to a molecular ensemble. Consider the photochemical reaction of the retinal
569 isomerization in bR. Its peak power is reached at the U-turn of the SB (Figs. 2a and S2),
570 which accomplishes the initial deprotonation of each photocycle. The protein structure
571 of bR prevents a photochemical reaction from reaching its equilibrium as the
572 photoisomerization of the retinal switches the accessibility of the Schiff base to a
573 different reaction space. This is usually unachievable in chemical reactions of small
574 molecules.
575

576 **Acknowledgements**

577 This work is supported in part by the grant R01EY024363 from National Institutes of
578 Health. The following database and software are used in this work: CCP4 (ccp4.ac.uk),
579 Coot (www2.mrc-lmb.cam.ac.uk/Personal/pemsley/coot), dynamix™ (Renz Research,
580 Inc.), gnuplot (gnuplot.info), PDB (rcsb.org), PHENIX (phenix-online.org), PyMOL
581 (pymol.org), Python (python.org), and SciPy (scipy.org).

582
583 **Competing interests**

584 ZR is the founder of Renz Research, Inc. that currently holds the copyright of the
585 computer software dynamix™.

586
587 **References**

- 588 Adams, P.D., Afonine, P.V., Bunkóczy, G., Chen, V.B., Davis, I.W., Echols, N., Headd, J.J., Hung, L.-W.,
589 Kapral, G.J., Grosse-Kunstleve, R.W., et al. (2010). PHENIX: a comprehensive Python-based system for
590 macromolecular structure solution. *Acta Crystallogr. D Biol. Crystallogr.* *D66*, 213–221.
- 591 Applebury, M.L., Peters, K.S., and Rentzepis, P.M. (1978). Primary intermediates in the photochemical
592 cycle of bacteriorhodopsin. *Biophys. J.* *23*, 375–382.
- 593 Balashov, S.P., Govindjee, R., Kono, M., Imasheva, E., Lukashov, E., Ebrey, T.G., Crouch, R.K., Menick,
594 D.R., and Feng, Y. (1993). Effect of the arginine-82 to alanine mutation in bacteriorhodopsin on dark
595 adaptation, proton release, and the photochemical cycle. *Biochemistry* *32*, 10331–10343.
- 596 Balashov, S.P., Imasheva, E.S., Govindjee, R., and Ebrey, T.G. (1996). Titration of aspartate-85 in
597 bacteriorhodopsin: what it says about chromophore isomerization and proton release. *Biophys. J.* *70*, 473–
598 481.
- 599 Balashov, S.P., Imasheva, E.S., Ebrey, T.G., Chen, N., Menick, D.R., and Crouch, R.K. (1997). Glutamate-
600 194 to cysteine mutation inhibits fast light-induced proton release in bacteriorhodopsin. *Biochemistry* *36*,
601 8671–8676.
- 602 van den Berg, R., Du-Jeon-Jang, Bitting, H.C., and El-Sayed, M.A. (1990). Subpicosecond resonance
603 Raman spectra of the early intermediates in the photocycle of bacteriorhodopsin. *Biophys. J.* *58*, 135–141.
- 604 Berman, H.M., Kleywegt, G.J., Nakamura, H., and Markley, J.L. (2012). The Protein Data Bank at 40:
605 Reflecting on the Past to Prepare for the Future. *Structure* *20*, 391–396.
- 606 Braiman, M.S., Mogi, T., Marti, T., Stern, L.J., Khorana, H.G., and Rothschild, K.J. (1988). Vibrational
607 spectroscopy of bacteriorhodopsin mutants: light-driven proton transport involves protonation changes
608 of aspartic acid residues 85, 96, and 212. *Biochemistry* *27*, 8516–8520.
- 609 Braiman, M.S., Bousche, O., and Rothschild, K.J. (1991). Protein dynamics in the bacteriorhodopsin
610 photocycle: submillisecond Fourier transform infrared spectra of the L, M, and N photointermediates.
611 *Proc. Natl. Acad. Sci.* *88*, 2388–2392.
- 612 Brown, L.S., Bonet, L., Needleman, R., and Lanyi, J.K. (1993). Estimated acid dissociation constants of the
613 Schiff base, Asp-85, and Arg-82 during the bacteriorhodopsin photocycle. *Biophys. J.* *65*, 124–130.

- 614 Chandonia, J.-M., and Brenner, S.E. (2006). The impact of structural genomics: expectations and
615 outcomes. *Science* 311, 347–351.
- 616 Dickopf, S., Alexiev, U., Krebs, M.P., Otto, H., Mollaaghababa, R., Khorana, H.G., and Heyn, M.P. (1995).
617 Proton transport by a bacteriorhodopsin mutant, aspartic acid-85-->asparagine, initiated in the
618 unprotonated Schiff base state. *Proc. Natl. Acad. Sci.* 92, 11519–11523.
- 619 Druckmann, S., Ottolenghi, M., Pande, A., Pande, J., and Callender, R.H. (1982). Acid-base equilibrium of
620 the Schiff base in bacteriorhodopsin. *Biochemistry* 21, 4953–4959.
- 621 Ernst, O.P., Lodowski, D.T., Elstner, M., Hegemann, P., Brown, L.S., and Kandori, H. (2014). Microbial
622 and animal rhodopsins: Structures, functions, and molecular mechanisms. *Chem. Rev.* 114, 126–163.
- 623 Fahmy, K., Weidlich, O., Engelhard, M., Tittor, J., Oesterhelt, D., and Siebert, F. (1992). Identification of
624 the proton acceptor of Schiff base deprotonation in bacteriorhodopsin: A Fourier-transform-infrared
625 study of the mutant Asp85 → Glu in its natural lipid environment. *Photochem. Photobiol.* 56, 1073–1083.
- 626 Fenno, L., Yizhar, O., and Deisseroth, K. (2011). The development and application of optogenetics. *Annu.*
627 *Rev. Neurosci.* 34, 389–412.
- 628 Friedrich, D., Brünig, F.N., Nieuwkoop, A.J., Netz, R.R., Hegemann, P., and Oschkinat, H. (2020).
629 Collective exchange processes reveal an active site proton cage in bacteriorhodopsin. *Commun. Biol.* 3, 4.
- 630 Garczarek, F., Wang, J., El-Sayed, M.A., and Gerwert, K. (2004). The Assignment of the Different Infrared
631 Continuum Absorbance Changes Observed in the 3000–1800-cm⁻¹ Region during the Bacteriorhodopsin
632 Photocycle. *Biophys. J.* 87, 2676–2682.
- 633 Garczarek, F., Brown, L.S., Lanyi, J.K., and Gerwert, K. (2005). Proton binding within a membrane protein
634 by a protonated water cluster. *Proc. Natl. Acad. Sci.* 102, 3633–3638.
- 635 Ge, X., and Gunner, M.R. (2016). Unraveling the mechanism of proton translocation in the extracellular
636 half-channel of bacteriorhodopsin: Proton translocation in bacteriorhodopsin. *Proteins Struct. Funct.*
637 *Bioinforma.* 84, 639–654.
- 638 Gerwert, K., Hess, B., Soppa, J., and Oesterhelt, D. (1989). Role of aspartate-96 in proton translocation by
639 bacteriorhodopsin. *Proc. Natl. Acad. Sci.* 86, 4943–4947.
- 640 Gerwert, K., Souvignier, G., and Hess, B. (1990). Simultaneous monitoring of light-induced changes in
641 protein side-group protonation, chromophore isomerization, and backbone motion of bacteriorhodopsin
642 by time-resolved Fourier-transform infrared spectroscopy. *Proc. Natl. Acad. Sci.* 87, 9774–9778.
- 643 Glynn, C., and Rodriguez, J.A. (2019). Data-driven challenges and opportunities in crystallography.
644 *Emerg. Top. Life Sci.* ETL20180177.
- 645 Govindjee, R., Balashov, S.P., and Ebrey, T.G. (1990). Quantum efficiency of the photochemical cycle of
646 bacteriorhodopsin. *Biophys. J.* 58, 597–608.
- 647 Govindjee, R., Misra, S., Balashov, S.P., Ebrey, T.G., Crouch, R.K., and Menick, D.R. (1996). Arginine-82
648 regulates the pK_a of the group responsible for the light-driven proton release in bacteriorhodopsin.
649 *Biophys. J.* 71, 1011–1023.
- 650 Grigorieff, N., Ceska, T.A., Downing, K.H., Baldwin, J.M., and Henderson, R. (1996). Electron-
651 crystallographic refinement of the structure of bacteriorhodopsin. *J. Mol. Biol.* 259, 393–421.
- 652 Hackett, N.R., Stern, L.J., Chao, B.H., Kronis, K.A., and Khorana, H.G. (1987). Structure-function studies
653 on bacteriorhodopsin. V. Effects of amino acid substitutions in the putative helix F. *J. Biol. Chem.* 262,
654 9277–9284.

- 655 Henderson, R., and Unwin, P.N.T. (1975). Three-dimensional model of purple membrane obtained by
656 electron microscopy. *Nature* 257, 28–32.
- 657 Henderson, R., Baldwin, J.M., Ceska, T.A., Zemlin, F., Beckmann, E., and Downing, K.H. (1990). Model
658 for the structure of bacteriorhodopsin based on high-resolution electron cryo-microscopy. *J. Mol. Biol.*
659 213, 899–929.
- 660 Henry, E.R., and Hofrichter, J. (1992). Singular value decomposition: Application to analysis of
661 experimental data. In *Numerical Computer Methods*, (Academic Press), pp. 129–192.
- 662 Jardetzky, O. (1966). Simple allosteric model for membrane pumps. *Nature* 211, 969–970.
- 663 Jung, Y.O., Lee, J.H., Kim, J., Schmidt, M., Moffat, K., Šrajer, V., and Ihee, H. (2013). Volume-conserving
664 trans-cis isomerization pathways in photoactive yellow protein visualized by picosecond X-ray
665 crystallography. *Nat. Chem.* 5, 212–220.
- 666 Kahan, A., Nahmias, O., Friedman, N., Sheves, M., and Ruhman, S. (2007). Following photoinduced
667 dynamics in bacteriorhodopsin with 7-fs impulsive vibrational spectroscopy. *J. Am. Chem. Soc.* 129, 537–
668 546.
- 669 Kandori, H. (2015). Ion-pumping microbial rhodopsins. *Front. Mol. Biosci.* 2.
- 670 Kobayashi, T., Saito, T., and Ohtani, H. (2001). Real-time spectroscopy of transition states in
671 bacteriorhodopsin during retinal isomerization. *Nature* 414, 531–534.
- 672 Kovacs, G.N., Colletier, J.-P., Grünbein, M.L., Yang, Y., Stensitzki, T., Batyuk, A., Carbajo, S., Doak, R.B.,
673 Ehrenberg, D., Foucar, L., et al. (2019). Three-dimensional view of ultrafast dynamics in photoexcited
674 bacteriorhodopsin. *Nat. Commun.* 10, 3177.
- 675 Lanyi, J.K., and Schobert, B. (2007). Structural changes in the L photointermediate of bacteriorhodopsin. *J.*
676 *Mol. Biol.* 365, 1379–1392.
- 677 Lewis, A., Spoonhower, J., Bogomolni, R.A., Lozier, R.H., and Stoeckenius, W. (1974). Tunable laser
678 resonance Raman spectroscopy of bacteriorhodopsin. *Proc. Natl. Acad. Sci.* 71, 4462–4466.
- 679 Li, Y.-T., Tian, Y., Tian, H., Tu, T., Gou, G.-Y., Wang, Q., Qiao, Y.-C., Yang, Y., and Ren, T.-L. (2018). A
680 review on bacteriorhodopsin-based bioelectronic devices. *Sensors* 18, 1368.
- 681 Liebschner, D., Afonine, P.V., Baker, M.L., Bunkóczi, G., Chen, V.B., Croll, T.I., Hintze, B., Hung, L.-W.,
682 Jain, S., McCoy, A.J., et al. (2019). Macromolecular structure determination using X-rays, neutrons and
683 electrons: recent developments in Phenix. *Acta Crystallogr. Sect. Struct. Biol.* 75, 861–877.
- 684 Lorenz-Fonfria, V.A., Saita, M., Lazarova, T., Schlesinger, R., and Heberle, J. (2017). pH-sensitive
685 vibrational probe reveals a cytoplasmic protonated cluster in bacteriorhodopsin. *Proc. Natl. Acad. Sci.*
686 114, E10909–E10918.
- 687 Lozier, R.H., Bogomolni, R.A., and Stoeckenius, W. (1975). Bacteriorhodopsin: a light-driven proton
688 pump in *Halobacterium Halobium*. *Biophys. J.* 15, 955–962.
- 689 Luecke, H., Schobert, B., Richter, H.-T., Cartailler, J.-P., and Lanyi, J.K. (1999a). Structure of
690 bacteriorhodopsin at 1.55 Å resolution. *J. Mol. Biol.* 291, 899–911.
- 691 Luecke, H., Schobert, B., Richter, H.-T., Cartailler, J.-P., and Lanyi, J.K. (1999b). Structural changes in
692 bacteriorhodopsin during ion transport at 2 angstrom resolution. *Science* 286, 255–260.

Ren: Concentration-driven proton conductance

- 693 Luecke, H., Schobert, B., Cartailler, J.-P., Richter, H.-T., Rosengarth, A., Needleman, R., and Lanyi, J.K.
694 (2000). Coupling photoisomerization of retinal to directional transport in bacteriorhodopsin. *J. Mol. Biol.*
695 *300*, 1237–1255.
- 696 Marti, T., Otto, H., Mogi, T., Rösselet, S.J., Heyn, M.P., and Khorana, H.G. (1991). Bacteriorhodopsin
697 mutants containing single substitutions of serine or threonine residues are all active in proton
698 translocation. *J. Biol. Chem.* *266*, 6919–6927.
- 699 Marx, D., Tuckerman, M.E., Hutter, J., and Parrinello, M. (1999). The nature of the hydrated excess proton
700 in water. *Nature* *397*, 601–604.
- 701 Mathias, G., and Marx, D. (2007). Structures and spectral signatures of protonated water networks in
702 bacteriorhodopsin. *Proc. Natl. Acad. Sci.* *104*, 6980–6985.
- 703 McCarty, C.G. (1970). Chapter 9 syn-anti isomerizations and rearrangements. In *The Chemistry of the*
704 *Carbon-Nitrogen Double Bond*, (John Wiley & Sons, Ltd), p. 363.
- 705 Moffat, K. (1989). Time-Resolved Macromolecular Crystallography. *Annu. Rev. Biophys. Biophys. Chem.*
706 *18*, 309–332.
- 707 Moffat, K. (2001). Time-resolved biochemical crystallography: A mechanistic perspective. *Chem Rev* *101*,
708 1569–1582.
- 709 Mogi, T., Stern, L.J., Marti, T., Chao, B.H., and Khorana, H.G. (1988). Aspartic acid substitutions affect
710 proton translocation by bacteriorhodopsin. *Proc. Natl. Acad. Sci.* *85*, 4148–4152.
- 711 Nango, E., Royant, A., Kubo, M., Nakane, T., Wickstrand, C., Kimura, T., Tanaka, T., Tono, K., Song, C.,
712 Tanaka, R., et al. (2016). A three-dimensional movie of structural changes in bacteriorhodopsin. *Science*
713 *354*, 1552–1557.
- 714 Nogly, P., Weinert, T., James, D., Carbajo, S., Ozerov, D., Furrer, A., Gashi, D., Borin, V., Skopintsev, P.,
715 Jaeger, K., et al. (2018). Retinal isomerization in bacteriorhodopsin captured by a femtosecond x-ray laser.
716 *Science* *361*, eaat0094.
- 717 Pebay-Peyroula, E., Rummel, G., Rosenbusch, J.P., and Landau, E.M. (1997). X-ray structure of
718 bacteriorhodopsin at 2.5 Angstroms from microcrystals grown in lipidic cubic phases. *Science* *277*, 1676–
719 1681.
- 720 Ren, Z. (2013a). Reaction trajectory revealed by a joint analysis of Protein Data Bank. *PLoS ONE* *8*, e77141.
- 721 Ren, Z. (2013b). Reverse engineering the cooperative machinery of human hemoglobin. *PLoS ONE* *8*,
722 e77363.
- 723 Ren, Z. (2016). Molecular events during translocation and proofreading extracted from 200 static
724 structures of DNA polymerase. *Nucleic Acids Res.* *6*, 1–13.
- 725 Ren, Z. (2019). Ultrafast structural changes decomposed from serial crystallographic data. *J. Phys. Chem.*
726 *Lett.* *10*, 7148–7163.
- 727 Ren, Z. (2021). Photoinduced isomerization sampling of retinal in bacteriorhodopsin. *BioRxiv*
728 doi:10.1101/2021.09.16.460656.
- 729 Ren, Z., Perman, B., Srajer, V., Teng, T.-Y., Praderyand, C., Bourgeois, D., Schotte, F., Ursby, T., Kort, R.,
730 Wulff, M., et al. (2001). A molecular movie at 1.8 Å resolution displays the photocycle of photoactive
731 yellow protein, a eubacterial blue-light receptor, from nanoseconds to seconds. *Biochemistry* *40*, 13788–
732 13801.

Ren: Concentration-driven proton conductance

- 733 Ren, Z., Chan, P.W.Y., Moffat, K., Pai, E.F., Royer, W.E., Šrajer, V., and Yang, X. (2013). Resolution of
734 structural heterogeneity in dynamic crystallography. *Acta Cryst D69*, 946–959.
- 735 Ren, Z., Ren, P.X., Balusu, R., and Yang, X. (2016). Transmembrane helices tilt, bend, slide, torque, and
736 unwind between functional states of rhodopsin. *Sci. Rep.* 6, 34129.
- 737 Ren, Z., Ayhan, M., Bandara, S., Bowatte, K., Kumarapperuma, I., Gunawardana, S., Shin, H., Wang, C.,
738 Zeng, X., and Yang, X. (2018). Crystal-on-crystal chips for in situ serial diffraction at room temperature.
739 *Lab. Chip* 18, 2246–2256.
- 740 Richter, H.T., Needleman, R., and Lanyi, J.K. (1996). Perturbed interaction between residues 85 and 204 in
741 Tyr-185-->Phe and Asp-85-->Glu bacteriorhodopsins. *Biophys. J.* 71, 3392–3398.
- 742 Royant, A., Edman, K., Ursby, T., Pebay-Peyroula, E., Landau, E.M., and Neutze, R. (2000). Helix
743 deformation is coupled to vectorial proton transport in the photocycle of bacteriorhodopsin. *Nature* 406,
744 645–648.
- 745 Sass, H.J., Büldt, G., Gessenich, R., Hehn, D., Neff, D., Schlesinger, R., Berendzen, J., and Ormos, P. (2000).
746 Structural alterations for proton translocation in the M state of wild-type bacteriorhodopsin. *Nature* 406,
747 649–653.
- 748 Schaffer, J.E., Kukshal, V., Miller, J.J., Kitainda, V., and Jez, J.M. (2021). Beyond X-rays: an overview of
749 emerging structural biology methods. *Emerg. Top. Life Sci.* ETL20200272.
- 750 Schmidt, M., Rajagopal, S., Ren, Z., and Moffat, K. (2003). Application of singular value decomposition to
751 the analysis of time-resolved macromolecular X-ray data. *Biophys. J.* 84, 2112–2129.
- 752 Schmidt, M., Graber, T., Henning, R., and Srajer, V. (2010). Five-dimensional crystallography. *Acta*
753 *Crystallogr. A* 66, 198–206.
- 754 Sheves, M., Albeck, A., Friedman, N., and Ottolenghi, M. (1986). Controlling the pKa of the
755 bacteriorhodopsin Schiff base by use of artificial retinal analogues. *Proc. Natl. Acad. Sci.* 83, 3262–3266.
- 756 Shin, H., Ren, Z., Zeng, X., Bandara, S., and Yang, X. (2019). Structural basis of molecular logic OR in a
757 dual-sensor histidine kinase. *Proc. Natl. Acad. Sci.* 116, 19973–19982.
- 758 Šrajer, V., Ren, Z., Teng, T.-Y., Schmidt, M., Ursby, T., Bourgeois, D., Pradervand, C., Schildkamp, W.,
759 Wulff, M., and Moffat, K. (2001). Protein conformational relaxation and ligand migration in myoglobin: A
760 nanosecond to millisecond molecular movie from time-resolved Laue X-ray diffraction. *Biochemistry* 40,
761 13802–13815.
- 762 Stoeckenius, W. (1999). Bacterial rhodopsins: Evolution of a mechanistic model for the ion pumps. *Protein*
763 *Sci.* 8, 447–459.
- 764 Stoeckenius, W., Lozier, R.H., and Bogomolni, R.A. (1979). Bacteriorhodopsin and the purple membrane
765 of halobacteria. *Biochim. Biophys. Acta BBA - Rev. Bioenerg.* 505, 215–278.
- 766 Su, T., and Purohit, P.K. (2009). Mechanics of forced unfolding of proteins. *Acta Biomater.* 5, 1855–1863.
- 767 Takahashi, H., Rico, F., Chipot, C., and Scheuring, S. (2018). α -Helix Unwinding as Force Buffer in
768 Spectrins. *ACS Nano* 12, 2719–2727.
- 769 Takeda, K., Matsui, Y., Kamiya, N., Adachi, S., Okumura, H., and Kouyama, T. (2004). Crystal structure of
770 the M intermediate of bacteriorhodopsin: Allosteric structural changes mediated by sliding movement of
771 a transmembrane helix. *J. Mol. Biol.* 341, 1023–1037.

Ren: Concentration-driven proton conductance

- 772 Ursby, T., and Bourgeois, D. (1997). Improved estimation of structure-factor difference amplitudes from
773 poorly accurate data. *Acta Crystallogr. A* 53, 564–575.
- 774 Wang, J., and El-Sayed, M.A. (2001). Time-Resolved Fourier Transform Infrared Spectroscopy of the
775 Polarizable Proton Continua and the Proton Pump Mechanism of Bacteriorhodopsin. *Biophys. J.* 80, 961–
776 971.
- 777 Weinert, T., Skopintsev, P., James, D., Dworkowski, F., Panepucci, E., Kekilli, D., Furrer, A., Brünle, S.,
778 Mous, S., Ozerov, D., et al. (2019). Proton uptake mechanism in bacteriorhodopsin captured by serial
779 synchrotron crystallography. *Science* 365, 61–65.
- 780 Wickstrand, C., Dods, R., Royant, A., and Neutze, R. (2015). Bacteriorhodopsin: Would the real structural
781 intermediates please stand up? *Biochim. Biophys. Acta* 1850, 536–553.
- 782 Yang, X., Ren, Z., Kuk, J., and Moffat, K. (2011). Temperature-scan cryocrystallography reveals reaction
783 intermediates in bacteriophytochrome. *Nature* 479, 428–432.
- 784 Zhong, Q., Ruhman, S., Ottolenghi, M., Sheves, M., Friedman, N., Atkinson, G.H., and Delaney, J.K.
785 (1996). Reexamining the primary light-induced events in bacteriorhodopsin using a synthetic C13=C14-
786 locked chromophore. *J Am Chem Soc* 118, 12828–12829.
- 787 Zimanyi, L., Varo, G., Chang, M., Ni, B., Needleman, R., and Lanyi, J.K. (1992). Pathways of proton
788 release in the bacteriorhodopsin photocycle. *Biochemistry* 31, 8535–8543.
- 789
- 790

791 **Directional Proton Conductance in Bacteriorhodopsin Is Driven by**
792 **Concentration Gradient, Not Affinity Gradient**

793

794 Zhong Ren

795

796 Department of Chemistry, University of Illinois at Chicago, Chicago, IL 60607, USA

797 Renz Research, Inc., Westmont, IL 60559, USA

798

799 zren@uic.edu

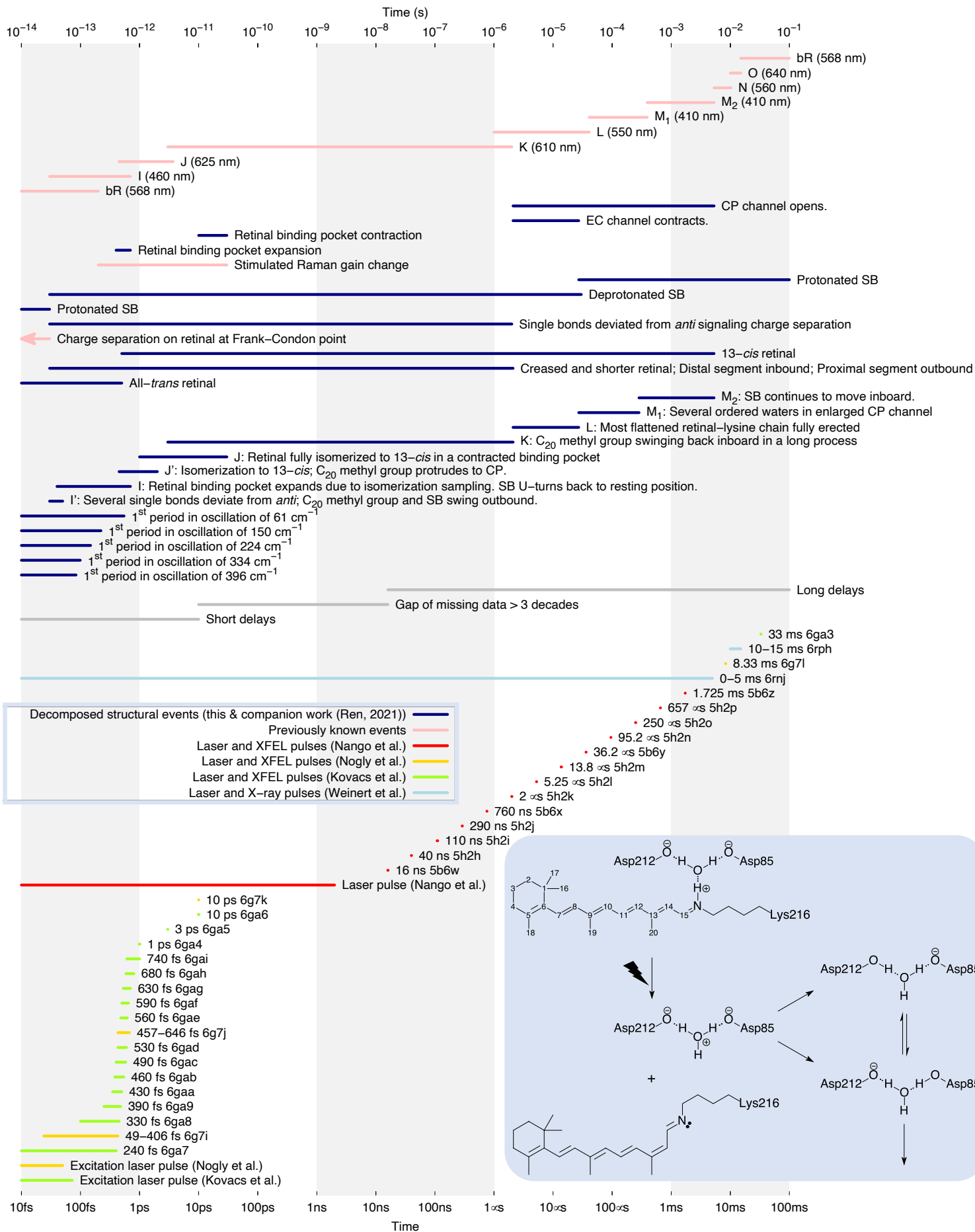
800 ORCID 0000-0001-7098-3127

801

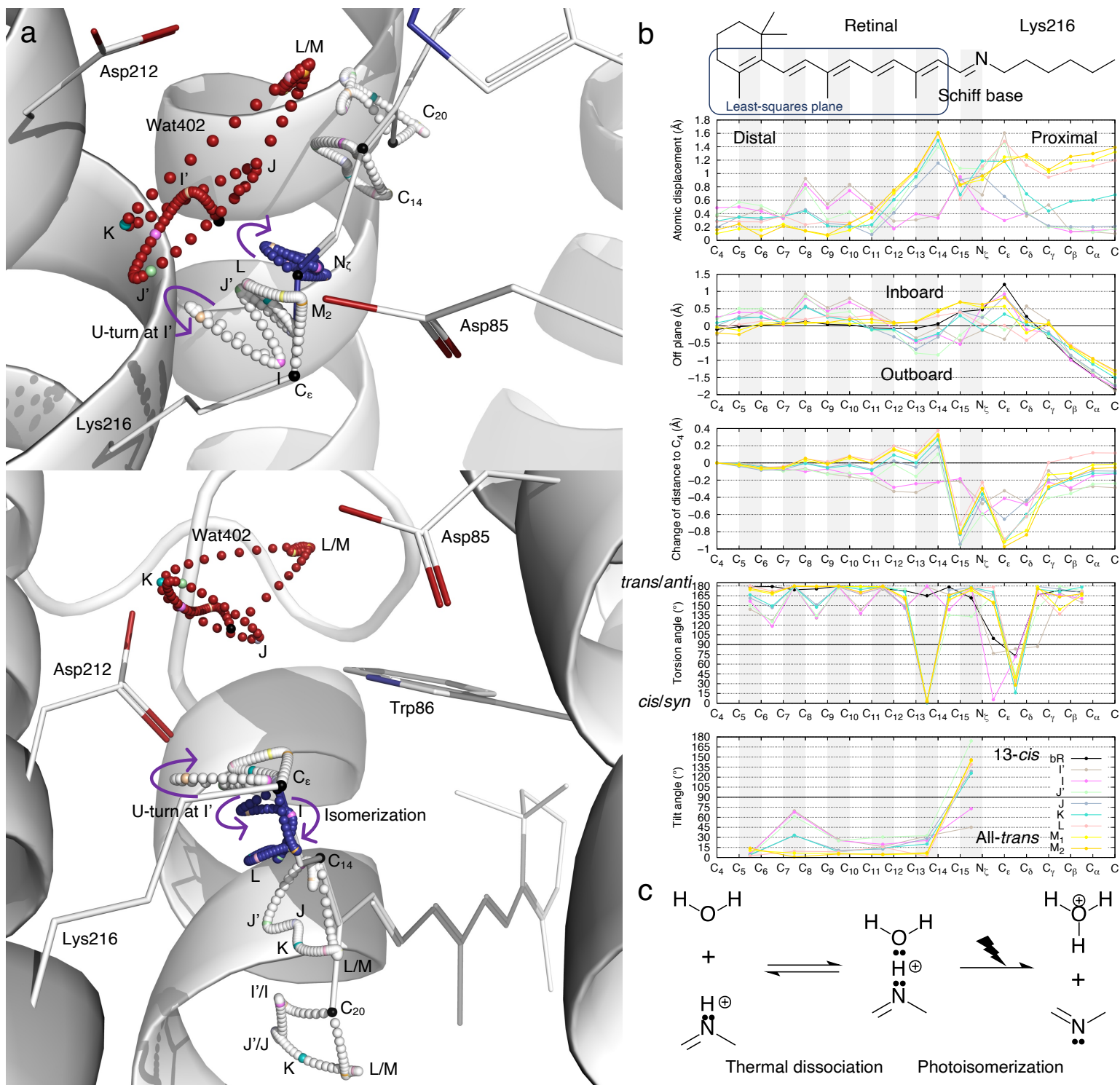
802 **Figures and Legends**

803

Ren: Concentration-driven proton conductance



805 Figure 1. Gantt chart summarizing analyzed datasets and results. (Inset) Proposed
806 scheme of deprotonation from SB. Deprotonation occurs at I' around ~30 fs to form a
807 transient hydronium ion (Fig. 2c). Another proton is transferred to either Asp85 or 212,
808 between which an equilibrium is maintained over time. A second deprotonation in the
809 next photocycle causes both Asp residues to be neutralized. One or more waters in the
810 inner EC channel become overcharged with excess protons during the subsequent
811 photocycles. A super-acidic inner EC channel then causes a second protonation of
812 Arg82 to form a divalent guanidinium cation. The positive charged guanidinium group
813 is attracted to the negative charged Glu residues in the outer EC channel and swings
814 outward to form a salt bridge. The extra proton is discharged to the EC medium
815 through the Glu residues and several waters in the outer EC channel, known as the
816 proton release complex. The monovalent guanidinium returns for the next shuttling
817 (Fig. 5).
818
819

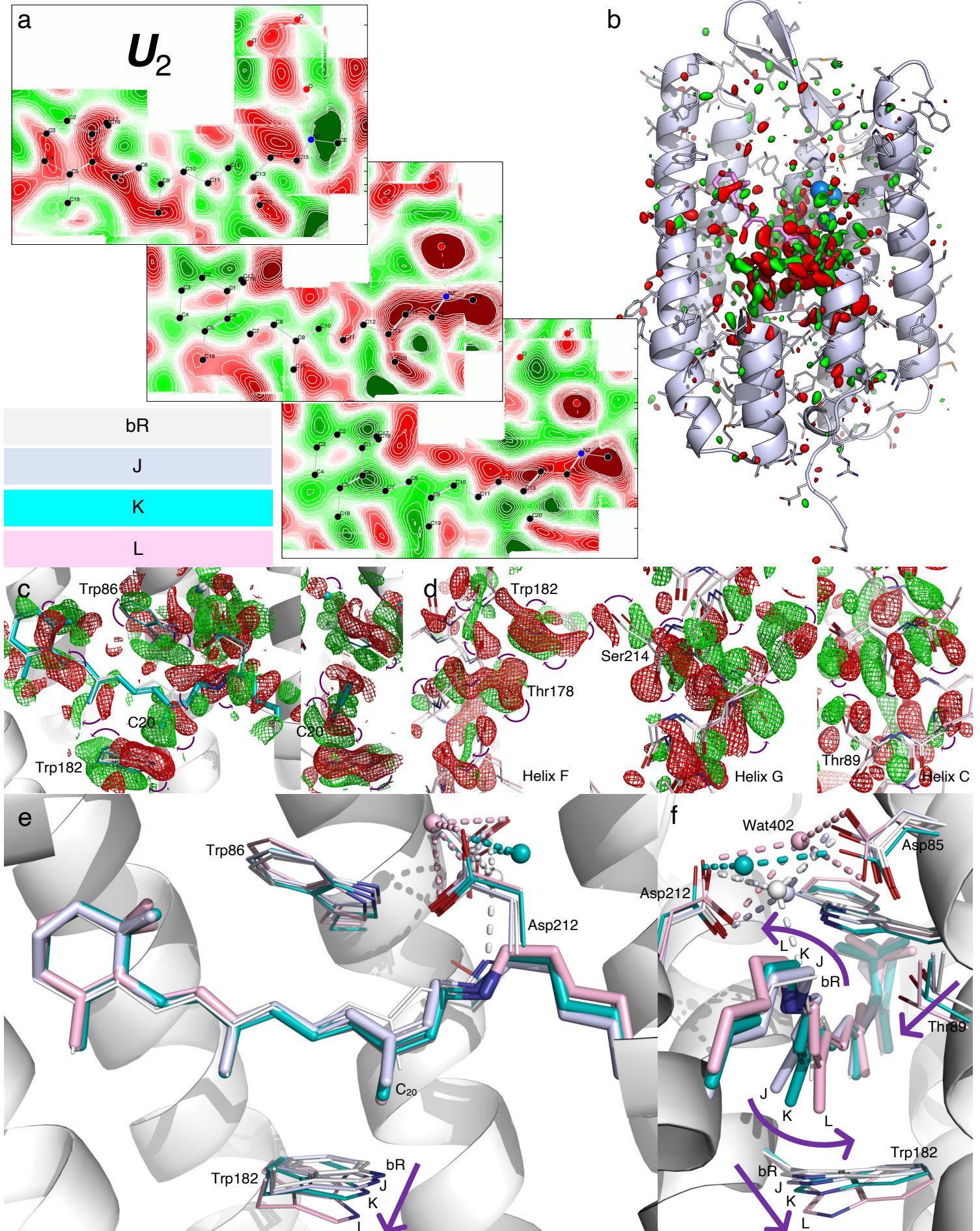


821
 822 Figure 2. Trajectories of bacteriorhodopsin photocycle. (a) Two orthographical views of
 823 refined atomic trajectories. bR structure in the resting state is rendered in white ribbon
 824 and sticks. The photocycle trajectories of several atoms of the chromophore C₁₄, C₂₀, C_ε,

825 N_{ζ} and Wat402 are rendered as small spheres. Their positions in the ground state bR
826 are in black. The intermediates I', I, J', J, K, L, M₁, and M₂ are colored differently. This
827 color scheme (key in b) is consistently applied to all figures in this paper. Other small
828 spheres along the atomic trajectories are in white for C, blue for N, and red for O. (b)
829 Conformational parameters calculated from the refined chromophore. The chemical
830 structure of the chromophore on top is aligned to the horizontal axis. Double bonds are
831 shaded in gray. Atomic displacements of each intermediate from the resting state show
832 greater changes in the proximal segment (top panel). A plane is least-squares fitted to
833 C₄ through C₁₄ of the resting state. This retinal plane is largely parallel to the three-fold
834 axis of bR trimer. Therefore, one side of the plane where the three-fold axis is located is
835 called inboard, and the opposite side of the plane away from the three-fold axis is called
836 outboard (Ren, 2021). The distances of all atoms to this plane in the inboard and
837 outboard directions show the curvature of the chromophore. The creased retinal in the
838 early intermediates and the inboard protruding corner at C_ε in the resting state are
839 clearly shown (2nd panel). Distances to atom C₄ are calculated for all refined
840 chromophores. Changes in these distances with respect to the resting state show the
841 shortened chromophore in I' and I. Once isomerization to 13-*cis* occurs, the segment
842 from C₁₅ to C₈ around the SB becomes significantly closer to the β-ionone ring, while the
843 distal segment of the retinal from C₁₄ and beyond stretches (3rd panel). The torsion
844 angles of single and double bonds quantify *anti/syn* or *trans/cis* for the ground state and
845 all intermediates. Only a single bond can be twisted with its torsion angle near 90°. A
846 double bond would spend very little time at a torsion angle near 90° compared to *trans*
847 or *cis* configurations thus not easily observed (4th panel). Each double bond is least-
848 squares fitted with a plane. The interplanar angle between one double bond and the
849 corresponding one in the ground state measures the local tilting of the retinal (bottom
850 panel). (c) Deprotonation from the Schiff base. In the resting state, a proton is situated
851 between the SB N_{ζ} and the O of Wat402. Two lone pairs of electrons from N and O,
852 respectively, are interacting with the proton. During thermal dissociation to the left, the
853 proton stays with the SB with greater probability due to its greater proton affinity. This
854 thermal process does not cause deprotonation from the SB, and it could revert. On the
855 other hand, when the SB is abruptly displaced by the photoisomerization as observed
856 here at ~30 fs (a), the proton inertia tips the balance of these two interactions. The
857 proton cannot overcome its association with the water and accelerate fast enough with
858 the SB. As a result, it stays with Wat402 to form a hydronium ion. This deprotonation

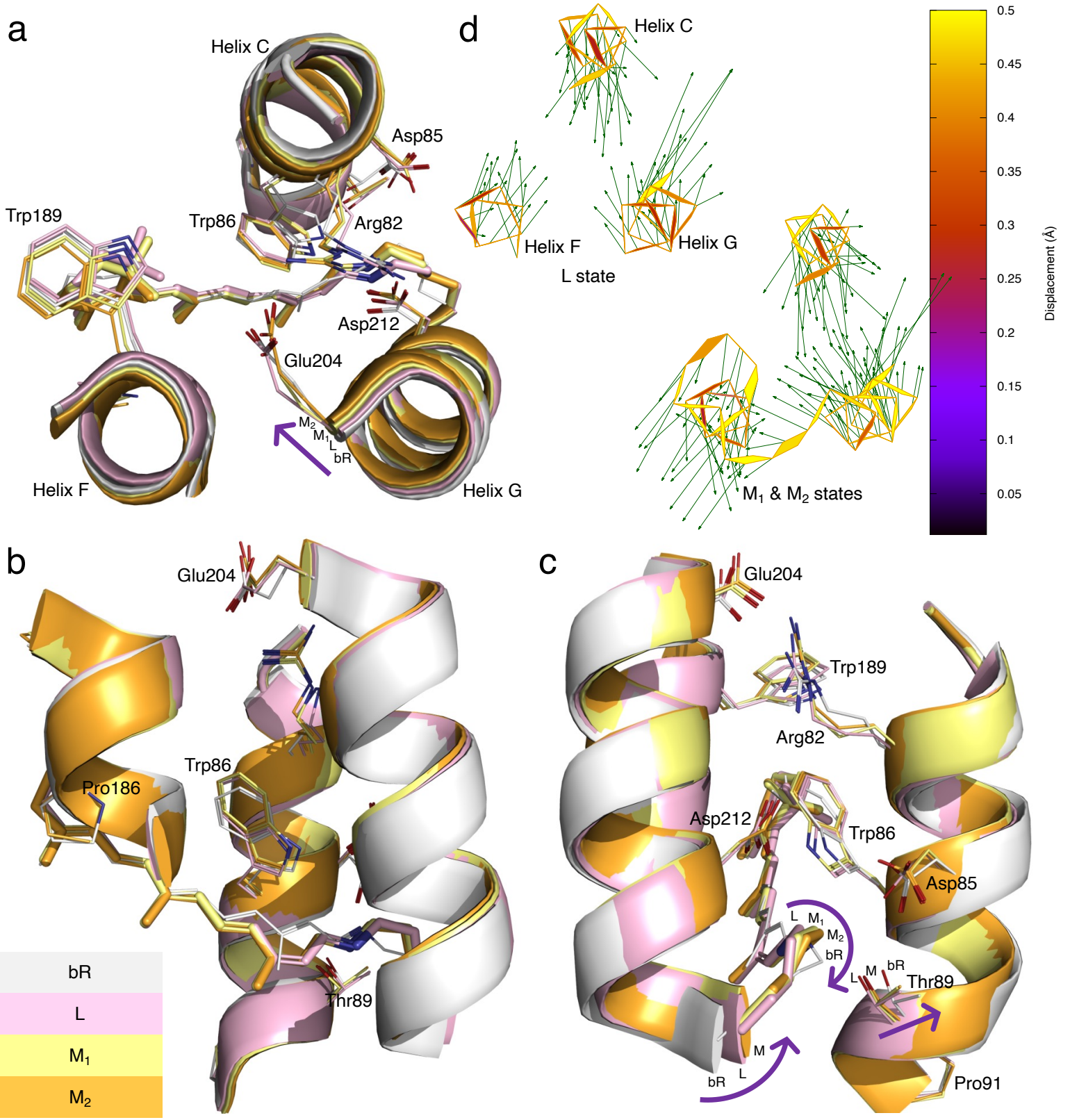
859 from the SB to the right is not governed by the proton affinities of two competing
860 moieties based on chemical equilibrium. In addition, this process does not revert as the
861 photoisomerization makes the SB no longer accessible from the EC half channel.
862

Ren: Concentration-driven proton conductance



864
865 Figure 3. Intermediates J, K, and L. (a) Cross sections of component map \mathbf{U}_2 of the long
866 delays > 10 ns. The middle cross section is an integration ± 0.2 Å around the surface
867 through the retinal. The top cross section is an integration 1.4-1.8 Å outboard from the
868 retinal surface and the bottom is an integration 0.6-1 Å inboard. Green and red indicate
869 electron density gain and loss, respectively. Stronger signals are around the proximal
870 segment of the retinal, including Wat402. Positive and negative sheets of densities flank
871 the distal segment of the retinal from inboard and outboard sides, respectively. This
872 component is nearly constant in all long-delay difference maps with a dark dataset as
873 reference (Fig. S4). (b) Overview of the component map \mathbf{U}_2 of the long delays contoured
874 at $\pm 3\sigma$. The extraordinary signal-to-noise level is shown as the association with specific
875 elements of the structure. Some parts of the structure are omitted to show the interior.
876 (c) Two orthographical views of the reconstituted difference map $\mathbf{K} - \text{bR}$ from \mathbf{U}_1 , \mathbf{U}_2 ,
877 and \mathbf{U}_3 of the long delays (Fig. S5abc). The map is contoured at $\pm 2.5\sigma$ in green and red
878 mesh, respectively. Atomic displacements are indicated by the arrows marking the
879 negative and positive pairs of densities. (d) Reconstituted difference map $\mathbf{L} - \text{bR}$ from
880 \mathbf{U}_2 , \mathbf{U}_3 , and \mathbf{U}_6 of the long delays (Fig. S5bcd). The map is contoured at $\pm 3.5\sigma$ in green
881 and red mesh, respectively. The strongest signals are concentrated on the irregularities
882 of helices F, G, and C (Fig. S10). (e and f) Two orthographical views of the refined
883 retinal in J, K, and L compared with the resting state in white. The retinal is less creased
884 in K and flattened in L compared to the previous intermediates (Fig. 2b 2nd panel). C₂₀
885 methyl group is less and less tilted from its orientation in the resting state (Fig. 2b
886 bottom panel). Wat402 with good electron density (Figs. S8 and S9) remains its H-
887 bonds with both Asp85 and 212 in both K and L. Thr89 follows the motion of the SB
888 toward outboard.
889

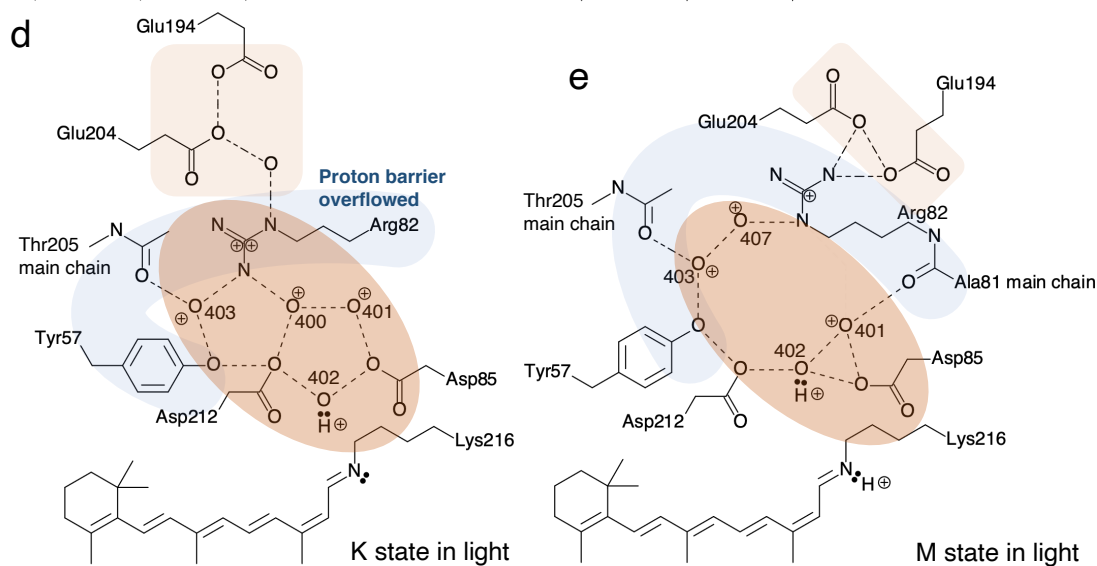
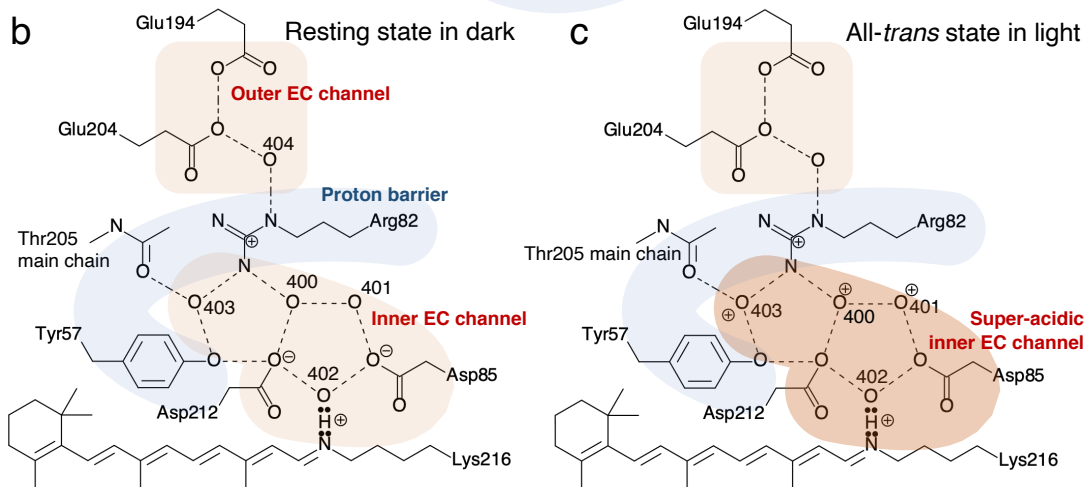
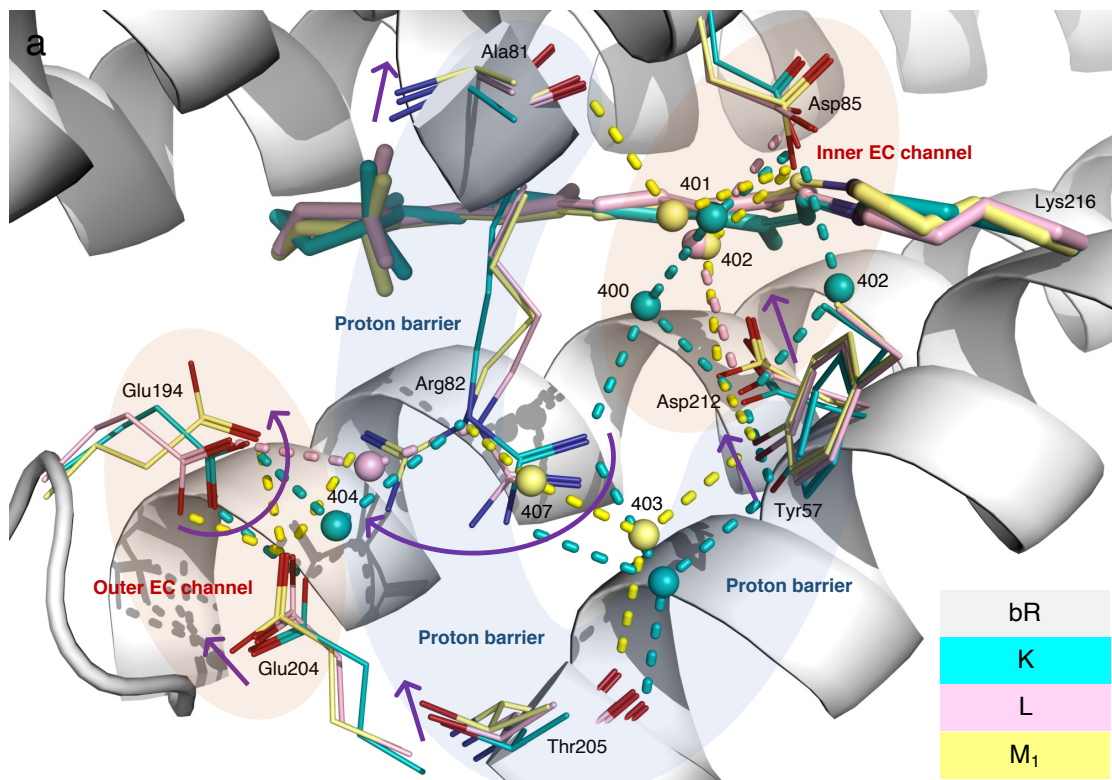
Ren: Concentration-driven proton conductance



891

892 Figure 4. Intermediates L, M₁, and M₂. (a, b, and c) Three orthographical views of EC
893 half channel. The refined structures of L, M₁, and M₂ in pink, yellow, and orange,
894 respectively, are compared to the resting state in white. Several arrows mark the
895 motions from the ground state bR to these intermediates or from these intermediates
896 back to bR. The SB is moving more and more inboard since L and finally establishes the
897 corner at C_ε protruding inboard in the ground state by isomerization back to all-*trans*.
898 Meanwhile, Thr89 and helix C are pushed away. (d) Atomic displacements in the main
899 chain around the EC half channel from the resting state to L and M are marked with
900 arrows 10× as long as the actual displacements. The EC segments of helices C and G
901 move closer to each other as Arg82 swings out. The same portion is displayed as in (a-
902 c).
903

Ren: Concentration-driven proton conductance



905
906 Figure 5. H-bond network in EC half channel. The EC half channel is decorated with
907 acidic residues, such as Asp85 and 212 at the end, called inner EC channel shaded in
908 pink, and Glu9, 194, and 204 at the EC surface, called outer EC channel also shaded in
909 pink. Arg82, Tyr57, and 83 are located between these two layers that form a proton
910 barrier shaded in blue (Fig. S1). (a) The refined structures of K in blue, L in pink, and
911 M_1 in yellow are rendered in the framework of the resting state in white. Several
912 arrows mark the motions of $K \rightarrow L \rightarrow M_1$. (b) Flattened network of resting state in dark.
913 Dashed lines mark H-bonds and salt bridges. Hydrogens, except the proton on the SB,
914 are omitted due to the ambiguity in their associations with other atoms. 400 numbers
915 are waters. A dual-pentagon of H-bond network is characteristic in the resting state.
916 The guanidinium group of Arg82 is already protonated with a positive charge at a
917 neutral pH. The phenol hydroxyl groups of Tyr cannot be protonated anymore. These
918 residues form a proton barrier shaded in blue between the inner aspartic acids and the
919 outer glutamic acids shaded in pink. The H-bond network in the EC half channel
920 connects the inner acidic residues with the outer ones through the proton barrier of
921 Arg82, Tyr57, and the main chain carbonyls of Ala81 and Thr205. No proton
922 conductance can occur in this resting state. (c) Flattened network in an all-*trans* state in
923 light. This hypothetical state only exists during continuous pumping activity in light.
924 Although its structure has not been observed, several FTIR continua previously
925 observed hint its existence. The retinal has returned to its all-*trans* configuration ready
926 to be excited for the next photocycle. Assume this state is similar to the resting state in
927 dark except that several protons have been pumped into the inner EC channel during
928 previous photocycles so that the aspartic acids are neutralized, and several waters could
929 have also been charged to become hydronium ions as shaded in brown. Although a
930 five-proton capacity is observed in the resting state, it is unknown how many excess
931 protons are required to drive the proton conductance. (d) Flattened network of K state
932 in light. The dual-pentagon H-bond network is disrupted therefore not observed in its
933 intact form in all excited states except in K. The dual pentagon is observed again in K
934 (a). Proton conductance through the proton barrier is driven by excess protons in the
935 super-acidic inner EC channel shaded in brown. The guanidinium group of Arg82 is
936 protonated for a second time under the extraordinary proton concentration. (e)
937 Flattened network of M state in light. The guanidinium group swings toward EC and
938 makes direct contact with the glutamic acids. The second extra charge on the

939 guanidinium group is conducted to the EC medium driven by affinity gradient.

940 However, the guanidinium group retains one extra proton.

941

942

943 **Directional Proton Conductance in Bacteriorhodopsin Is Driven by**
944 **Concentration Gradient, Not Affinity Gradient**

945

946 Zhong Ren

947

948 Department of Chemistry, University of Illinois at Chicago, Chicago, IL 60607, USA

949 Renz Research, Inc., Westmont, IL 60559, USA

950

951 zren@uic.edu

952 ORCID 0000-0001-7098-3127

953

954 **Supplementary Information**

955 *Intermediates K and L*

956 Emerged from J around 10 ps, K lasts more than five decades into μs , which suggests
957 that it is a struggle to achieve the next state L over a significant energy barrier. The
958 creased retinal ever since I' at the very first time point (Ren, 2021) is relaxing in K (blue;
959 Figs. 3ef and S8). This slow and difficult relaxation could be driven in part by the
960 energy stored in the creased 13-*cis* retinal and leads to global changes over the entire
961 molecule. First, C_{20} methyl group is tilting less at 20° from its resting orientation (Fig. 2b
962 bottom panel). Although protruded toward the CP direction due to the 13-*cis*
963 configuration, the tilted C_{20} in J is not pointing to Trp182 directly (Fig. 3ef). Therefore,
964 Trp182 is little affected in J. As C_{20} swings back in K, it starts to push Trp182 toward the
965 CP and causes displacements in the main chain (Fig. 3cdef). The positive density that
966 indicates the position of C_{20} in the reconstituted difference map $K - bR$ forms an arc
967 shape centered on the polyene chain (Fig. 3c). This observation strongly suggests that K
968 is a process, rather than a discrete state, with C_{20} distributed along the arc leading
969 toward the next state L, in which the methyl group is fully erected (Fig. 3ef). Second,
970 the entire chromophore in K, except the most distal segment beyond C_8 , is in a flat
971 conformation with the double bond $C_{13}=C_{14}$ in *cis* and the single bond $C_\epsilon-C_\delta$ in *syn*. 12
972 consecutive torsion angles from C_8 to C_α deviate no more than 20° from *trans/cis* or
973 *anti/syn*. The root-mean-squared deviation (rmsd) is 8.6° (Fig. 2b 4th panel). To achieve
974 such energetically favorable conformation in the chromophore, the retinal anchor
975 Lys216 is driven toward the EC direction, which causes a significant shift of the main
976 chain in the vicinity. Third, again due to the 13-*cis* configuration, Trp86 on the EC side

977 moves with the proximal segment of the retinal toward the CP direction, which also
 978 causes movement in the main chain. All three developments above are the progresses
 979 in a long and hard work toward the goal to establish the state L with global
 980 consequences.

981
 982 After five decades of time since tens of ps, the large energy barrier is finally
 983 overcome around several μs as described by the component map \mathbf{U}_3 (Fig. S5c) in the
 984 global transition of $\text{K} \rightarrow \text{L}$. This transition is modeled here at a time constant of $2 \mu\text{s}$
 985 (Fig. S7). The potential energy in the creased retinal established within tens of fs after
 986 photon absorption is spent to trigger this transition, at least in part. Other sources of
 987 potential energy, such as that stored in the bent helix C (Fig. S10a), could also drive the
 988 global transition. Strong signals in the reconstituted difference map $\text{L} - \text{bR}$ (Fig. 3d)
 989 support the refined structure of L (pink; Fig. S9). The refined structure of L shows that
 990 the 13-*cis* retinal is finally flattened as its potential energy is consumed. 12 consecutive
 991 torsion angles from C_5 to C_8 , including the SB, deviate from *trans/cis* or *syn/anti* no more
 992 than 23° with an rmsd of 10° (Fig. 2b 4th panel). As a small cost, a couple of single bonds
 993 of Lys216 have to deviate from the perfect *syn* or *anti* conformation like those in the flat
 994 all-*trans* retinal in the resting state. The plane of the flattened 13-*cis* retinal has largely
 995 returned to the original plane of the all-*trans* retinal (Fig. 2b 2nd panel). C_{20} methyl
 996 group is pointing directly to Trp182, which causes helix F to displace (Figs. 3d and
 997 S10b). Leu93 in helix C is also affected by the protruding C_{20} methyl group back into
 998 the original retinal plane. On the other hand, the fully erected C_{20} displaces the anchor
 999 helix G with equally strong signals (Figs. 3d and S10c).

1000

1001 *Intermediates M_1 and M_2*

1002 An increase of the component map \mathbf{U}_1 separating the long delays $> 10 \mu\text{s}$ from the
 1003 earlier ones is modeled as the $\text{L} \rightarrow \text{M}$ transition at a time constant of $27 \mu\text{s}$. The M state
 1004 could be split into two by an increase of the component map \mathbf{U}_6 at a time constant of 290
 1005 μs (Fig. S7). Signals in both \mathbf{U}_1 and \mathbf{U}_6 are distributed over the EC half of the molecule
 1006 instead of globally (Fig. S5ad). Two similar structures M_1 and M_2 (yellow and orange)
 1007 are refined according to the reconstituted difference maps $M_1 - \text{bR}$ and $M_2 - \text{bR}$ (Figs.
 1008 S12 and S13). Since the L state, the SB is moving inboard mainly by twisting the torsion
 1009 angle around $\text{N}_\zeta - \text{C}_\varepsilon$ (Fig. 2b 4th panel). C_ε in M_1 and M_2 has moved 0.6 and 0.8 \AA ,
 1010 respectively, from its position in L. It seems that the conformation is approaching a

1011 point poised to isomerize back to all-*trans*. In the meanwhile, Thr89 and helix C are
1012 being pushed back toward inboard, which restores the kink of helix C in the resting
1013 state (Fig. 4abc). The new development in the retinal displaces helix G further toward
1014 the EC direction as previously observed (Takeda et al., 2004). On the other hand, the
1015 stretched helix F in L springs back in M and becomes shorter than that in the resting
1016 state. The EC segment of helix F turns around to move outboard since L (Fig. 4d).
1017 However, the EC segments of helices C and G squeeze even tighter, while Arg82 swings
1018 out of the way as observed previously (Luecke et al., 2000; Sass et al., 2000).

1019

1020 *Mutant functions*

1021 Under the mechanism of proton conductance driven by concentration gradient
1022 presented here, a number of mutant functions are explained. How mutants behave, in
1023 return, further support these hypotheses. Proton pumping activity is abolished in
1024 D85N at neutral pH (Mogi et al., 1988). The remaining proton acceptor Asp212 is H-
1025 boned to the phenol hydroxy group of Tyr57 (Fig. S14). After two successful
1026 photocycles, Asp212 and Wat402 are both protonated. However, proton conductance is
1027 stopped at the carbonyl groups =O of both side chains of Asn85 and Asp212, the amide
1028 group -NH₂ of Asn85, and the hydroxy groups -OH of Tyr57 and 185, since none of
1029 them can be protonated further. The lack of a proton outlet causes the SB to be
1030 reprotonated quickly during I' or I before isomerization. The proton pump stalls with
1031 repeated futile photocycles. It has been shown that the proton pumping activity of
1032 D85N can be somewhat restored at an alkaline pH (Dickopf et al., 1995), which is
1033 consistent with the concentration-driven proton conductance proposed here. The
1034 phenol hydroxy group of Tyr57, a weak acid, could start to conduct proton to Wat403
1035 and Arg82 only at an alkaline pH by deprotonation. On the other hand, some activity
1036 remains in D212N, which suggests a proton outlet going through Asp85, Wat401, 400,
1037 Arg82, and beyond (Fig. S14). In addition, Asp to Glu mutants are harder to assess
1038 because of their severe structural impacts. Proton pumping activity is also abolished in
1039 D212A (Mogi et al., 1988) perhaps due to a more mobile Wat402 or a hydronium that
1040 reprotonates the SB before isomerization or fails to withhold the proton during the SB
1041 U-turn. This mutant function further underscores the importance that Wat402 or a
1042 hydronium ion maintains its H-bonds to both Asp 85 and 212 throughout the
1043 photocycle as observed in this study despite its large traveling trajectory (Fig. 2a).

1044

1045 Mutants at the site of Arg82 are crucial tests to the mechanisms proposed here. M
1046 formation in the wildtype is pH-dependent at a few μ s under alkaline pH and 85 μ s at
1047 neutral pH (Balashov et al., 1993; Zimanyi et al., 1992), which nicely illustrates the
1048 concentration-gradient-driven proton conductance proposed here as faster proton
1049 release takes place driven by greater proton gradient. The proton barrier is breached in
1050 R82A mutant (Fig. 5). Therefore, the EC half channel must be filled with a continuous
1051 water network. Very little proton gradient can be established along the water filled
1052 channel during continuous pumping activity. R82A exhibits the same rate of proton
1053 uptake as the wildtype, but a rapid M formation without a pH dependency between
1054 neutral pH and pH10. Such rapid M formation is even faster than the wildtype under
1055 alkaline condition (Balashov et al., 1993). This is obviously due to the inability to
1056 establish the super-acidic inner EC channel without an intact proton barrier so that the
1057 protonation of Asp85 is accelerated compared to the wildtype. More interestingly, the
1058 fast phase of proton release is absent in R82A. Instead, a slow relaxation of 30 ms after
1059 proton uptake was observed (Balashov et al., 1993). Under the mechanism of a
1060 concentration-gradient-driven proton conductance, this slow relaxation is the
1061 spontaneous movement of the newly pumped proton in the same photocycle driven by
1062 a small gradient. Therefore, the “early release” in the fast phase of proton release
1063 cannot be observed without a well-established super-acidic inner EC channel in R82A.
1064 The “early release” observed from the wildtype is actually a much slower proton
1065 movement, in which a proton pumped into the super-acidic inner channel several
1066 photocycles ago is “squeezed out” by a newly pumped proton. This proton released
1067 from the wildtype appears to be coupled with or even faster than the protonation of
1068 Asp85.

1069
1070 Similar to R82A, another mutant R82Q also features rapid, biphasic formation of M
1071 at 1 and 160 μ s but delayed proton release after uptake at neutral pH (Govindjee et al.,
1072 1996). However, unlike R82A, proton release from R82Q shows its strong pH-
1073 dependency. At neutral pH, the majority of proton release occurs late at 23 ms. If the
1074 pH increases to 8, most proton release precedes proton uptake at a few ms. The amide
1075 group on the side chain of the neutral residue Gln82 could be protonated by
1076 hydroniums in the inner EC channel. However, the amide group is not a sufficient
1077 proton barrier with its pK_a of -1.4 that could only establish a proton puddle less acidic
1078 compared to that of the wildtype. Another important factor to a smaller proton puddle

1079 is that Gln is two bonds shorter than Arg. As a result, rapid proton release at a few ms
1080 is possible with a sufficient proton gradient under high pH. However, proton release is
1081 delayed to 23 ms as the proton gradient decreases under neutral pH. Again, the proton
1082 apparently released early is one of the protons accumulated in the inner EC channel, not
1083 the one freshly pumped in the same photocycle.

1084

1085 *Supplementary Q&A*

1086 This study addresses four key questions regarding the operating mechanisms of the
1087 light-driven proton pump bR in addition to the question of isomerization sampling
1088 (Ren, 2021). Answers to these questions are somewhat scattered in the main text while
1089 evidence are presented to support these answers. Here the answers are recapped
1090 without the interruption of the technical details of the supporting data.

1091

1092 Q1) How does the protonated SB with a pK_a of 13.3 transfer its proton to the acidic
1093 acceptors and when?

1094

1095 A1) Which of the two weak interactions $N_{\zeta}:H^+:O402$ survives an abrupt tare while the
1096 retinal prepares to undergo photoisomerization is determined by the inertia of the
1097 proton (Fig. 2c). It is decisive that the proton dissociates from the SB due to its inertia at
1098 the beginning of the retinal photoisomerization. The SB nitrogen makes a rapid U-turn
1099 at ~ 30 fs (Figs. 2a and S2). A force > 500 pN is required to accelerate the proton as fast
1100 as the SB. Breaking the H-bond $H_2O402:H^+$ is nearly as costly as breaking the
1101 association $N_{\zeta}:H^+$ (Figs. 1 inset and 2c). Therefore, the proton joins Wat402 to form a
1102 hydronium ion due to its inertia instead of keeping up to maintain the SB protonated.
1103 Such a proton transfer uphill over 15 pH units within tens of fs is not achieved by a
1104 chemical equilibrium, thus not governed by pK_a values. This proton transfer requires a
1105 high peak power dH/dt localized at the SB. On the other hand, holding Wat402 in place
1106 by both Asp85 and 212 symmetrically from inboard and outboard is as important as the
1107 ultrafast shaking of the SB. This proton transfer uses the same mechanism of the
1108 tablecloth trick. The early deprotonation from the SB is a separate event from the
1109 protonation of Asp85 ten decades later at the formation of M state. Vibrational
1110 signatures from the neutralization of the carboxylates previously observed do not imply
1111 SB deprotonation. This light-driven reaction of a proton pump differs markedly from a
1112 thermal driven chemical equilibrium (Fig. 2c).

1113

1114 Q2) Which molecular event, the isomerization, or another event, switches the
1115 accessibility of the SB from EC side to CP side and how does the SB avoid reprotonation
1116 on the wrong side?

1117

1118 A2) Immediately before isomerization in the I state, the SB is reoriented toward the
1119 inboard while Wat402, a hydronium at this moment, is displaced to the outboard. This
1120 geometry is very bad for proton exchange (Fig. S3). Therefore, the accessibility of the
1121 SB is already limited even before isomerization. However, accessibility switch of the SB
1122 is finally accomplished by the photoisomerization during $I \rightarrow J'$. The
1123 photoisomerization must be quick enough to prevent a chemical equilibrium in the EC
1124 half channel. If the equilibrium is reached before isomerization, the SB is reprotonated
1125 from the EC side, and the quantum yield of the proton pump is sacrificed (Govindjee et
1126 al., 1990).

1127

1128 Q3) How are protons conducted $> 15 \text{ \AA}$ through the rollercoasting pK_a values and
1129 released into the EC medium from the SB of a high pK_a through aspartic acids of low
1130 pK_a , arginine (strictly speaking, its guanidinium ion) and tyrosine of high pK_a , and
1131 glutamic acids of low pK_a again?

1132

1133 A3) The EC half channel is obviously not lined with residues of pK_a values in a
1134 monotonic order (Figs. 5 and S1). Despite numerous observations of pK_a changes, no
1135 sufficient evidence supports photoinduced changes to form an ascending order of pK_a
1136 values either. Proton is therefore not conducted along an ascending order of pK_a values
1137 driven by the proton affinity (Stoeckenius, 1999; Stoeckenius et al., 1979). Instead,
1138 proton conductance is driven by concentration gradient, not by affinity gradient. The
1139 guanidinium ion of the arginine and tyrosines of high pK_a , together with several main
1140 chain carbonyls, are arranged to function as a proton levee so that protons could only
1141 overflow outward from a super-acidic inner EC channel established after several
1142 successful cycles of proton pumping. No proton is released during the first a few cycles
1143 of productive pumping until a sufficient proton gradient is established. Under a super-
1144 acidic condition in the inner EC channel, the guanidinium group of Arg82 is protonated
1145 for a second time to form a divalent cation. While it swings outward, the extra proton is
1146 discharged to Glu194, 204, and a water cluster in the outer EC channel, the proton

1147 release complex. Protons could never flow backward into the cell as long as sufficient
1148 water is available in the EC medium. The rollercoasting pK_a values ensure the
1149 concentration-driven outward conductance of protons and prevent the concentration-
1150 driven inward conductance during dark, that is, a unidirectional valve.

1151
1152 Q4) How is a gradient-driven proton leak prevented in the resting state and during the
1153 pumping motions?

1154
1155 A4) A potential proton leak back into the cell during dark is prevented by the exact
1156 mechanism that conducts proton outward (A3). However, the chance of proton leak
1157 increases dramatically during the molecular motions of proton pumping because the
1158 inner EC channel becomes super acidic and the retinal and its surrounding are in
1159 constant motions. Lys216 forms a corner at C_ϵ that protrudes inboard and makes a van
1160 der Waals contact with Thr89 in helix C (Figs. 2b and S10a). Pressed by the corner at C_ϵ ,
1161 helix C is kinked and bends away. This contact is a seal between two half channels.
1162 This seal could be broken briefly in I' state but inconsequential. C_δ - C_ϵ moves outboard
1163 in L state once again due to a flattened 13-*cis* retinal (Figs. 2b and S10a). But this motion
1164 is slow enough to allow the spring-loaded helix C to react. Helix C straightens and
1165 maintains the contact between the chromophore and Thr89 to prevent a concentration-
1166 gradient-driven proton leak back into the CP (Figs. 3f and 4c). During the M states, the
1167 corner at C_ϵ is reestablished. It pushes Thr89 and helix C to restore its kink.

1168
1169 **Methods**

1170 From the outset, the key presumption is that every crystallographic dataset, at a given
1171 temperature and a given time delay after the triggering of the photochemical reaction,
1172 captures a mixture of unknown number of intermediate species at unknown fractions.
1173 Needless to say, all structures of the intermediates are also unknown except the
1174 structure at the ground state that has been determined and well refined by static
1175 crystallography. A simultaneous solution of all these unknowns requires multiple
1176 datasets that are collected at various temperatures or time delays so that a common set
1177 of intermediate structures are present in these datasets with variable ratios. If the
1178 number of available datasets is far greater than the number of unknowns, a linear
1179 system can be established to overdetermine the unknowns with the necessary
1180 stereochemical restraints (Ren et al., 2013). This analytical strategy is recapped below.

1181
1182 The methodological advance in this work and the companion work (Ren, 2021) is the
1183 refinement of each pure intermediate structure that has been deconvoluted from
1184 multiple mixtures. Structure factor amplitudes of a single conformation free of
1185 heterogeneity are overdetermined. Unlike the conventional crystallography, such a
1186 deconvoluted dataset of structure factor amplitudes are not observed directly from any
1187 crystal but computed from many experimental datasets. It could be considered as an
1188 extrapolated dataset “on steroids” if compared to the traditional extrapolation of small
1189 differences, such as, 3Fo-2Fc map, a technique often used to overcome a partial
1190 occupancy of an intermediate structure, except that this deconvolution method is an
1191 interpolation among many experimental datasets rather than an extrapolation. The
1192 standard structural refinement software is taken full advantage of with the built-in
1193 stereochemical constraints, e.g. PHENIX (Adams et al., 2010; Liebschner et al., 2019). In
1194 case that the computed deconvolution has not achieved a single pure structural species,
1195 the structural refinement is expected to make such indication.

1196
1197 *Difference Fourier maps*

1198 A difference Fourier map is synthesized from a Fourier coefficient set of $F_{\text{light}} - F_{\text{reference}}$
1199 with the best available phase set, often from the ground state structure. Before Fourier
1200 synthesis, F_{light} and $F_{\text{reference}}$ must be properly scaled to the same level so that the
1201 distribution of difference values is centered at zero and not skewed either way. A
1202 weighting scheme proven effective assumes that a greater amplitude of a difference
1203 Fourier coefficient $F_{\text{light}} - F_{\text{reference}}$ is more likely caused by noise than by signal (Ren et al.,
1204 2001, 2013; Šrajer et al., 2001; Ursby and Bourgeois, 1997). Both the dark and light
1205 datasets can serve as a reference in difference maps. If a light dataset at a certain delay
1206 is chosen as a reference, the difference map shows the changes since that delay time but
1207 not the changes prior to that delay. However, both the dark and light datasets must be
1208 collected in the same experiment. A cross reference from a different experimental
1209 setting usually causes large systematic errors in the difference map that would swamp
1210 the desired signals. Each difference map is masked 3.5 Å around the entire molecule of
1211 bacteriorhodopsin (bR). No lipid density is analyzed.

1212

1213 *Meta-analysis of protein structures*

1214 Structural meta-analysis based on singular value decomposition (SVD) has been
1215 conducted in two forms. In one of them, an interatomic distance matrix is calculated
1216 from each protein structure in a related collection. SVD of a data matrix consists of
1217 these distance matrices enables a large-scale joint structural comparison but requires no
1218 structural alignment (Ren, 2013a, 2013b, 2016). In the second form, SVD is performed
1219 on a data matrix of electron density maps of related protein structures (Ren, 2019; Ren
1220 et al., 2013; Schmidt et al., 2003, 2010). Both difference electron density maps that
1221 require a reference dataset from an isomorphous crystal and simulated annealing omit
1222 maps that do not require the same unit cell and space group of the crystals are possible
1223 choices in a structural meta-analysis (Ren, 2019; Ren et al., 2013). The distance matrices
1224 or the electron density maps that SVD is performed on are called core data. Each
1225 distance matrix or electron density map is associated with some metadata that describe
1226 the experimental conditions under which the core data are obtained, such as
1227 temperature, pH, light illumination, time delay, mutation, etc. These metadata do not
1228 enter the SVD procedure. However, they play important role in the subsequent
1229 interpretation of the SVD result. This computational method of structural analysis takes
1230 advantage of a mathematical, yet practical, definition of conformational space with
1231 limited dimensionality (Ren, 2013a). Each experimentally determined structure is a
1232 snapshot of the protein structure. A large number of such snapshots taken under a
1233 variety of experimental conditions, the metadata, would collectively provide a survey of
1234 the accessible conformational space of the protein structure and reveal its reaction
1235 trajectory. Such joint analytical strategy would not be effective in early years when far
1236 fewer protein structures were determined to atomic resolution. Recent rapid growth in
1237 protein crystallography, such as in structural genomics (Berman et al., 2012; Chandonia
1238 and Brenner, 2006) and in serial crystallography (Glynn and Rodriguez, 2019; Schaffer
1239 et al., 2021), has supplied the necessarily wide sampling of protein structures for a joint
1240 analytical strategy to come of age. The vacancies or gaps in a conformational space
1241 between well-populated conformational clusters often correspond to less stable
1242 transient states whose conformations are difficult to capture, if not impossible. These
1243 conformations are often key to mechanistic understanding and could be explored by a
1244 back calculation based on molecular distance geometry (Ren, 2013a, 2016), the chief
1245 computational algorithm in nucleic magnetic resonance spectroscopy (NMR), and by a
1246 structure refinement based on reconstituted dataset, a major methodological advance in

1247 this work (see below). These structures refined to atomic resolution against
1248 reconstituted datasets may reveal short-lived intermediate conformation hard to be
1249 captured experimentally. Unfortunately, a protein structure refined against a
1250 reconstituted dataset currently cannot be recognized by the Protein Data Bank (PDB).
1251 Because crystallographic refinement of a macromolecular structure is narrowly defined
1252 as a correspondence from one dataset to one structure. A never-observed dataset
1253 reconstituted from a collection of experimental datasets does not match the well-
1254 established crystallographic template of PDB; let alone a refinement of crystal structure
1255 with the NMR algorithm.

1256

1257 A distance matrix contains M pairwise interatomic distances of a structure in the
1258 form of Cartesian coordinates of all observed atoms. An everyday example of distance
1259 matrix is an intercity mileage chart appended to the road atlas. Differences in the
1260 molecular orientation, choice of origin, and crystal lattice among all experimentally
1261 determined structures have no contribution to the distance matrices. Due to its
1262 symmetry, only the lower triangle is necessary. A far more intimate examination of
1263 protein structures in PDB is a direct analysis of their electron density maps instead of
1264 the atomic coordinates. M such (difference) electron densities, often called voxels in
1265 computer graphics, are selected by a mask of interest. In the case of difference maps,
1266 only the best refined protein structure in the entire collection supplies a phase set for
1267 Fourier synthesis of electron density maps. This best structure is often the ground state
1268 structure determined by static crystallography. Other refined atomic coordinates from
1269 the PDB entries are not considered in the meta-analysis. That is to say, a meta-analysis
1270 of difference electron density maps starts from the X-ray diffraction data archived in
1271 PDB rather than the atomic coordinates interpreted from the diffraction data, which
1272 removes any potential model bias.

1273

1274 *Singular value decomposition of (difference) electron density maps*

1275 An electron density map, particularly a difference map as emphasized here, consists of
1276 density values on an array of grid points within a mask of interest. All M grid points in
1277 a three-dimensional map can be serialized into a one-dimensional sequence of density
1278 values according to a specific protocol. It is not important what the protocol is as long
1279 as a consistent protocol is used to serialize all maps of the same grid setting and size,
1280 and a reverse protocol is available to erect a three-dimensional map from a sequence of

1281 M densities. Therefore, a set of N serialized maps, also known as vectors in linear
1282 algebra, can fill the columns of a data matrix \mathbf{A} with no specific order, so that the width
1283 of \mathbf{A} is N columns, and the length is M rows. Often, $M \gg N$, thus \mathbf{A} is an elongated
1284 matrix. If a consistent protocol of serialization is used, the corresponding voxel in all N
1285 maps occupies a single row of matrix \mathbf{A} . This strict correspondence in a row of matrix
1286 \mathbf{A} is important. Changes of the density values in a row from one structure to another
1287 are due to either signals, systematic errors, or noises. Although the order of columns in
1288 matrix \mathbf{A} is unimportant, needless to say, the metadata associated with each column
1289 must remain in good bookkeeping.

1290

1291 SVD of the data matrix \mathbf{A} results in $\mathbf{A} = \mathbf{U}\mathbf{W}\mathbf{V}^T$, also known as matrix factorization.
1292 Matrix \mathbf{U} has the same shape as \mathbf{A} , that is, N columns and M rows. The N columns
1293 contain decomposed basis components \mathbf{U}_k , known as left singular vectors of M items,
1294 where $k = 1, 2, \dots, N$. Therefore, each component \mathbf{U}_k can be erected using the reverse
1295 protocol to form a three-dimensional map. This decomposed elemental map can be
1296 presented in the same way as the original maps, for example, rendered in molecular
1297 graphics software such as Coot and PyMol. It is worth noting that these decomposed
1298 elemental maps or map components \mathbf{U}_k are independent of any metadata. That is to
1299 say, these components remain constant when the metadata vary. Since each left
1300 singular vector \mathbf{U}_k has a unit length due to the orthonormal property of SVD (see
1301 below), that is, $|\mathbf{U}_k| = 1$, the root mean squares (rms) of the items in a left singular
1302 vector is $1/\sqrt{M}$ that measures the quadratic mean of the items.

1303

1304 The second matrix \mathbf{W} is a square matrix that contains all zeros except for N positive
1305 values on its major diagonal, known as singular values w_k . The magnitude of w_k is
1306 considered as a weight or significance of its corresponding component \mathbf{U}_k . The third
1307 matrix \mathbf{V} is also a square matrix of $N \times N$. Each column of \mathbf{V} or row of its transpose \mathbf{V}^T ,
1308 known as a right singular vector \mathbf{V}_k , contains the relative compositions of \mathbf{U}_k in each of
1309 the N original maps. Therefore, each right singular vector \mathbf{V}_k can be considered as a
1310 function of the metadata. Right singular vectors also have the same unit length, that is,
1311 $|\mathbf{V}_k| = 1$. Effectively, SVD separates the constant components independent of the
1312 metadata from the compositions that depend on the metadata.

1313

1314 A singular triplet denotes 1) a decomposed component \mathbf{U}_k , 2) its singular value w_k ,
 1315 and 3) the composition function \mathbf{V}_k . Singular triplets are often sorted in a descending
 1316 order of their singular values w_k . Only a small number of n significant singular triplets
 1317 identified by the greatest singular values w_1 through w_n can be used in a linear
 1318 combination to reconstitute a set of composite maps that closely resemble the original
 1319 ones in matrix \mathbf{A} , where $n < N$. For example, the original map in the i th column of
 1320 matrix \mathbf{A} under a certain experimental condition can be closely represented by the i th
 1321 composite map $w_1 v_{1i} \mathbf{U}_1 + w_2 v_{2i} \mathbf{U}_2 + \dots + w_n v_{ni} \mathbf{U}_n$, where (v_{1i}, v_{2i}, \dots) is from the i th row of
 1322 matrix \mathbf{V} . The coefficient set for the linear combination is redefined here as $c_{ki} =$
 1323 $w_k v_{ki} / \sqrt{M}$. The rms of the values in a map component, or the average magnitude
 1324 measured by the quadratic mean, acts as a constant scale factor that resets the modified
 1325 coefficients c_{ki} back to the original scale of the core data, such as \AA for distance matrices
 1326 and $e/\text{\AA}^3$ for electron density maps if these units are used in the original matrix \mathbf{A} .
 1327 Practically, an electron density value usually carries an arbitrary unit without a
 1328 calibration, which makes this scale factor unnecessary. In the linear combination $c_{1i} \mathbf{U}_1 +$
 1329 $c_{2i} \mathbf{U}_2 + \dots + c_{ni} \mathbf{U}_n$, each component \mathbf{U}_k is independent of the metadata while how much of
 1330 each component is required for the approximation, that is, c_{ki} , depends on the metadata.

1331
 1332 Excluding the components after \mathbf{U}_n in this approximation is based on an assumption
 1333 that the singular values after w_n are very small relative to those from w_1 through w_n . As
 1334 a result, the structural information evenly distributed in all N original maps is
 1335 effectively concentrated into a far fewer number of n significant components, known as
 1336 information concentration or dimension reduction. On the other hand, the trailing
 1337 components in matrix \mathbf{U} contain inconsistent fluctuations and random noises.
 1338 Excluding these components effectively rejects noises (Schmidt et al., 2003). The least-
 1339 squares property of SVD guarantees that the rejected trailing components sums up to
 1340 the least squares of the discrepancies between the original core data and the
 1341 approximation using the accepted components.

1342
 1343 However, no clear boundary is guaranteed between signals, systematic errors, and
 1344 noises. Systematic errors could be more significant than the desired signals. Therefore,
 1345 excluding some components from 1 through n is also possible. If systematic errors are
 1346 correctly identified, the reconstituted map without these significant components would
 1347 no longer carry the systematic errors.

1348

1349 *The orthonormal property of SVD*

1350 The solution set of SVD must guarantee that the columns in \mathbf{U} and \mathbf{V} , the left and right
1351 singular vectors \mathbf{U}_k and \mathbf{V}_k , are orthonormal, that is, $\mathbf{U}_h \bullet \mathbf{U}_k = \mathbf{V}_h \bullet \mathbf{V}_k = 0$ (ortho) and $\mathbf{U}_k \bullet \mathbf{U}_k$
1352 $= \mathbf{V}_k \bullet \mathbf{V}_k = 1$ (normal), where $h \neq k$ but both are from 1 to N . The orthonormal property
1353 also holds for the row vectors. As a result, each component \mathbf{U}_k is independent of the
1354 other components. In other words, a component cannot be represented by a linear
1355 combination of any other components. However, two physical or chemical parameters
1356 in the metadata, such as temperature and pH, may cause different changes to a
1357 structure. These changes are not necessarily orthogonal. They could exhibit some
1358 correlation. Therefore, the decomposed components \mathbf{U}_k not necessarily represent any
1359 physically or chemically meaningful changes (see below).

1360

1361 Due to the orthonormal property of SVD, an N -dimensional Euclidean space is
1362 established, and the first n dimensions define its most significant subspace. Each
1363 coefficient set $\mathbf{c}_i = (c_{1i}, c_{2i}, \dots, c_{ni})$ of the i th composite map is located in this n -dimensional
1364 subspace. All coefficient sets for $i = 1, 2, \dots, N$ in different linear combinations to
1365 approximate the N original maps in a least-squares sense can be represented by N
1366 points or vectors $\mathbf{c}_1, \mathbf{c}_2, \dots, \mathbf{c}_N$ in the Euclidean subspace. This n -dimensional subspace is
1367 essentially the conformational space as surveyed by the jointly analyzed core data. The
1368 conformational space is presented as scatter plots with each captured structure
1369 represented as a dot located at a position determined by the coefficient set \mathbf{c}_i of the i th
1370 observed map. When the subspace has greater dimensionality than two, multiple two-
1371 dimensional orthographical projections of the subspace are presented. These scatter
1372 plots are highly informative to reveal the relationship between the (difference) electron
1373 density maps and their metadata.

1374

1375 If two coefficient sets $\mathbf{c}_i \approx \mathbf{c}_j$, they are located close to each other in the
1376 conformational space. Therefore, these two structures i and j share two similar
1377 conformations. Two structures located far apart from each other in the conformational
1378 space are distinct in their conformations, and distinct in the compositions of the map
1379 components. A reaction trajectory emerges in this conformational space if the temporal
1380 order of the core data is experimentally determined (Figs. S4 and S7). Otherwise, an
1381 order could be assigned to these structures based on an assumed smoothness of

1382 conformational changes along a reaction trajectory (Ren, 2013a, 2013b, 2016). Causation
1383 and consequence of structural motions could be revealed from the order of the
1384 structures in a series, which may further lead to structural mechanism. In addition, an
1385 off-trajectory location in the conformational space or a location between two clusters of
1386 observed structures represents a structure in a unique conformation that has never been
1387 experimentally captured. Such a hypothetical structure can be refined against a
1388 reconstituted distance matrix using molecular distance geometry (Ren, 2013a, 2013b,
1389 2016) or a reconstituted electron density map with the method proposed below.

1390

1391 *Rotation in SVD space*

1392 Dimension reduction is indeed effective in meta-analysis of protein structures when
1393 many datasets are evaluated at the same time. However, the default solution set of SVD
1394 carries complicated physical and chemical meanings that are not immediately obvious.
1395 The interpretation of a basis component \mathbf{U}_k , that is, “what-does-it-mean”, requires a
1396 clear demonstration of the relationship between the core data and their metadata. The
1397 outcome of SVD does not guarantee any physical meaning in a basis component.
1398 Therefore, SVD alone provides no direct answer to “what-does-it-mean”, thus its
1399 usefulness is very limited to merely a mathematical construction. However, the
1400 factorized set of matrices \mathbf{U} , \mathbf{W} , and \mathbf{V} from SVD is not a unique solution. That is to say,
1401 they are not the only solution to factorize matrix \mathbf{A} . Therefore, it is very important to
1402 find one or more alternative solution sets that are physically meaningful to elucidate a
1403 structural interpretation. The concept of a rotation after SVD was introduced by Henry
1404 & Hofrichter (Henry and Hofrichter, 1992). But they suggested a protocol that fails to
1405 preserve the orthonormal and least-squares properties of SVD. The rotation protocol
1406 suggested by Ren incorporates the metadata into the analysis and combines with SVD
1407 of the core data. This rotation achieves a numerical deconvolution of multiple physical
1408 and chemical factors after a pure mathematical decomposition, and therefore, provides
1409 a route to answer the question of “what-does-it-mean” (Ren, 2019). This rotation shall
1410 not be confused with a rotation in the three-dimensional real space, in which a
1411 molecular structure resides.

1412

1413 A rotation in the n -dimensional Euclidean subspace is necessary to change the
1414 perspective before a clear relationship emerges to elucidate scientific findings. It is
1415 shown below that two linear combinations are identical before and after a rotation

1416 applied to both the basis components and their coefficients in a two-dimensional
1417 subspace of h and k . That is,

1418

$$c_h \mathbf{U}_h + c_k \mathbf{U}_k = f_h \mathbf{R}_h + f_k \mathbf{R}_k, \quad (1)$$

1419

1420 where c_h and c_k are the coefficients of the basis components \mathbf{U}_h and \mathbf{U}_k before the
1421 rotation; and f_h and f_k are the coefficients of the rotated basis components \mathbf{R}_h and \mathbf{R}_k ,
1422 respectively. The same Givens rotation of an angle θ is applied to both the components
1423 and their coefficients:

1424

$$\begin{cases} \mathbf{R}_h = \mathbf{U}_h \cos \theta - \mathbf{U}_k \sin \theta; \\ \mathbf{R}_k = \mathbf{U}_h \sin \theta + \mathbf{U}_k \cos \theta. \end{cases} \quad (2)$$

1425

1426 Obviously, the rotated components \mathbf{R}_h and \mathbf{R}_k remain mutually orthonormal and
1427 orthonormal to other components. And

1428

$$\begin{cases} f_h = s_h t_h = c_h \cos \theta - c_k \sin \theta; \\ f_k = s_k t_k = c_h \sin \theta + c_k \cos \theta. \end{cases} \quad (3)$$

1429

1430 Here $s_{h|k} = \sqrt{\sum f_{h|k}^2}$ are the singular values that replace w_h and w_k , respectively, after the
1431 rotation. They may increase or decrease compared to the original singular values so
1432 that the descending order of the singular values no longer holds. $\mathbf{T}_{h|k} = (t_{h|k1}, t_{h|k2}, \dots,$
1433 $t_{h|kN}) = (f_{h|k1}, f_{h|k2}, \dots, f_{h|kN})/s_{h|k}$ are the right singular vectors that replace \mathbf{V}_h and \mathbf{V}_k ,
1434 respectively. \mathbf{T}_h and \mathbf{T}_k remain mutually orthonormal after the rotation and
1435 orthonormal to other right singular vectors that are not involved in the rotation.

1436

1437 Eq. 1 holds because the dot product of two vectors does not change after both
1438 vectors rotate the same angle. To prove Eq. 1 in more detail, Eqs. 2 and 3 are combined
1439 and expanded. All cross terms of sine and cosine are self-canceled:

1440

$$\begin{aligned} 1441 \quad f_h \mathbf{R}_h + f_k \mathbf{R}_k &= (c_h \cos \theta - c_k \sin \theta)(\mathbf{U}_h \cos \theta - \mathbf{U}_k \sin \theta) + (c_h \sin \theta + c_k \cos \theta)(\mathbf{U}_h \sin \theta + \mathbf{U}_k \cos \theta) \\ 1442 &= c_h \mathbf{U}_h \cos^2 \theta + c_k \mathbf{U}_k \sin^2 \theta + c_h \mathbf{U}_h \sin^2 \theta + c_k \mathbf{U}_k \cos^2 \theta \pm c_h \mathbf{U}_k \sin \theta \cos \theta \pm c_k \mathbf{U}_h \sin \theta \cos \theta \\ 1443 &= c_h \mathbf{U}_h (\cos^2 \theta + \sin^2 \theta) + c_k \mathbf{U}_k (\sin^2 \theta + \cos^2 \theta) \\ 1444 &= c_h \mathbf{U}_h + c_k \mathbf{U}_k \end{aligned}$$

1445

1446 A rotation in two-dimensional subspace of h and k has no effect in other dimensions,
1447 as the orthonormal property of SVD guarantees. Multiple steps of rotations can be
1448 carried out in many two-dimensional subspaces consecutively to achieve a multi-
1449 dimensional rotation. A new solution set derived from a rotation retains the
1450 orthonormal property of SVD. The rotation in the Euclidean subspace established by
1451 SVD does not change the comparison among the core data of protein structures. Rather
1452 it converts one solution set $\mathbf{A} = \mathbf{U}\mathbf{W}\mathbf{V}^T$ to other alternative solutions $\mathbf{A} = \mathbf{R}\mathbf{S}\mathbf{T}^T$ so that
1453 an appropriate perspective can be found to elucidate the relationship between the core
1454 data and metadata clearly and concisely.

1455
1456 For example, if one physical parameter could be reoriented along a single dimension
1457 k but not involving other dimensions by a rotation, it would be convincing to show that
1458 the left singular vector \mathbf{U}_k of this dimension illustrates the structural impact by this
1459 physical parameter. Before this rotation, the same physical parameter may appear to
1460 cause structural variations along several dimensions, which leads to a difficult
1461 interpretation. Would a proper rotation establish a one-on-one correspondence from all
1462 physical or chemical parameters to all the dimensions? It depends on whether each
1463 parameter induces an orthogonal structural change, that is, whether structural
1464 responses to different parameters are independent or correlated among one another. If
1465 structural changes are indeed orthogonal, it should be possible to find a proper rotation
1466 to cleanly separate them in different dimensions. Otherwise, two different rotations are
1467 necessary to isolate two correlated responses, but one at a time.

1468
1469 For another example, if the observed core datasets form two clusters in the
1470 conformational space, a rotation would be desirable to separate these clusters along a
1471 single dimension k but to align these clusters along other dimensions. Therefore, the
1472 component \mathbf{U}_k is clearly due to the structural transition from one cluster to the other.
1473 Without a proper rotation, the difference between these clusters could be complicated
1474 with multiple dimensions involved. A deterministic solution depends on whether a
1475 clear correlation exists between the core data and metadata. A proper rotation may
1476 require a user decision. A wrong choice of rotation may select a viewpoint that hinders
1477 a concise conclusion. However, it would not alter the shape of the reaction trajectory,
1478 nor create or eliminate an intrinsic structural feature. A wrong choice of rotation cannot
1479 eliminate the fact that a large gap exists between two clusters of observed core datasets

1480 except that these clusters are not obvious from that viewpoint. A different rotation may
 1481 reorient the perspective along another direction. But the structural conclusion would be
 1482 equivalent. See example of before and after a rotation in (Ren, 2016).

1483
 1484 This rotation procedure finally connects the core crystallographic datasets to the
 1485 metadata of experimental conditions and accomplishes the deconvolution of physical or
 1486 chemical factors that are not always orthogonal to one another after a mathematical
 1487 decomposition. SVD analysis presented in this paper employs rotations extensively
 1488 except that no distinction is made in the symbols of components and coefficients before
 1489 and after a rotation except in this section. This method is widely applicable in large-
 1490 scale structural comparisons. Furthermore, Ren rotation after SVD is not limited to
 1491 crystallography and may impact other fields wherever SVD is used. For example, SVD
 1492 is frequently applied to spectroscopic data, images, and genetic sequence data.

1493
 1494 A preliminary analysis of SVD involving all difference maps (Table S1) shows that
 1495 the short and long delays are in two different subspaces (Fig. S15). That is to say,
 1496 difference maps in the time regimes before 10 ps and after 10 ns share no common
 1497 features. This conclusion cannot be reached without a proper rotation of the
 1498 components. The separation between the short and long delays into different subspaces
 1499 can only be viewed clearly from this specific perspective shown in Fig. S15. Therefore,
 1500 these time regimes are analyzed separately.

1501
 1502 *Exponential fitting of SVD coefficients*

1503 The time dependencies of the SVD coefficients $c_1(t)$, $c_3(t)$, and $c_6(t)$ for the long delays $>$
 1504 10 ns are modeled with exponential functions (Fig. S7). Each time-dependent coefficient
 1505

$$c_k(t) = b_k + p_k \exp\left(-\frac{t}{\tau_1}\right) + q_k \exp\left(-\frac{t}{\tau_3}\right) + r_k \exp\left(-\frac{t}{\tau_6}\right) \quad (4)$$

1506
 1507 where $k = 1, 3, \text{ or } 6$. The time constant τ_k associated with the major change in each
 1508 coefficient models each step in the reaction scheme $K \rightarrow L \rightarrow M_1 \rightarrow M_2$. Whether the
 1509 time-dependent coefficients can be successfully fitted with exponentials is also a good
 1510 test for a proper rotation. Because the fact that the fractional concentrations of
 1511 intermediate species can be expressed as exponentials indicate that the reaction follows
 1512 a regular kinetic scheme.

1513
1514 *Structural refinement against reconstituted dataset*
1515 The linear combination $\Delta\rho(t) = f_1(t)\mathbf{R}_1 + f_2(t)\mathbf{R}_2 + \dots + f_n(t)\mathbf{R}_n$ after a rotation reconstitutes
1516 one of the observed difference maps at a specific time point t . This time-dependent
1517 difference map depicts an ever-evolving mixture of many excited species. A
1518 reconstituted difference map $\Delta\rho(E)$ for a time-independent, pure, excited species $E =$
1519 intermediate I' , I , J' , and J deconvoluted from many mixtures would take the same form
1520 except that only one or very few coefficients remain nonzero if a proper rotation has
1521 been found (Table S2). In order to take advantage of the mature refinement software for
1522 macromolecular structures with extensive stereochemical restraints, a set of structure
1523 factor amplitudes is needed. Therefore, it is necessary to reconstitute a set of structure
1524 factor amplitudes that would produce the target difference map $\Delta\rho(E)$ based on a
1525 known structure at the ground state. First, an electron density map of the structure at
1526 the ground state is calculated. This calculated map is used as a base map. Second, this
1527 base map of the ground state is combined with the positive and negative densities in the
1528 target difference map $\Delta\rho(E)$ so that the electron densities at the ground state are skewed
1529 toward the intermediate state. Third, structure factors are calculated from the
1530 combined map. Finally, the phase set of the calculated structure factors is discarded,
1531 and the amplitudes are used to refine a single conformation of the intermediate species
1532 E that $\Delta\rho(E)$ represents.

1533
1534 This protocol following the SVD and Ren rotation of components achieves a
1535 refinement of a pure structural species without the need of alternative conformations.
1536 Several points are noteworthy. First, the minimization protocol in this refinement is
1537 performed against a numerically reconstituted amplitude set that has never been
1538 directly measured from a crystal. This reconstituted dataset could be considered as an
1539 extrapolated dataset "on steroids" if compared to the traditional extrapolation of small
1540 differences, such as, the Fourier coefficient set to calculate a 3Fo-2Fc map, a technique
1541 often used to overcome a partial occupancy of an intermediate structure. An
1542 extrapolation of small differences is not directly observed either but computed by an
1543 exaggeration of the observed difference based on an assumption that the intermediate
1544 state is partially occupied, such as the doubling of the observed difference in 3Fo-2Fc =
1545 $F_o + 2(F_o - F_c)$. In contrast to the conventional technique of extrapolation, the
1546 deconvolution method applied here is an interpolation among many experimental

1547 datasets rather than an extrapolation. Secondly, the deconvolution is a simultaneous
1548 solution of multiple intermediate states mixed together instead of solving a single
1549 excited state.

1550
1551 Second, a map calculated from the ground state structure is chosen as the base map
1552 instead of an experimental map such as F_o or $2F_o-F_c$ map. If the second step of the
1553 protocol is skipped, that is, no difference map is combined with the ground state map,
1554 the refinement would result in an R factor of nearly zero, since the refinement is
1555 essentially against the calculated structure factors (bR in Table S2). This is to say, the
1556 residuals of the refinement are solely due to the difference component instead of the
1557 base map. This is desirable since errors in the static structure of the ground state are
1558 gauged during its own refinement. On the other hand, if an experimental map is
1559 chosen as a base map, the refinement R factors would reflect errors in both the base map
1560 and the difference map, which leads to a difficulty in an objective evaluation of this
1561 refinement protocol.

1562
1563 Third, the combination of the base map and a difference map is intended to
1564 represent a pure intermediate species. Therefore, alternative conformations in
1565 structural refinement that model a mixture of species would defeat this purpose.
1566 However, this combined map could be very noisy and may not represent a single
1567 species without a proper rotation. This is particular the case, if the target difference
1568 map $\Delta\rho$ is not derived from an SVD analysis and Ren rotation. The SVD analysis
1569 identifies many density components that are inconsistent among all observed difference
1570 maps and excludes them, which greatly reduces the noise content. Therefore, this
1571 refinement protocol may not be very successful without an SVD analysis. Another
1572 source of noise originates from the phase set of the structure factors. Prior to the
1573 refinement of the intermediate structure, the phase set remains identical to that of the
1574 ground state. This is far from the reality when an intermediate structure involves
1575 widespread changes, such as those refined in this study. If the rotation after SVD is not
1576 properly selected, the target difference map would remain as a mixture minus the
1577 ground state. Therefore, the refinement of a single conformation would encounter
1578 difficulty or significant residuals, as judged by the R factors, the residual map, and the
1579 refined structure. A proper solution to this problem is a better SVD solution by Ren
1580 rotation rather than alternative conformations. A successful refinement of near perfect

1581 *trans* or *cis* double bonds is a good sign to indicate that the reconstituted amplitude set
1582 after a rotation reflects a relatively homogeneous structure. If a double bond could not
1583 be refined well to near perfect *trans* or *cis* configuration, the dataset of structure factor
1584 amplitudes is likely from a mixture of heterogeneous configurations, which occurred
1585 frequently in previous studies of bR and photoactive yellow protein (Jung et al., 2013;
1586 Lanyi and Schobert, 2007; Nogly et al., 2018). It has been a great difficulty in
1587 crystallographic refinement in general that a heterogeneous mixture of conformations
1588 cannot be unambiguously refined even with alternative conformations. This difficulty
1589 becomes more severe when a mixture involves more than two conformations or when
1590 some conformations are very minor.

1591
1592 Lastly, the refinement protocol proposed here could be carried out in the original
1593 unit cell and space group of the crystal at the ground state. However, this is not always
1594 applicable as the original goal of the meta-analysis is a joint examination of all available
1595 structures from a variety of crystal forms. It would be highly desirable to evaluate
1596 difference maps of the same or similar proteins from non-isomorphous crystals together
1597 by SVD. Alternatively, the refinement protocol could also be performed in the space
1598 group of P1 with a virtual unit cell large enough to hold the structure, which is the
1599 option in this study (Table S2). This is to say, the entire analysis of SVD-rotation-
1600 refinement presented here could be extracted and isolated from the original crystal
1601 lattices, which paves the way to future applications to structural data acquired by
1602 experimental techniques beyond crystallography, most attractively, to single particle
1603 reconstruction in cryo electron microscopy.

1604

1605

1606 **Supplementary Tables**

1607

Table S1. Datasets analyzed in this work

Publication	PDB	Label	Resolution	Main conclusions	New findings in this work
Nango et al. Science 354, 1552, 2016	5b6v	dark5	1.77 Å	A newly ordered water on the CP side bridges the SB to Thr89 after isomerization, thus further conducts a proton to Asp85.	These datasets contribute to the overdetermination of the structures $K \rightarrow L \rightarrow M_1 \rightarrow M_2$. The early creased retinal is flattened; C ₂₀ methyl group returns into the original plane of the resting retinal as K transitions to L. The most flattened chromophore is achieved in L. The EC half channel contracts in L while the CP half channel starts to open. Reprotonation of the SB starts in L. Several ordered waters are observed in the enlarged CP half channel in M ₁ . The SB move toward inboard in M ₁ and M ₂ .
	5b6w	16ns	2.0 Å		
	5h2h	40ns	2.0 Å		
	5h2i	110ns	2.0 Å		
	5h2j	290ns	2.0 Å		
	5b6x	760ns	2.0 Å		
	5h2k	2μs	2.0 Å		
	5h2l	5.25μs	2.0 Å		
	5h2m	13.8μs	2.0 Å		
	5b6y	36.2μs	2.0 Å		
	5h2n	95.2μs	2.0 Å		
	5h2o	250μs	2.0 Å		
5h2p	657μs	2.0 Å			
5b6z	1.725ms	2.0 Å			
Nogly et al. Science 361, eaat0094, 2018	6g7h	dark6	1.5 Å	Retinal fully isomerizes at 10 ps. But the SB water dissociates earlier.	The short-delay datasets contribute to the structures of $I' \rightarrow I \rightarrow J' \rightarrow J$. Photoisomerization in J'; retinal binding pocket expansion before 1 ps in I and contraction at 10 ps in J
	6g7i	49-406fs	1.9 Å		
	6g7j	457-646fs	1.9 Å		
	6g7k	10ps	1.9 Å		
	6g7l	8.33ms	1.9 Å		
Kovacs et al. Nat. Commun. 10, 3177, 2019	6ga1	dark1	1.7 Å	The exceedingly high power density of the pump laser causes two-photon absorption. Vibrational motions were observed.	The sub-ps datasets exhibit extensive vibrations at various frequencies. The vibrational signals are widespread over the entire bR molecule and not associated with any structural elements. Therefore, it is concluded that these global vibrations are intrinsic properties of bR induced by short laser pulses. The vibrational signals are more prominent under higher power density of the laser pulses. However, these vibrations are irrelevant to the light-driven proton pumping function of bR.
	6ga2	dark2	1.8 Å		
	6rmk	dark3	1.8 Å		
	6ga7	240fs	1.8 Å		
	6ga8	330fs	1.8 Å		
	6ga9	390fs	1.8 Å		
	6gaa	430fs	1.8 Å		
	6gab	460fs	1.8 Å		
	6gac	490fs	1.8 Å		
	6gad	530fs	1.8 Å		
	6gae	560fs	1.8 Å		
	6gaf	590fs	1.8 Å		
	6gag	630fs	1.8 Å		
	6gah	680fs	1.8 Å		
	6gai	740fs	1.8 Å		
6ga4	1ps	1.8 Å			
6ga5	3ps	1.9 Å			
6ga6	10ps	1.8 Å			
6ga3	33ms	2.1 Å			
Weinert et al. Science 365, 61, 2019	6rqp	dark	1.8 Å	Helices E and F swing outward after 10 ms.	These datasets contribute to the overdetermination of M ₂ , in which an open CP half channel is observed. The SB moves toward inboard.
	6rnj	0-5ms	2.6 Å		
	6rph	10-15ms	2.6 Å		
	6rqo	activated	2.0 Å		

1608

Table S2. Refinement statistics

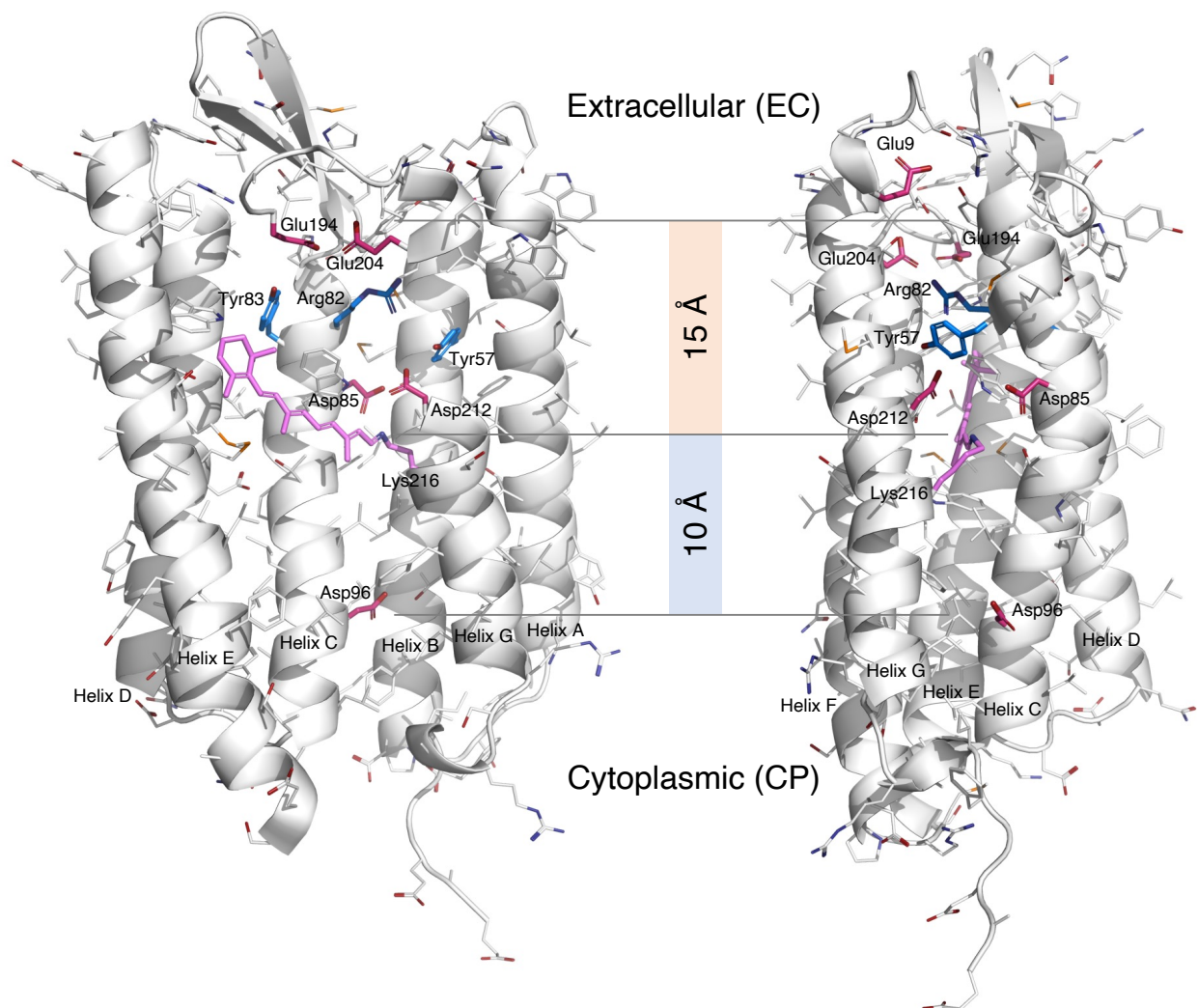
Intermediate Time period	bR	I'	I	J'	J	K	L	M ₁	M ₂
	0-	< 50 fs	40-700 fs	0.5-2 ps	1-30 ps	3 ps-2 μs	1-100 μs	10-1000 μs	0.5-5 ms
Short delay components	U₁₀		3,300		-4,200				
	U₁₄	2,000	2,700	2,700	2,000				
	U₁₇	3,000		-1,300	-300				
Long delay components	U₁					-700		2,200	1,000
	U₂					1,800	1,800	1,800	1,200
	U₃					-1,000	2,100	1,500	900
	U₆						-600		1,500
Starting model	PDB 6g7h								
Resolution range	50-2.1 Å								
Space group	P1								
Unit cell	$a = 62.32 \text{ \AA}; b = 62.32 \text{ \AA}; c = 111.10 \text{ \AA}; \alpha = 90^\circ; \beta = 90^\circ; \text{ and } \gamma = 120^\circ$								
Unique reflections	80,354 in working set + 4,236 in test set = 84,590 total								
Completeness	95% in working set + 5% in test set = 100% reconstituted								
R (%)	1.8	29.4	31.0	29.1	30.0	26.0	27.7	28.4	28.5
R _{free} (%)	1.9	31.1	32.4	30.4	30.7	26.3	28.8	29.6	29.7
Refined content	230 protein residues + 1 retinal + water molecules								
Number of atoms	1,798	1,795	1,798	1,796	1,795	1,798	1,794	1,799	1,796
Water molecules	8	5	8	6	5	8	4	9	6
RMSD bonds (Å)	0.005	0.009	0.009	0.009	0.009	0.009	0.009	0.009	0.009
RMSD angles (°)	0.793	1.206	1.105	1.085	1.068	1.006	1.074	1.120	1.081
Rama. favored (%)	98.7	96.5	95.6	96.1	96.5	97.8	96.5	97.4	96.1
Rama. outliers (%)	0.0	0.0	0.4	0.4	0.4	0.4	0.0	0.0	0.4
Clash score	4	9	5	4	6	6	7	10	7

1609

1610

1611 **Supplementary Figures and Legends**

1612

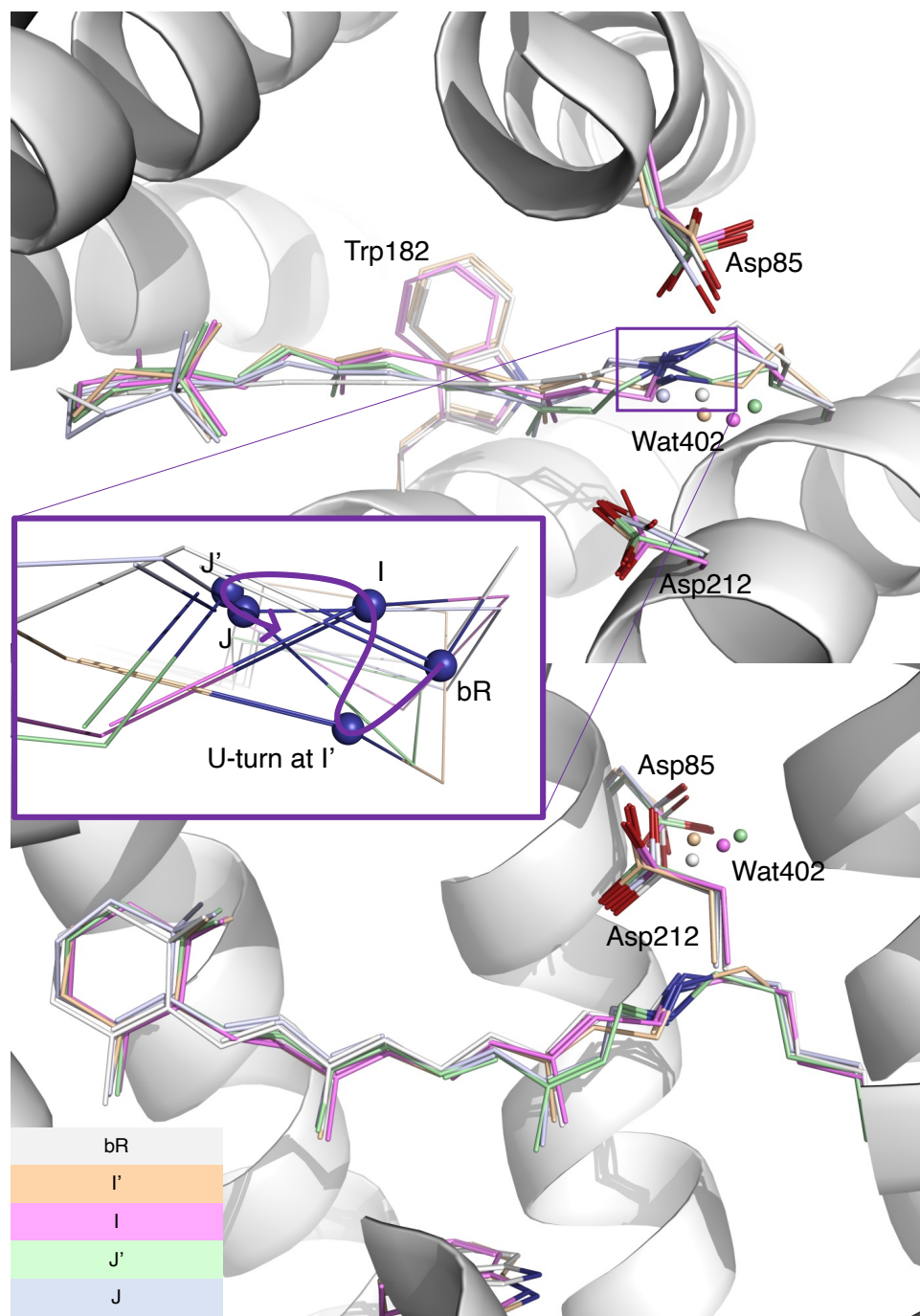


1613

1614

1615 Figure S1. Orthographical views of EC and CP half channels. Parts of the structure are
 1616 omitted to reveal the interior. The acidic residues in the half channels are highlighted in
 1617 red. Those in the EC half channel are deprotonated. Asp96 in the hydrophobic CP half
 1618 channel could be protonated (Gerwert et al., 1989). Arg82 in blue is protonated at
 1619 neutral pH to form a positive charged guanidinium ion with a pK_a of 12.5. Tyr57 and 83
 1620 with a pK_a of 10 in blue could be deprotonated at alkaline pH.

1621



1622

1623

1624 Figure S2. Two orthographical views of early intermediates. The refined conformations

1625 of the retinal and several key side chains are rendered in stick models of various colors.

1626 These early intermediates are compared with the resting state in white ribbon and stick

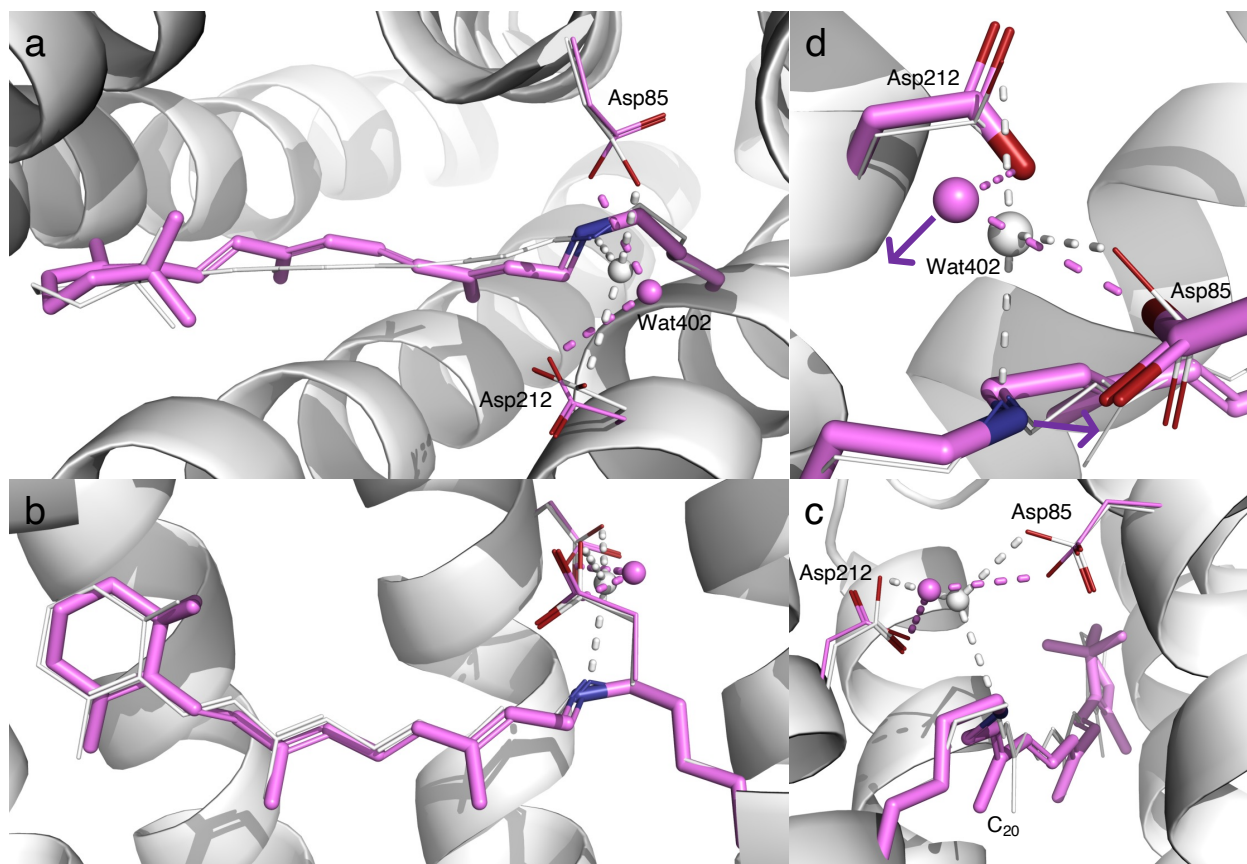
1627 model. Wat402 is rendered in small spheres. A zoom-in view of the SB is presented in

1628 the inset. N_{ζ} is shown in blue spheres. Its trajectory marked by a spline curve shows a

1629 sharp U-turn at I' state. The SB moves toward the distal direction during I and J due to
1630 a creased retinal (Fig. 2b).

1631

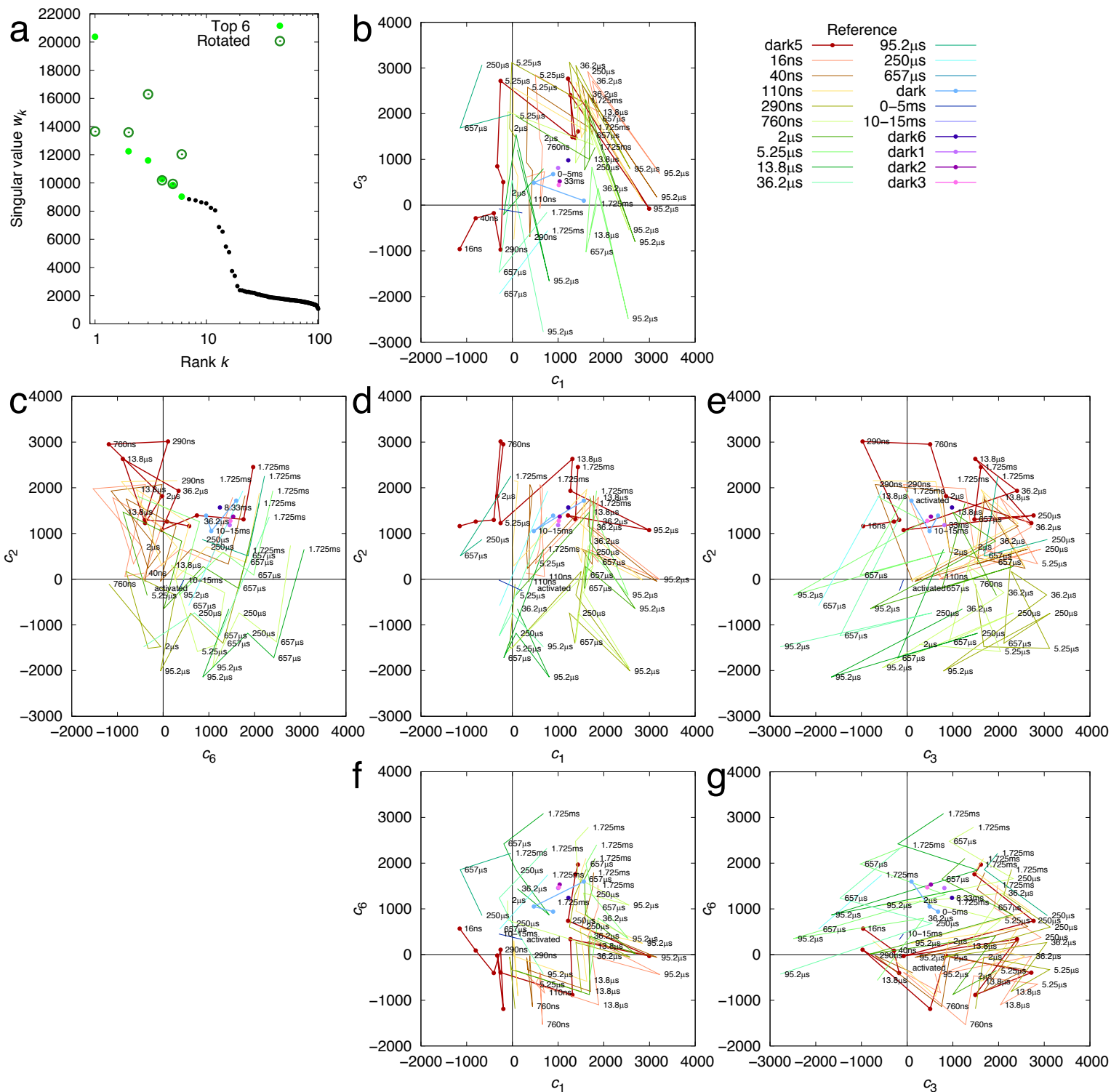
1632



1633
1634

1635 Figure S3. Refined structure of I state. (a, b, and c) Three orthographical views of
1636 retinal in I state. The refined retinal conformation in purple is compared with the
1637 resting state in white. The SB is pointing toward inboard with a perfect *syn*
1638 conformation at the single bond $N_{\zeta}-C_{\epsilon}$. C_{20} methyl group remains tilted toward
1639 outboard. Wat402 with good electron density is displaced toward outboard and
1640 remains H-bonded with both Asp85 and 212. (d) Zoom-in view of SB and Wat402.
1641 Wat402 is 3.7 Å away from the SB N_{ζ} . The would-be H-bond directions of the SB and
1642 Wat402 are pointing toward the opposite directions as marked by the arrows. This
1643 geometry makes not only a H-bond impossible but also any proton transfer difficult.
1644

Ren: Concentration-driven proton conductance

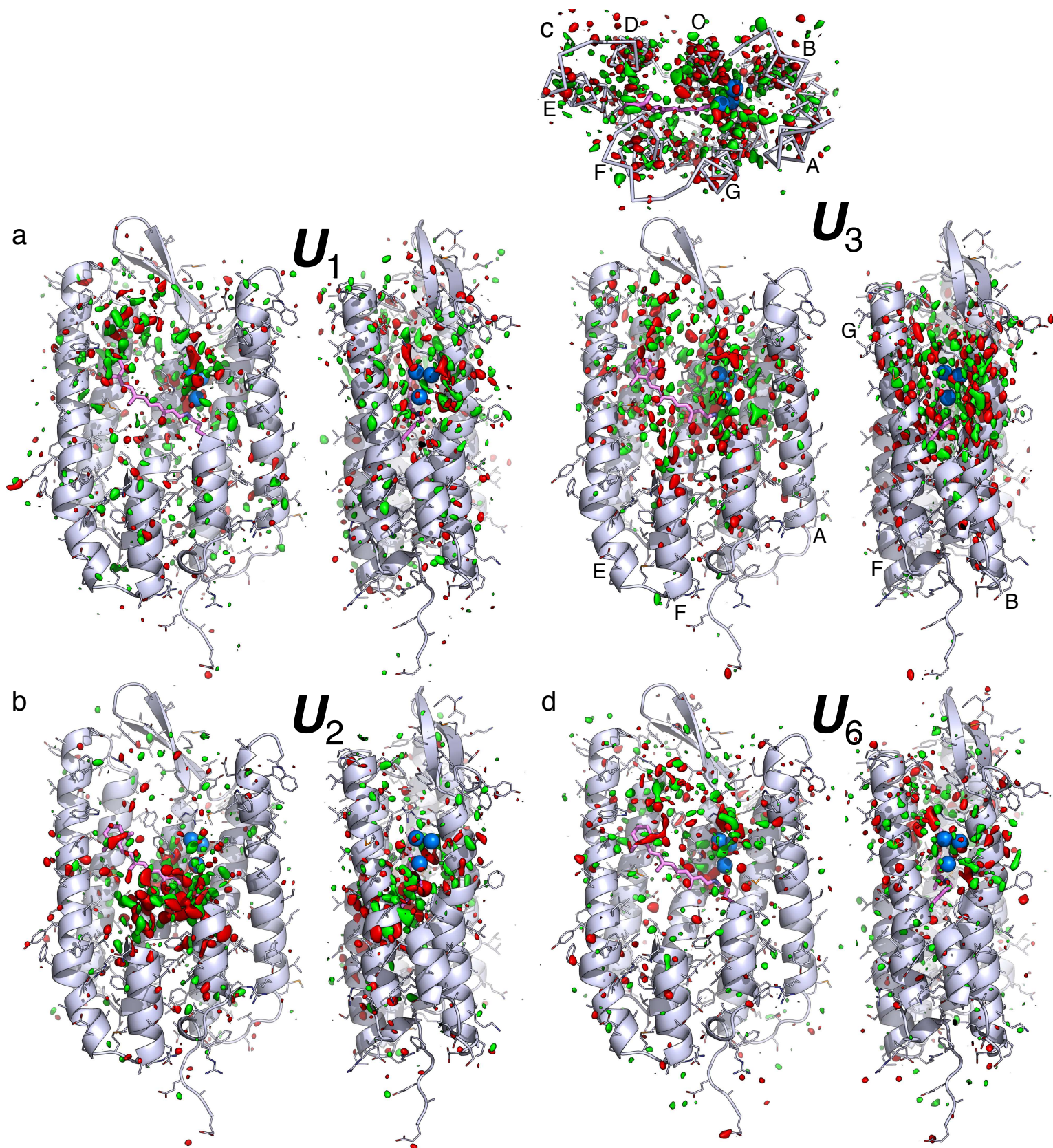


1646

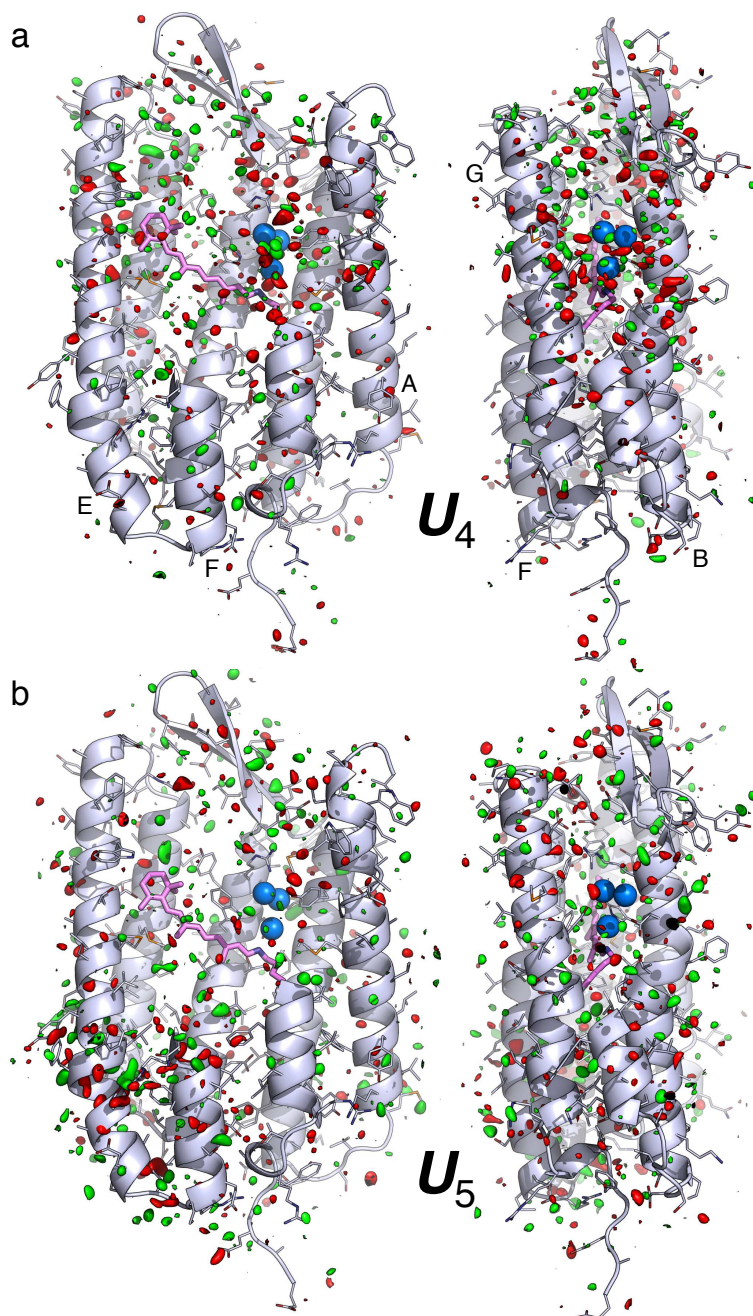
1647 Figure S4. SVD analysis of difference Fourier maps at long delays > 10 ns. SVD

1648 analyses of difference Fourier maps result in time-dependent coefficients $c_k(t)$, where $k =$

1649 1, 2, ..., each corresponding to a time-independent components \mathbf{U}_k . Each raw difference
1650 map at a time delay t can be closely represented by a linear combination of these
1651 components, $c_1(t)\mathbf{U}_1 + c_2(t)\mathbf{U}_2 + \dots$, that is called a reconstituted difference map. Each of
1652 these components \mathbf{U}_k and the reconstituted difference maps can be rendered in the same
1653 way as an observed difference map. The coefficient set $c_k(t)$ is therefore a trace of the
1654 photocycle trajectory, when these time-dependent functions are plotted in a multi-
1655 dimensional space or plotted together against the common variable t . See Methods for
1656 detail. (a) Singular values before and after rotation (Ren, 2019, 2021). 19 components
1657 stand out. (b-g) Time-dependent coefficients of four components \mathbf{U}_1 , \mathbf{U}_2 , \mathbf{U}_3 , and \mathbf{U}_6 .
1658 Each pair of the adjacent orthographical views, horizontal or vertical, can be folded
1659 along a straight line between them to erect a three-dimensional space. Each colored
1660 trace represents difference maps in a time series calculated with a common reference.
1661 Those time series with a dark reference are plotted with thick lines with dots. Other
1662 series are in thin lines without dots.
1663
1664



1667 Figure S5. Component maps \mathbf{U}_1 , \mathbf{U}_2 , \mathbf{U}_3 , and \mathbf{U}_6 from long delays. The main chain and
1668 side chains of the protein are rendered with ribbons and sticks, respectively. The retinal
1669 and Lys216 are in purple sticks. Several key waters are in blue spheres. Parts of the
1670 structure are omitted to reveal more of the interior. The maps are contoured at $\pm 3\sigma$ in
1671 green and red, respectively. (a) Two orthographical views of \mathbf{U}_1 . The signals are
1672 distributed over the EC half of the molecule. (b) Two orthographical views of \mathbf{U}_2 . The
1673 signals are concentrated around the proximal segment of the retinal. (c) Three
1674 orthographical views of \mathbf{U}_3 . Widespread signals are associated with all seven helices.
1675 (d) Two orthographical views of \mathbf{U}_6 . The signals are over the EC half of the molecule.
1676



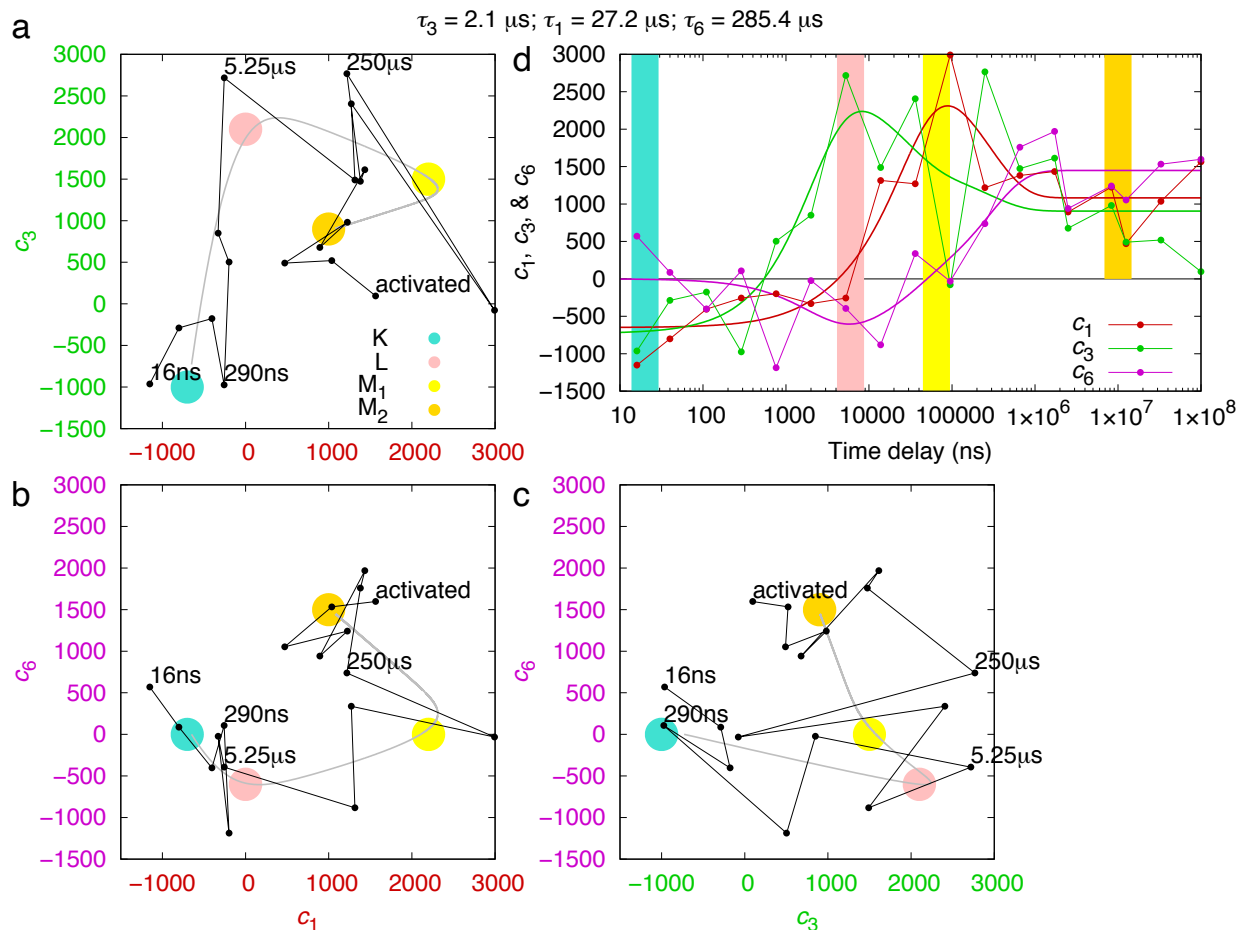
1677
1678

1679 Figure S6. Component maps U_4 and U_5 from long delays. The main chain and side
1680 chains of the protein are rendered with ribbons and sticks, respectively. The retinal and
1681 Lys216 are in purple sticks. Several key waters are in blue spheres. Parts of the
1682 structure are omitted to reveal more of the interior. The maps are contoured at $\pm 3\sigma$ in
1683 green and red, respectively. These components are not associated with a clear time
1684 dependency. Therefore, they are isolated but not used in structure refinement. (a) Two
1685 orthographical views of U_4 . Some signals are distributed over the EC half of the

1686 molecule. (b) Two orthographical views of \mathbf{U}_5 . Some signals are located around the CP
1687 segments of helices E and F.

1688

1689



1690

1691

1692 Figure S7. Exponential fitting of SVD coefficients of long delays. (a, b, and c) The time

1693 dependencies of the SVD coefficients $c_1(t)$, $c_3(t)$, and $c_6(t)$ of the long delays are modeled1694 with exponential functions (Methods). The time constant τ_k associated with the major1695 change in each coefficient models a step in the reaction scheme $K \rightarrow L \rightarrow M_1 \rightarrow M_2$. $\tau_3 =$ 1696 $2.1 \pm 1 \mu\text{s}$ or a rate of 470 ms^{-1} is the rate of increase in $c_3(t)$. $\tau_1 = 27 \pm 10 \mu\text{s}$ or a rate of 37 1697 ms^{-1} describes the jump in $c_1(t)$. $\tau_6 = 290 \pm 100 \mu\text{s}$ or a rate of 4 ms^{-1} seems to separate M_1 1698 and M_2 . The fitted exponential functions are plotted as the gray curves through the

1699 black dots derived from SVD in three orthographical views of the three-dimensional

1700 subspace of c_1 , c_3 , and c_6 . The large colored dots mark the relatively pure states of K, L,1701 M_1 , and M_2 . (d) SVD coefficients and their exponential fittings as functions of time. The

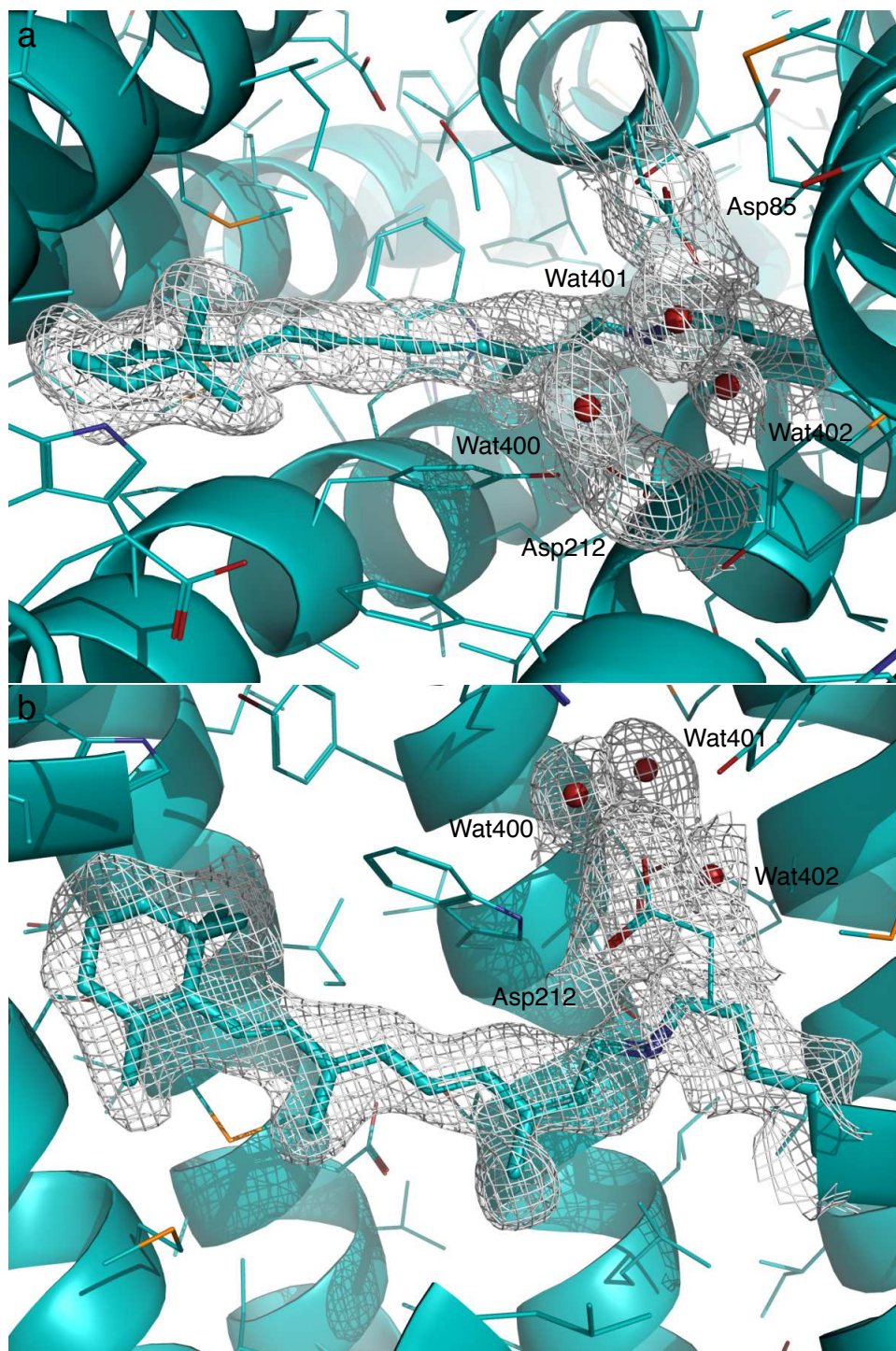
1702 relatively pure states are marked as color bars at the approximate time. The result of

1703 exponential fitting shows the time-dependency clearer. The second component map U_2

1704 seems to be a constant component without a time-dependent trend (Fig. S4cde). It

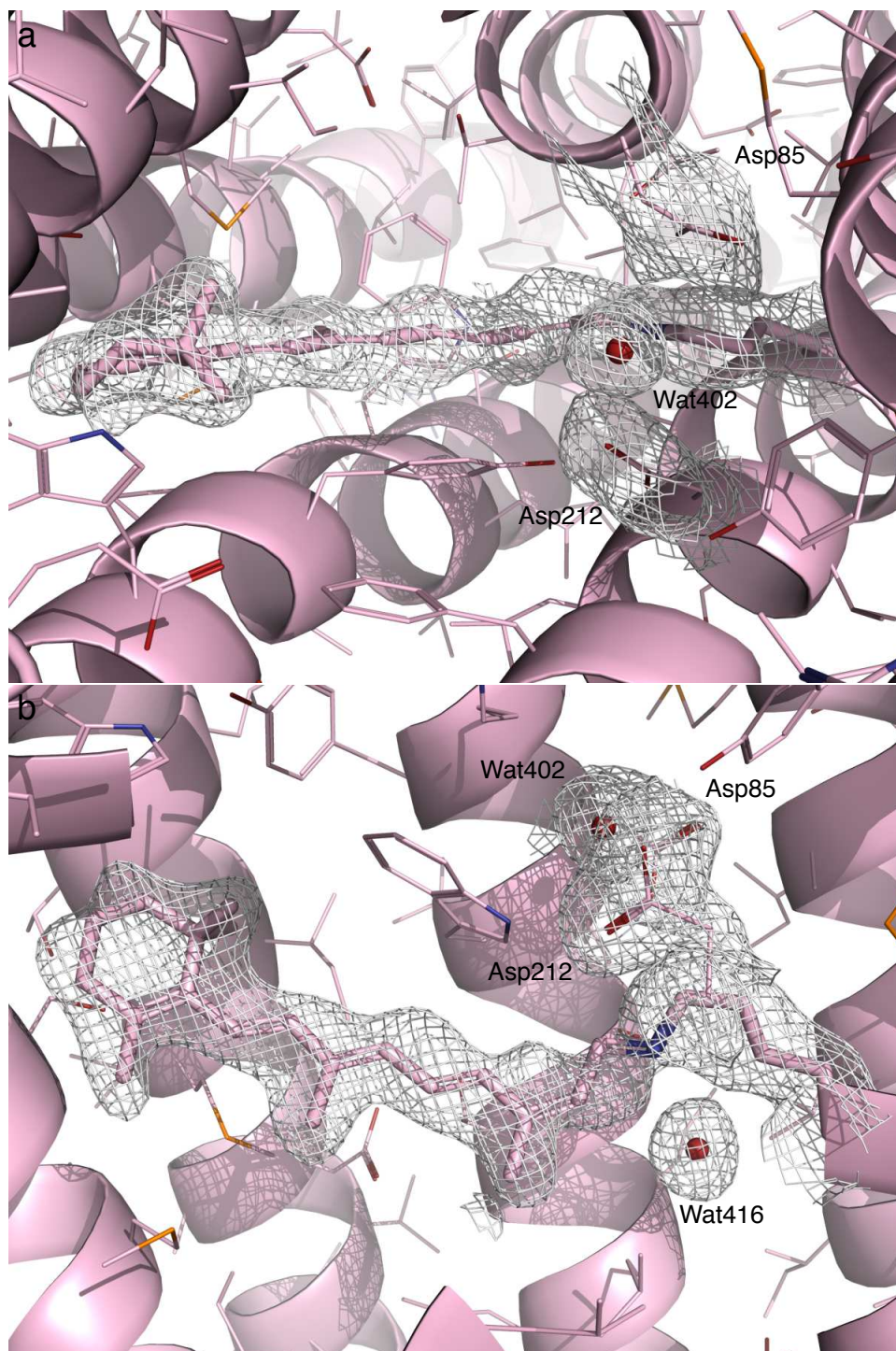
1705 describes significant changes near the SB and the retinal anchor (Figs. 3ab and S5b). The

1706 third component map \mathbf{U}_3 increases sharply and consistently around 1 μs (Figs. S4beg).
1707 This component contains widespread signals associated with all seven helices (Fig. S5c),
1708 therefore describes the global changes during $\text{K} \rightarrow \text{L}$ transition. The first component \mathbf{U}_1
1709 increases at 10 μs (Figs. S4bdf), which could reflect the changes during $\text{L} \rightarrow \text{M}$
1710 transition. \mathbf{U}_1 clearly contains signals over the EC half of the molecule (Fig. S5a), which
1711 indicates events related to the proton release. Similarly, the sixth component \mathbf{U}_6 also
1712 shows additional signals on the EC half to a lesser extent (Fig. S5d). This component
1713 seems to increase at a rather late time around hundreds of μs (Figs. S4cfg), which splits
1714 the M state into M_1 and M_2 .
1715



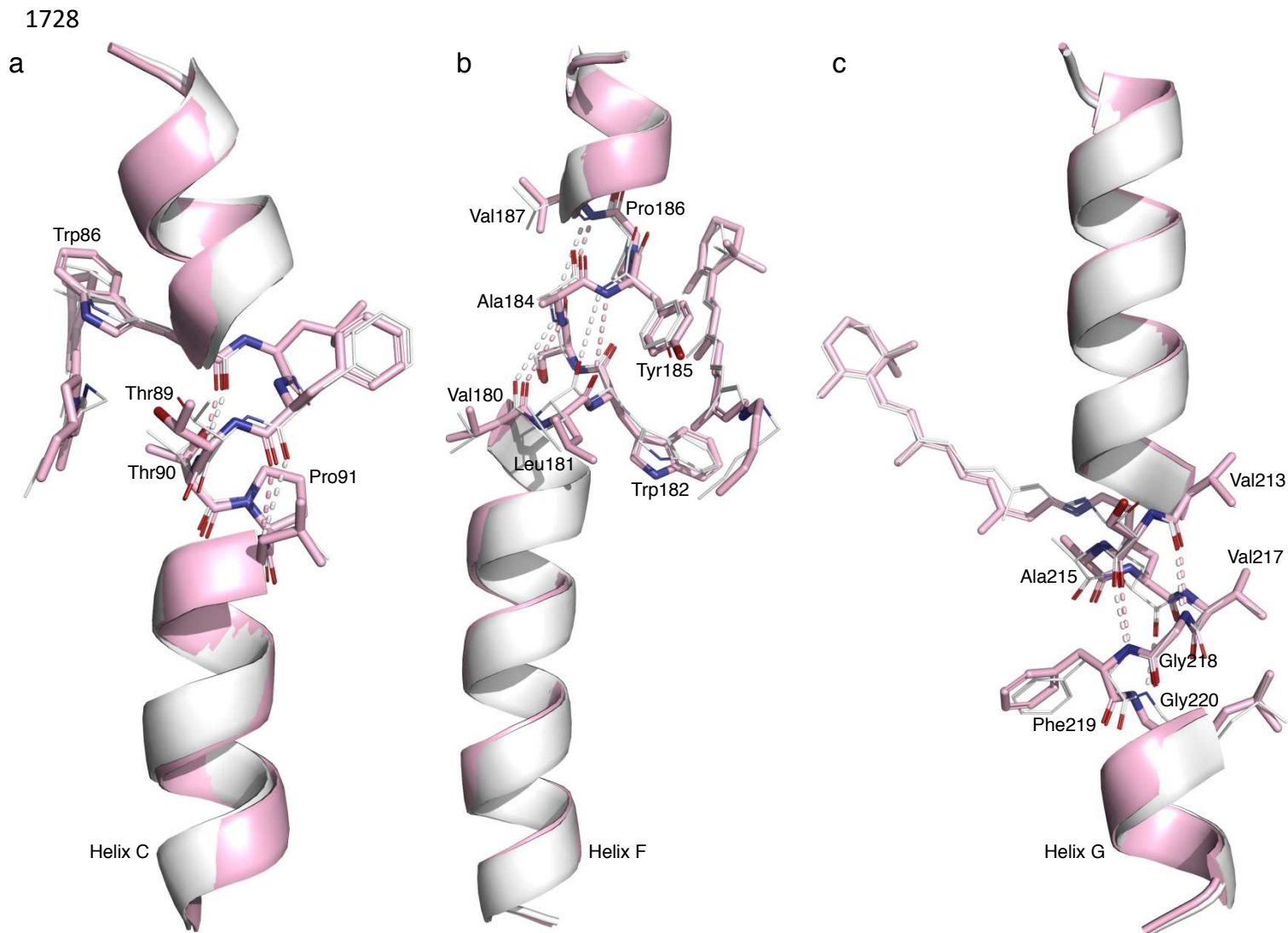
1716
1717

1718 Figure S8. Two orthographical views of the 2Fo-Fc map of K contoured at 6σ . Here Fo
1719 is the reconstituted structure factor amplitudes rather than observed amplitudes (Table
1720 S2). Fc is the structure factor amplitudes calculated from the refined structure
1721 (Methods). The same applies to the other 2Fo-Fc maps.



1722
1723

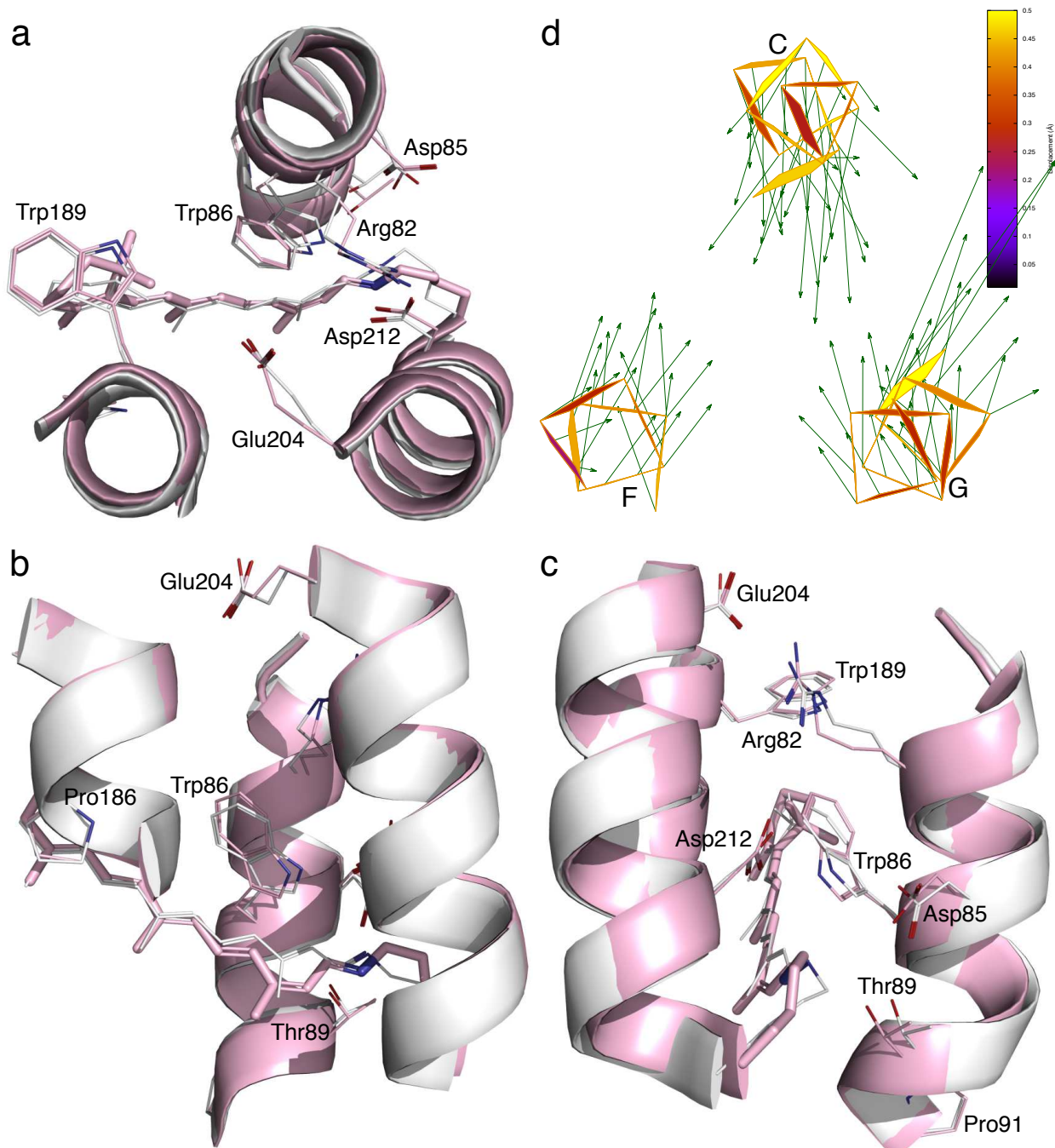
1724 Figure S9. Two orthographical views of the 2Fo-Fc map of L contoured at 3.5σ . Here Fo
1725 is the reconstituted structure factor amplitudes rather than observed amplitudes (Table
1726 S2). Fc is the structure factor amplitudes calculated from the refined structure
1727 (Methods).



1730

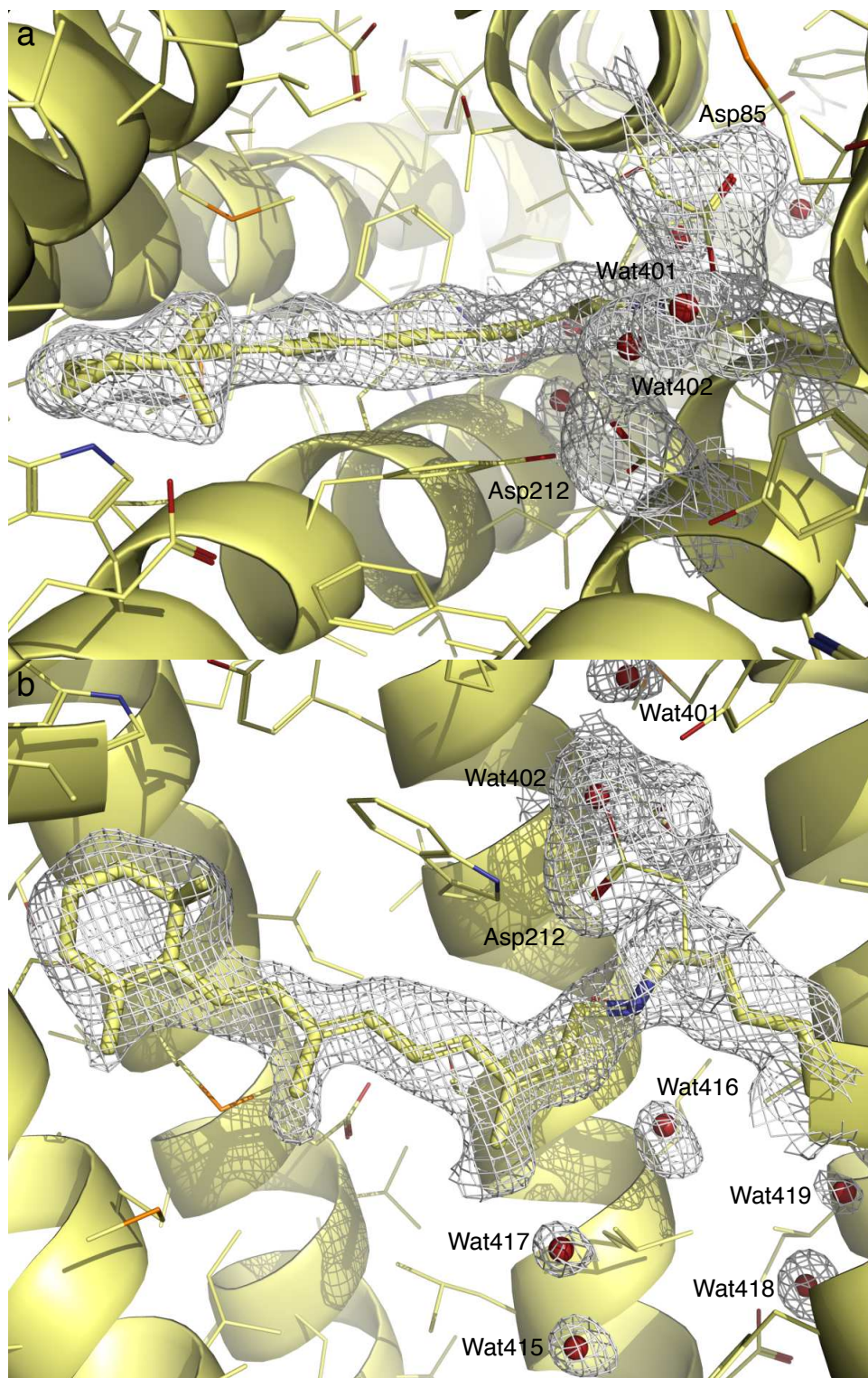
1731 Figure S10. Irregularities in helices C, F, and G. bR in the resting state and L are
 1732 rendered in white and pink, respectively. (a) Kinked helix C. All main chain H-bonds
 1733 are regular except that Pro91 in helix C causes a kink. This kink was noticed as soon as
 1734 the bR structure was determined to a reasonable resolution (Grigorieff et al., 1996). In
 1735 the resting retinal, the corner of C_{ϵ} makes a contact with Thr89 and pushes the helix
 1736 inboard. In bR, J, K, and L, C_{ϵ} moves more and more outboard (Fig. 3f). So does Thr89.
 1737 The opposite motions occur in L, M_1 , M_2 , and back to bR (Fig. 4c). Thr90 also
 1738 contributes to the seal. Pro91 is located exactly at right place to facilitate this spring-
 1739 loaded bend. (b) Stretched helix F. Pro186 removes one H-bond in helix F. Several
 1740 would-be H-bonds in the main chain around Pro186 are stretched to 3.6-4.2 Å in the
 1741 resting state, such as Val180O-Ala184N, Leu181O-Tyr185N, and Ser183O-Val187N.

1742 Pro186 and these stretched H-bonds marked by dashed lines effectively breaks helix F
1743 into two segments. In J, K, and L, Trp182 is pushed by C₂₀ methyl group more and
1744 more toward the CP. The breakage in helix F stretches even more. P186L mutant is
1745 likely to feature an intact α helix F with uninterrupted main chain H-bonds. Its proton
1746 pumping activity is severely affected (Hackett et al., 1987). A more rigid helix F would
1747 increase the difficult to displace Trp182 toward the CP direction and hinder the opening
1748 of the CP half channel for proton uptake. (c) π helical segment in helix G. The retinal
1749 anchor is in a π helical segment with two main chain H-bonds Val213O-Gly218N and
1750 Ser214O-Phe219N. Unlike the regular α helix, a π helix features H-bonds from the
1751 carbonyl of residue n to the amide N of residue $n+5$. During the transition from the α
1752 helix to the π helical segment, Val217N does not have a H-bond partner. As the π
1753 helical segment transitions back to the regular α helical conformation, Ala215O does not
1754 join the H-bond pattern for helical formation. Loss of main chain H-bonds on both
1755 sides of the retinal anchor allows the anchor to move 1.2 Å in L. In addition, two
1756 nearby Gly218 and 220 increase the flexibility of the anchor.
1757



1758
 1759
 1760
 1761
 1762
 1763
 1764

Figure S11. Tighter EC half channel in L. (a-c) Three orthographical views of the EC half channel. The resting state and L state are rendered in white and pink, respectively. (d) Atomic displacements in the main chain around the EC half channel from the resting state to L are marked with arrows 10× as long as the actual values.



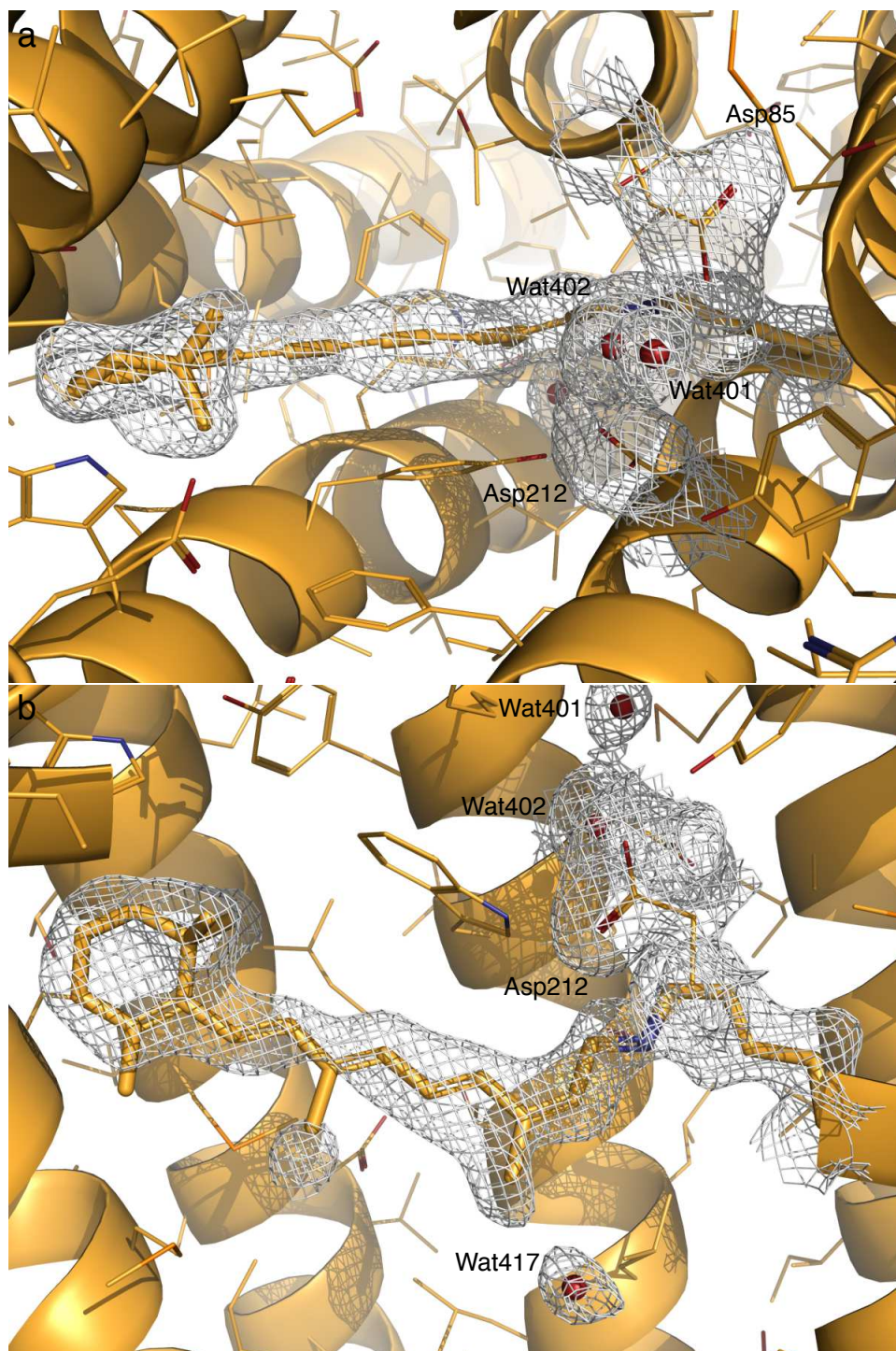
1765
1766

1767 Figure S12. Two orthographical views of the 2Fo-Fc map of M₁ contoured at 3σ. Here
1768 Fo is the reconstituted structure factor amplitudes rather than observed amplitudes

1769 (Table S2). F_c is the structure factor amplitudes calculated from the refined structure
1770 (Methods).

1771

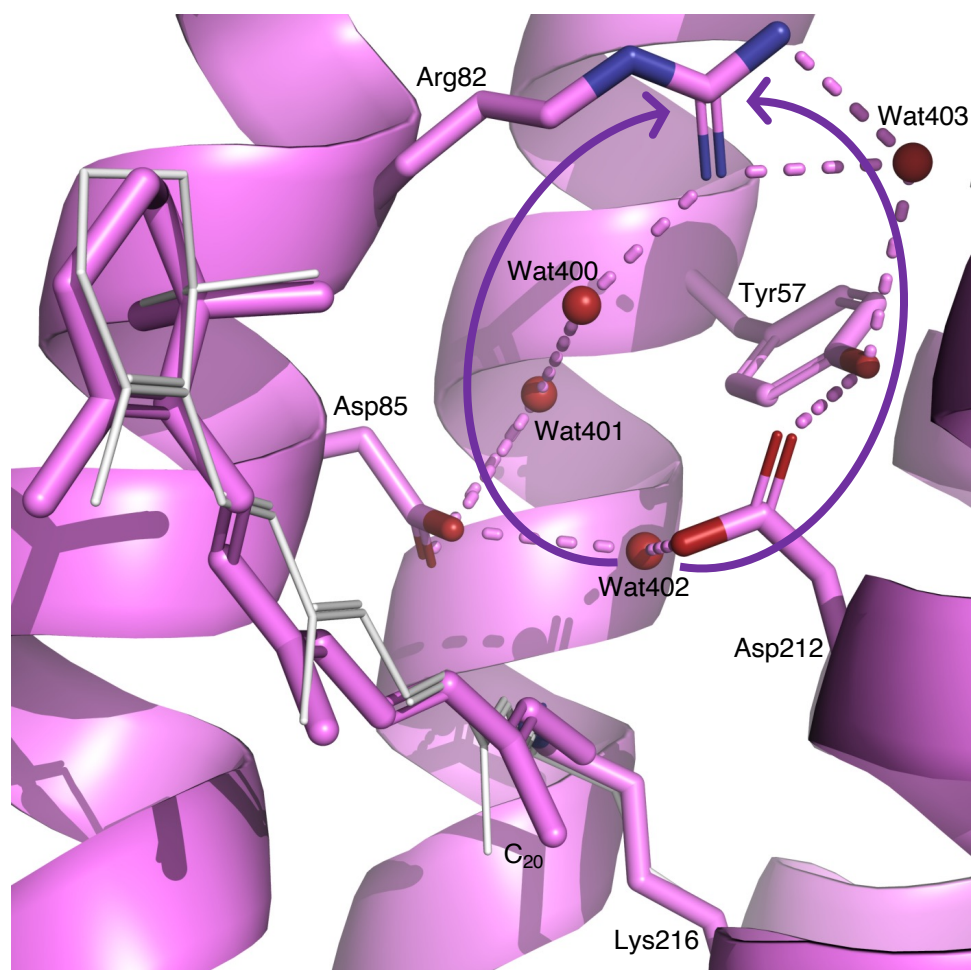
1772



1773
1774

1775 Figure S13. Two orthographical views of the $2F_o - F_c$ map of M_2 contoured at 5σ . Here
1776 F_o is the reconstituted structure factor amplitudes rather than observed amplitudes
1777 (F_c is the structure factor amplitudes calculated from the refined structure
1778 (Methods).

1779



1780

1781

1782 Figure S14. H-bond network at end of EC half channel in I state. Two curved arrows
1783 mark two possible proton conductance pathways. At more acidic EC pH, the pathway
1784 through Asp85 is in use and that through Asp212 is blocked by Tyr57. At more alkaline
1785 EC pH, Tyr57 could deprotonate thus the pathway through Asp212 may help to
1786 increase the proton flow. Both pathways conduct protons only under a concentration
1787 gradient of protons.

1788

Supplementary Files

This is a list of supplementary files associated with this preprint. Click to download.

- [SupplementaryFile.docx](#)